Technical Report No. 1180-1

AUTONOMOUS RPRV NAVIGATION, GUIDANCE AND CONTROL

Donald E. Johnston
Thomas T. Myers
John W. Zellner

March 1983

TABLE OF CONTENTS

SECTION I

INTRODUCTION

NASA Dryden Flight Research Center has the responsibility for flight test of advanced remotely piloted research vehicles (RPRV) to explore highly maneuverable aircraft technology, and to test advanced structural concepts, and related aeronautical technologies which can yield important research results with significant cost benefits. These RPRV's, such as HiMAT (Ref. 1) and DAST, are launched from a B-52 and controlled remotely from a ground pilot station, Fig. 1, at DFRF using a telemetry uplink for issuing control commands and a downlink for sending sensor data. The RPRV is tracked by a ground radar station capable of tracking the vehicle with less than 12 yards error. The radar processing facility is capable of generating guidance information over the telemetry uplink including synthetic ILS localizer and glide slope data for three runways on the lake bed.

At the present time landings on one of the three runways is accomplished by visual reference to a forward looking TV image which is data linked to the remote cockpit CRT display. Prior to landing flare the pilot has synthetic glide slope and localizer errors displayed on the remote cockpit attitude director indicator (ADI) display. Using the ground station control stick and rudder pedals the pilot flys the RPRV to acquire the synthetic beam and stabilize the vehicle path along the approach path by minimizing the director indicator errors. For the flare and touchdown the pilot uses the TV image for landing. The pilot lacks altitude data and a yaw angle due to wind crab looks like a runway offset. Consequently, the last 500 ft of landing is confusing. The pilot work load is high, and difficult to accomplish, but the pilots do an acceptable job after performing several practice landings in a PA-30 aircraft with a safety pilot prior to an actual RPRV flight.

An automatic flare mode is available for the longitudinal axis as a part of the HIMAT backup control system. This mode can be activated when below 5000 ft radar altitude by selecting the LAND mode. The vehicle then executes a preprogrammed flare and airspeed reduction
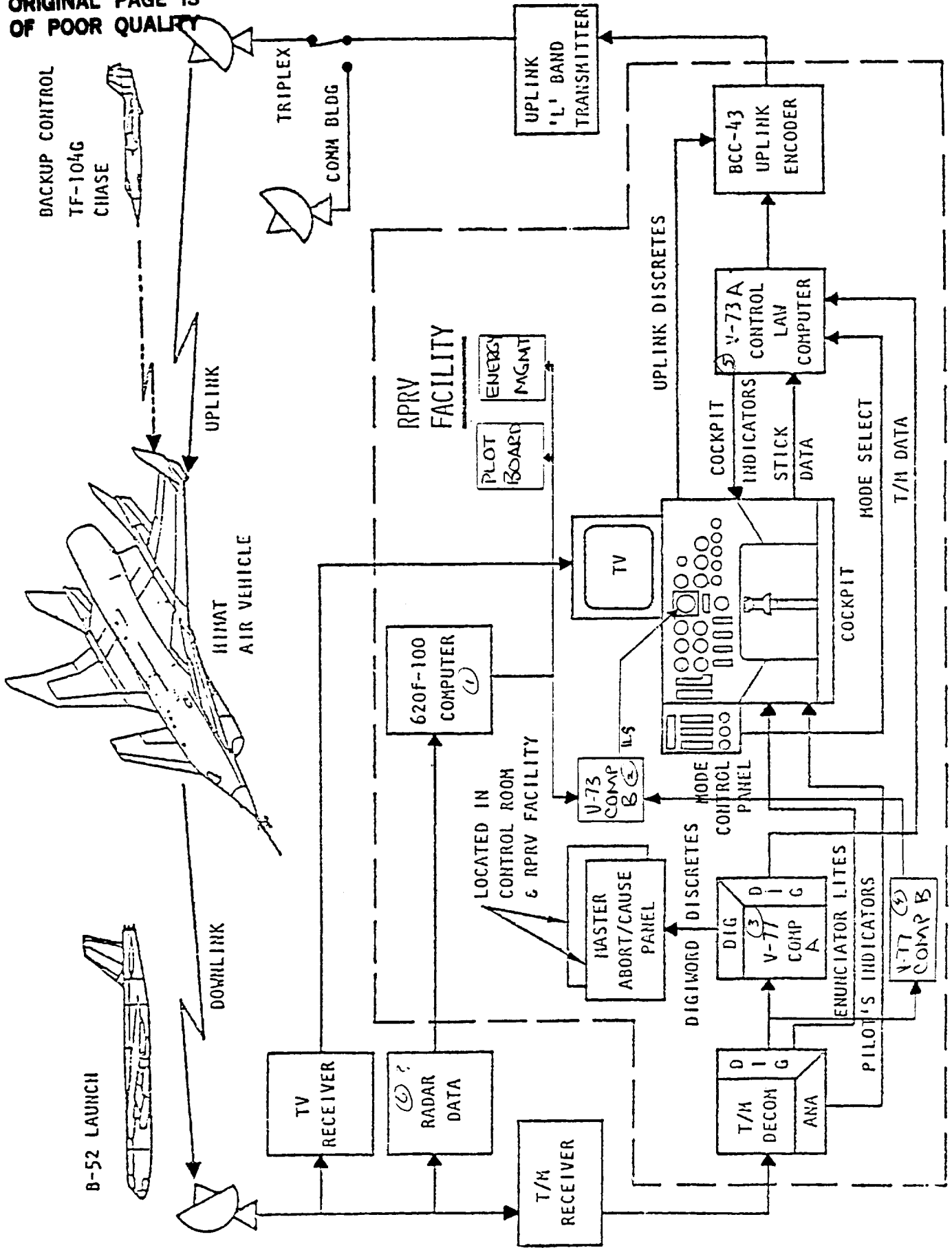
Figure 1. Control Loop

maneuver referenced to radar altitude but again the T.V. display to the pilot is confusing.

In case of a failure in the uplink the RPRV is commanded into a level, constant bank angle orbit which continues until communication is restored or the vehicle crashes. At the present time there is no means to command the vehicle to automatically proceed to a safe unpopulated area in case of total uplink loss.

NASA DFRF is interested in developing a system which shall make manual landings easier and more consistent and to provide a simple autonomous navigation system aboard the RPRV to have it proceed to a safe area for orbiting after loss of uplink. The provision of an autoland capability supervised by the remotely located pilot would be beneficial in reducing pilot workload and making the landings more consistent.

The primary purpose of this study is to provide the preliminary design of an upgraded automatic approach and landing control system and flight director display to improve landing performance and reduce pilot workload. A secondary purpose is to determine the feasibility of an onboard autonomous navigation, orbit, and landing capability for safe vehicle recovery in the event of loss of telemetry uplink communication with the vehicle.

The following sections describe the current RPRV approach and landing method, the proposed automatic and manual approach and autoland system, and an autonomous navigation, orbit, and landing system concept which is based upon existing operational technology.

The intent of the study is to upgrade the DFRF facility rather than a specific vehicle performance. At the outset of the study the HiMAT RPRV was specified as the example vehicle. However, it rapidly became apparent that the desired flight control and director display algorithms must be vehicle specific and the HiMAT vehicle would no longer be operational by the time any of the control and display concepts could be implemented. Since the PA-30 aircraft has been used in the past as a developmental test bed and is likely to continue in this role in the future, the various analysis herein have been more or less focused on the PA-30.

SECTION II

CURRENT RPRV APPROACH AND LANDING

A. MANUAL APPROACH AND LANDING

1. Normal Procedures

The approach and landing is flown by the ground based pilot viewing the head down instrument panel or head up TV display and operating the cockpit controls (stick and pedals). The pilot is guided to intercept an extension of the runway centerline via verbal guidance commands of test personnel who monitor the horizontal position of the vehicle on an X-Y plot board containing a map of the area. The vehicle is then descended, at a rate based upon the specific test conditions, to intercept a computer generated "synthetic ILS" glide slope of 2.82 deg eminating from a runway aim point one nautical mile from the runway threshold (see Fig. 2).

Measures representative of deviation from the "synthetic ILS" beam are calculated in the 620-f-100 computer based upon FPS-16 tracking radar data (see Fig. 1). These deviations are modified in V-73 Computer A to drive the flight director needles of the Attitude Director Indicator (ADI) on the pilot's display panel. Thus, the pilot can "fly" the "synthetic ILS" beam until the runway comes into view of the vehicle mounted TV camera and is displayed on the head-up TV monitor. The final approach and flare is then flown by means of the TV view with an engineer calling out altitude and airspeed.

Stick and rudder pedal deflections by the pilot command pitch, roll, and yaw rate responses via the control algorithms mechanized in the ground computer. The computer outputs surface actuator position commands which are then uplinked to the RPRV.
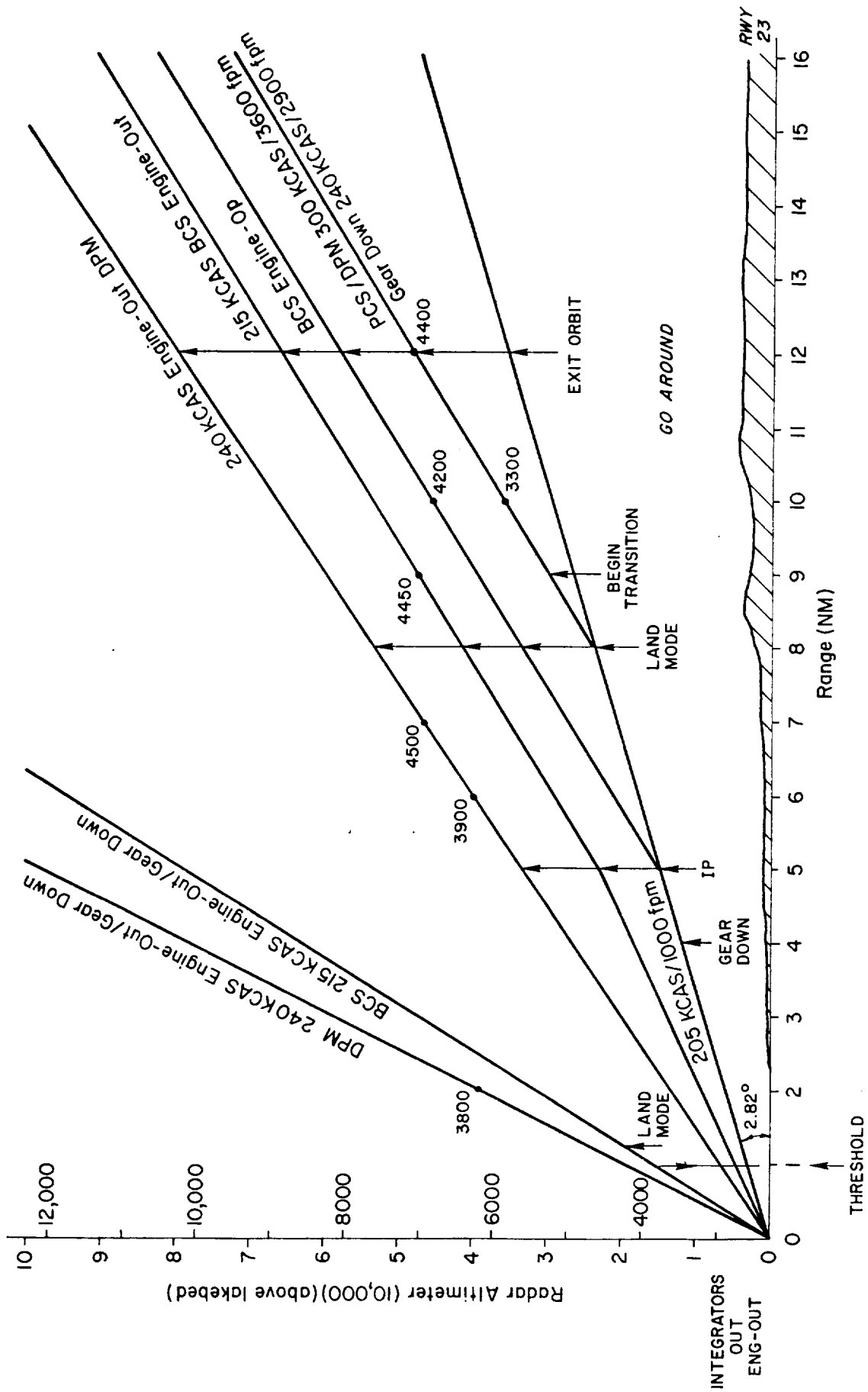
Figure 2. Typical HIMAT RPRV Approach Paths

2. ADI Synthetic ILS Information

Documentation was not found for the algorithms used to compute the synthetic ILS beam and vehicle displacement error signals used in the ADI flight director mode. However, error could be determined from radar tracking measurements and trignometric relationships such as depicted in Fig. 3. The FPS-16 tracking radar provides measurements of the RPRV range, R, azimuth, A_z, and elevation, E_ℓ, relative to the tracking station (or some other bench mark). The RPRV location relative to the synthetic beam is computed to produce glide slope and localizer position error measures, h_e and y_e, respectively to drive the ADI needles.

Based upon the relationships shown in Fig. 3 the error calculations could be:

$$y_e = Y - R \cos \varepsilon_a$$

$$h_e = h - h_\gamma$$

$$= (R \sin \varepsilon_e + Z) - L \tan \gamma$$

where

Y = perpendicular distance from runway center-line to radar

Z = height of radar above like bed

L = $R \cos \varepsilon_e (\sin \varepsilon_a - \cos \varepsilon_a \tan a_f)$

R = measured vehicle range from radar

ε_e = measured vehicle elevation above radar

ε_a = measured vehicle azimuth from perpendicular to runway

a_f = angle between perpendicular to runway and azimuth to aim point

Figure 3. Pseudo or Synthetic ILS Beam

The FPS-16 measurement accuracy is (Ref. 2):

Range: ±30 ft

Azimuth: ±0.1 mil

Elevation: ±0.1 mil

The radar is located on a hilltop approximately 2.5 nm west of the intersections of runways 15/33 and 5/23 (see Fig. 4). From this vantage point it provides an unobstructed view of these runways and runway 7/25, the runways designated for RPRV landing (Ref. 3). Unfortunately, the orientation between the runway centerline and radar location is such that vehicle lateral (localizer) error would probably be determined from the range measurement on runways 15/33, 5/25, and 5, and from azimuth only on runway 23. Although this has some influence on error measurement accuracies the impact is small considering the width of these runways and the surrounding areas of lakebed. The principal effect would be on the algorithm to compute lateral error.

3. TV Display

The forward looking TV cameras provide a restricted, two dimensional black and white view of the area directly ahead of the vehicle. The camera axis is depressed with respect to the aircraft longitudinal axis to assure a view of the runway during the flare. Thus, in steep descents the horizon is not visible and roll attitude information is lacking. The runway does not come into view until late in the approach and then it is difficult for the pilot to extract the necessary information as to runway alignment, flight path, altitude, etc. As an example, three different restricted views of the runway from a banked aircraft are shown in Fig. 5 (from Ref. 4) along with an unrestricted view. All views are the same runway and horizon sketch but only in the unrestricted view can it be determined that the aircraft is aligned with the left side of the runway.

The monitor, an 11 in. (diagonal) black and white display, is located about 20 in. from the pilots eye. The camera has a 50 mm lens. This results in a magnification factor of 1.8 (Ref. 4).
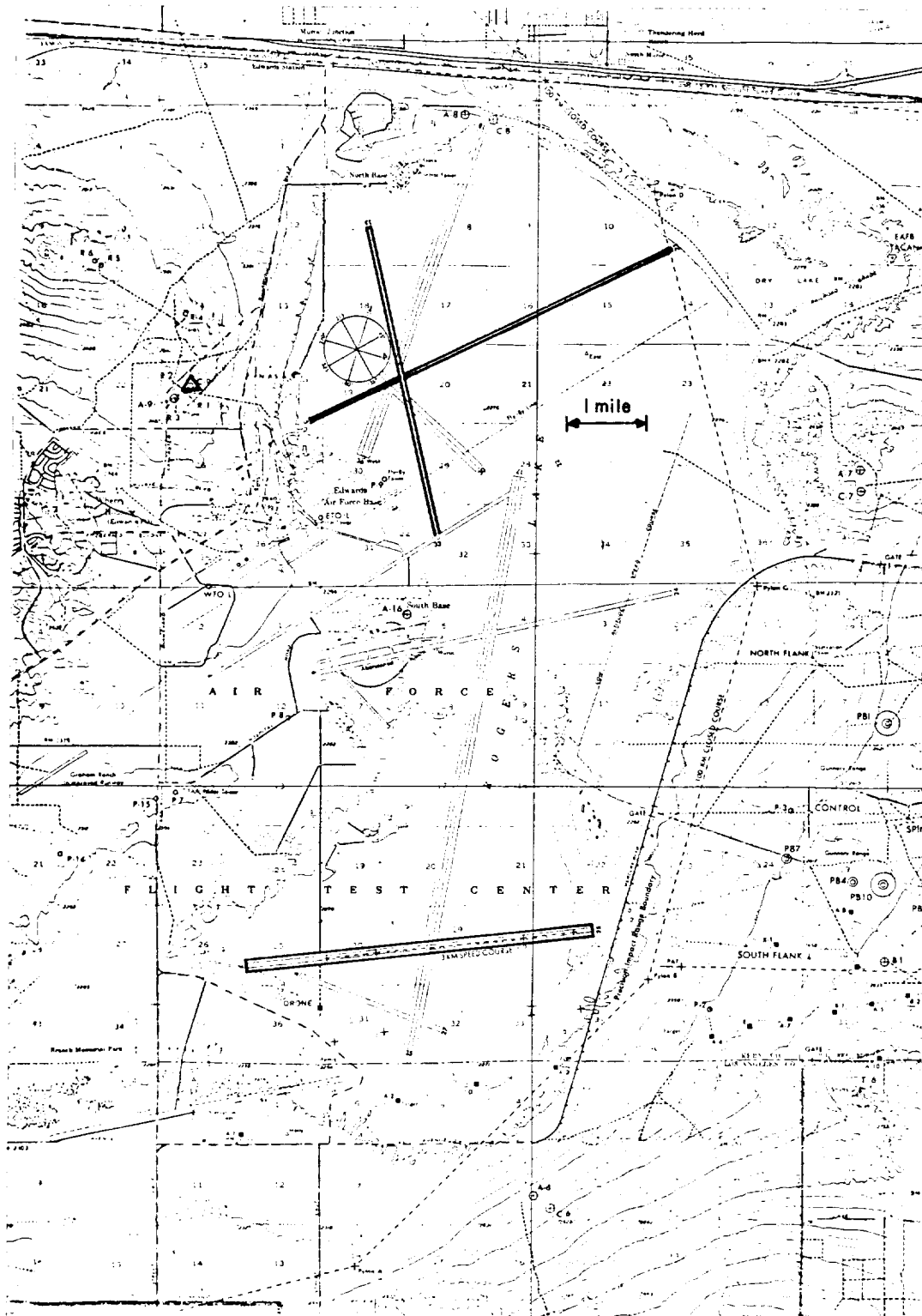
Figure 4. Runways Designated for RPRV Landings
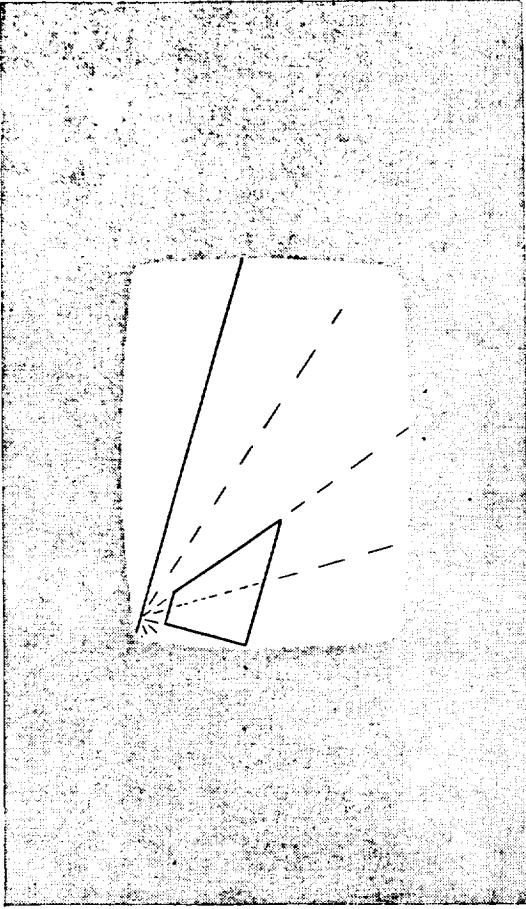
Restricted view of runway, aircraft banked.
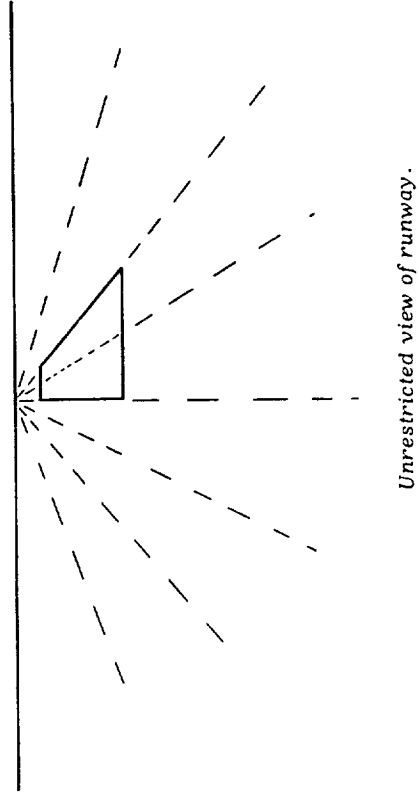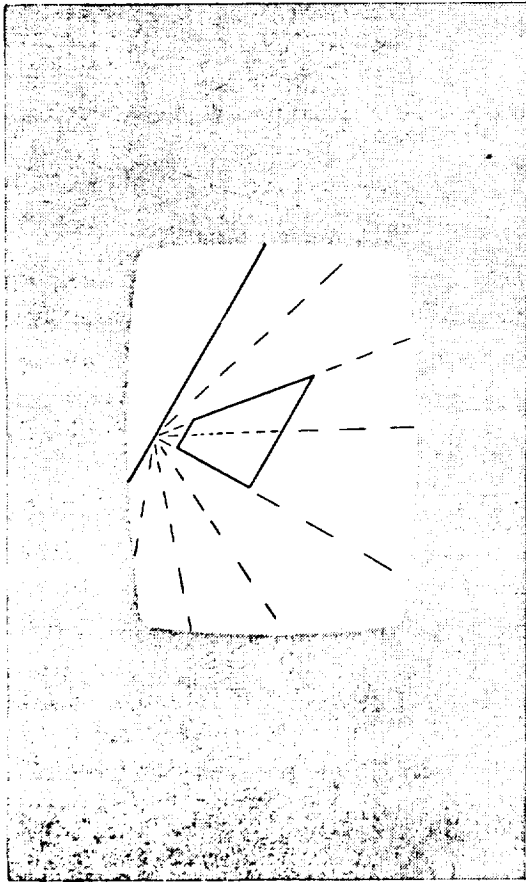
Unrestricted view of runway.

Restricted view of runway, aircraft banked.
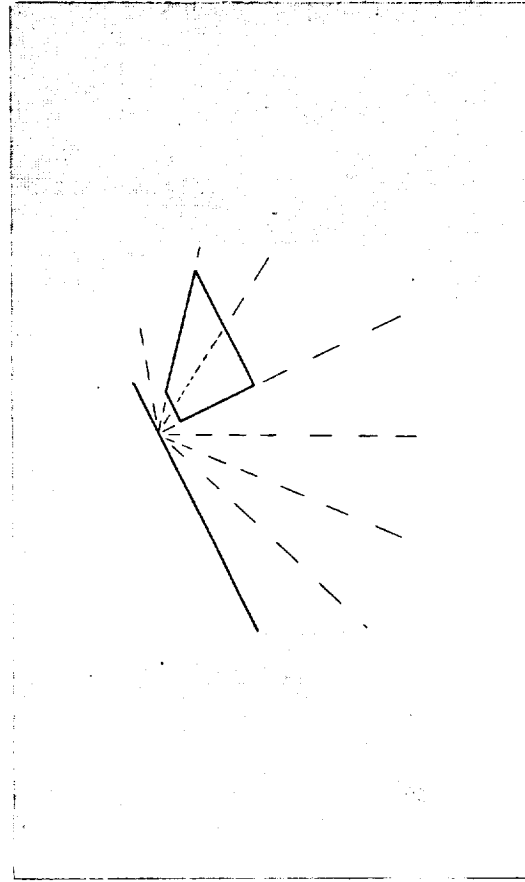
Restricted view of runway, aircraft banked.

Figure 5. Influence of Restricted T.V. View on Interpretation of Vehicle Alignment

During the final approach and flare phase the pilot is reluctant to look away from this restricted view long enough to obtain altitude or airspeed data from the instrument panel. Thus, the necessity for an engineer to call out this information.

4. Control System

The remote vehicle control mechanization described here is the system implemented for the PA-30 aircraft (Refs. 5 and 6) to validate the HIMAT backup control system (BCS) autoflare concept prior to the first HIMAT flight. This PA-30 mechanization subsequently has been employed as a ground pilot trainer/refresher system prior to each RPRV flight. In this application the RPRV flight control system is mechanized on the ground computer and commands to the various control actuators are uplinked to the PA-30 servo amplifier. The vehicle motion parameters downlinked to the computers are listed in Table 1 (from Ref. 5).

The PA-30 has an onboard pilot to fly it via its own control system to the desired area for initiating the ground controlled approach. Control is handed off to the ground pilot in what is termed the computer direct (CD) mode for pitch, roll, and yaw. See Figs. 6, 7, and 8 taken from Ref. 5. The ground pilot then selects the pitch, roll, and yaw rate damping (RD) modes as the primary means of maneuvering control. This mechanization incorporates both rate and attitude feedbacks in the pitch and roll axes and are a form of rate command, attitude hold control. The latter modes had been used previously in the PA-30 aircraft and gave improved handling over the basic control system.

When approach line-up requirements have been met the ground pilot can select the autoflare mode for completion of the approach and landing.

B. HIMAT BACKUP CONTROL SYSTEM AUTOFLARE MODE

The "Autoflare" mode is pilot selectable at any altitude below the radar altimeter upper limit of 5000 ft. The longitudinal pitch axis incorporates a preprogrammed two-step altitude rate descent followed by

TABLE 1. PA-30 DOWNLINKED VARIABLES

	MNEMONIC	DESCRIPTION	SCALING
1	P	Roll Rate	±40 deg/sec
2	Q	Pitch Rate	±25 deg/sec
3	R	Yaw Rate	±40 deg/sec
4	Theta	Pitch Attitude	±60 deg
5	Phi	Roll Attitude	±90 deg
6	HRAD	Radar Altimeter	0-5000 ft
7	DW1	Digital Word #1	--
8	DW2	Digital Word #2	--
9	VKIAS	Indicated Airspeed	0-200 kts
10	SQSWM	L/H Gear Squat Switch	On/Off
11	DAP*	L/H Lateral Wheel Position	±10.2 in.
12	DRP*	L/H Pedal Position	±5.24 in.
13	DEP*	L/H Pitch Wheel Position	±13.16 in.
14	AZ	Normal Accelerometer	+2 to -5 g
15	AY	Lateral Accelerometer	
16	HDOT	IVSI	±2000 ft/min

*During RPRV mode of operation the ground pilot control positions will be used instead of the variables marked with the asterisk.
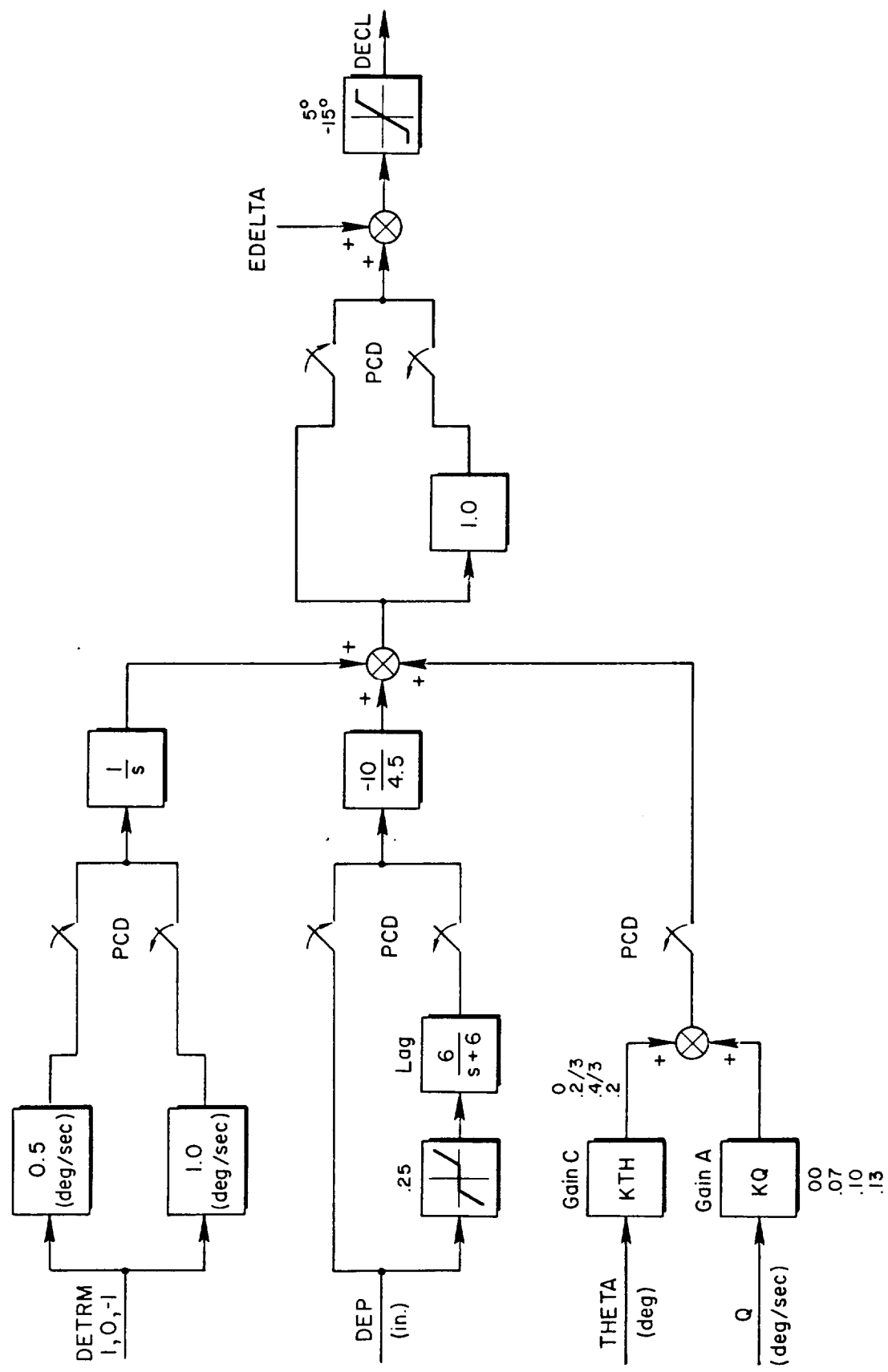
Figure 6. PA-30 Pitch CD/RD
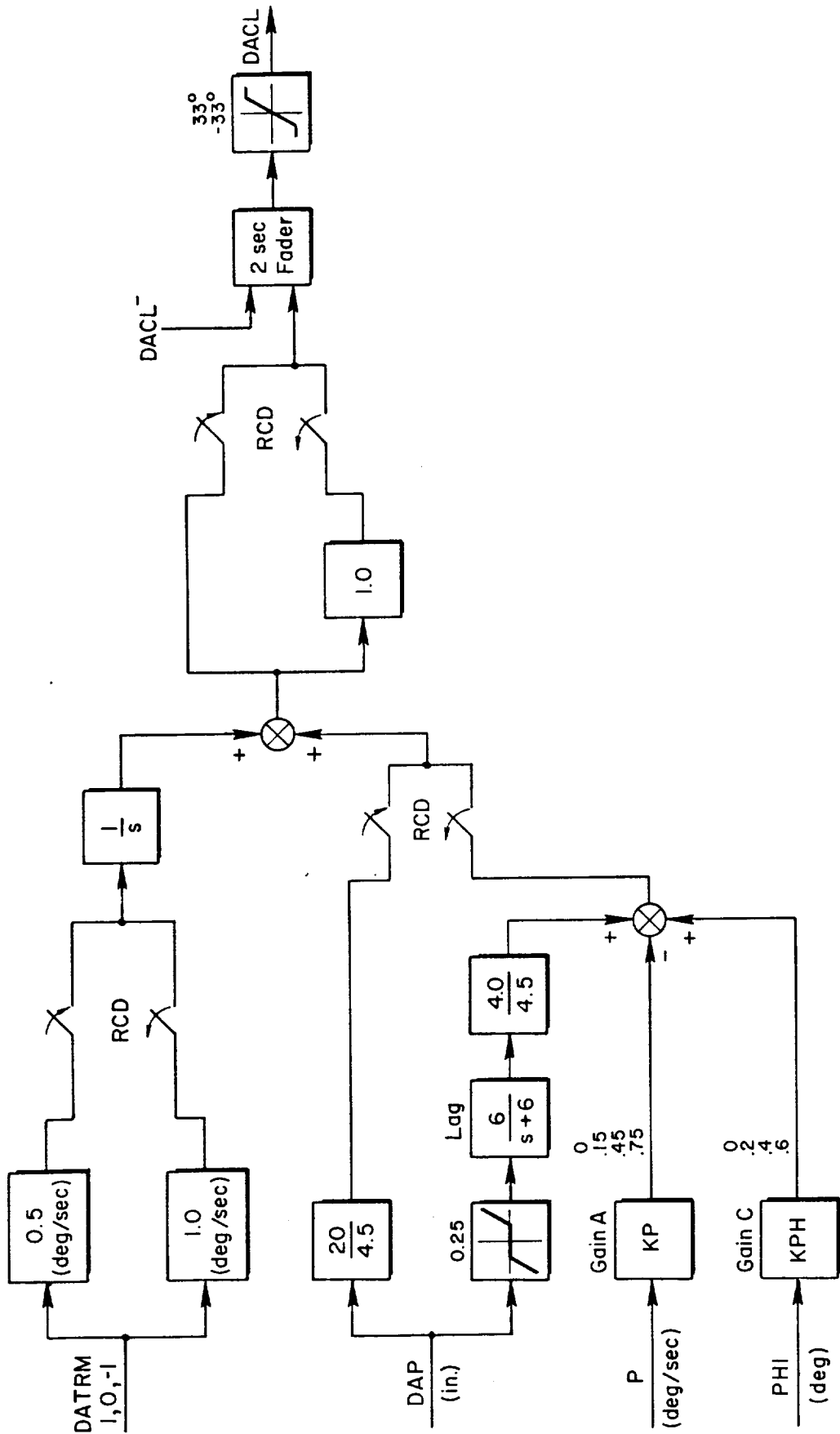
Figure 7. PA-30 Roll CD/RD

14
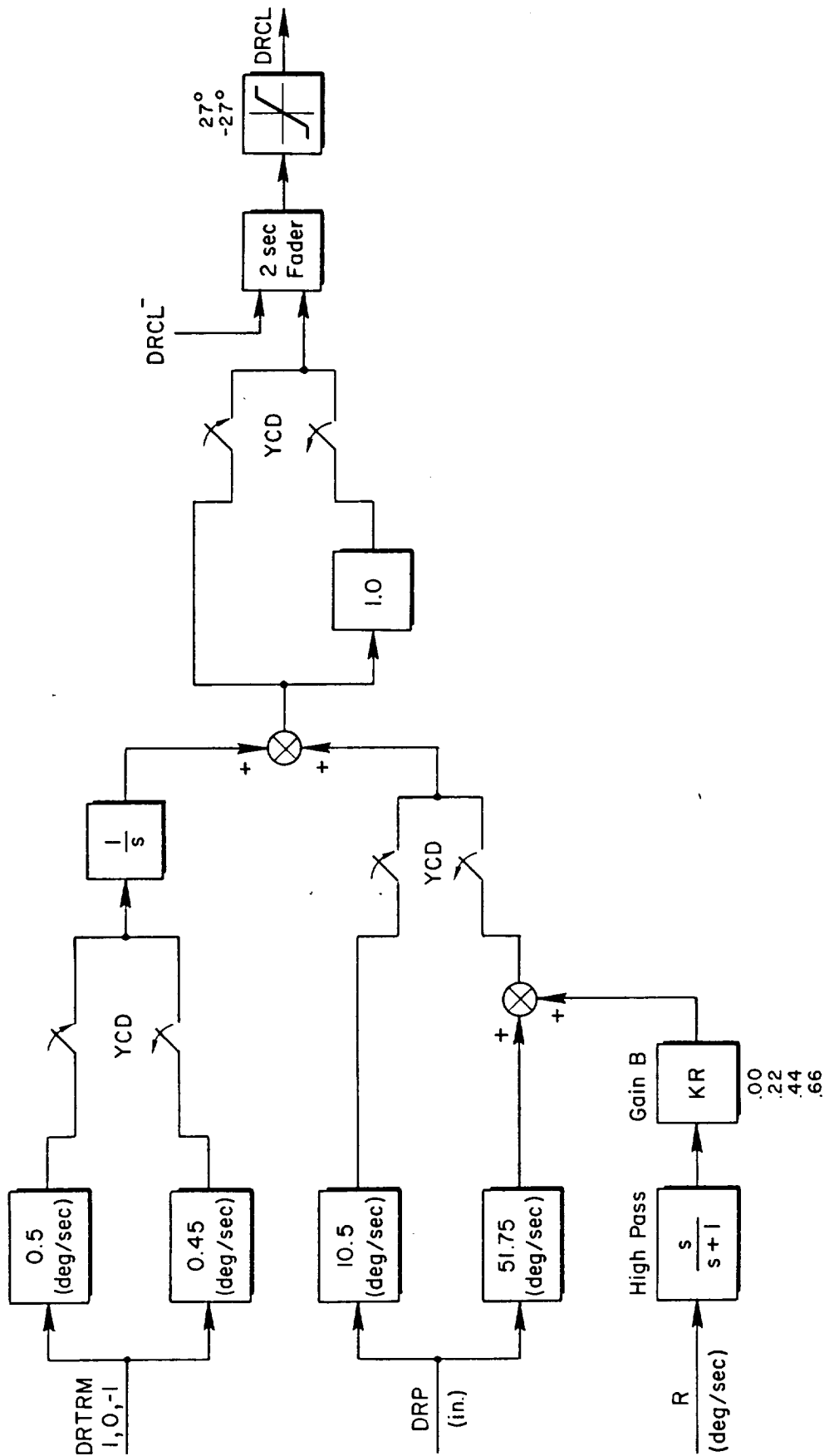
Figure 8. PA-30 Yaw CD/RD

an exponential flare to landing. The complete approach and flare is scheduled via onboard radar measurement of altitude above ground level but provision is made for the pilot to insert discrete climb/dive rate increment corrections if necessary. The longitudinal axis also contains an autothrottle for airspeed control — again scheduled via radar altitude.

The roll axis "autoflare" mode is a zero yaw rate hold system with pilot commandable discrete left/right step turn rate commands. The yaw axis consists of a yaw rate damper with lateral acceleration turn coordination.

1. Longitudinal Mechanization and Performance

PA-30 pitch axis and autothrottle mechanization block diagrams are presented in Figs. 9 and 10, respectively. In the pitch axis, the path sink rate control is implemented through the h_{RAD} and $\dot{h}_{BARO}$ feedback loops. The inner loop normal acceleration and pitch rate feedbacks provide the proper equalization and vehicle damping for the outer path loop control. A stability analysis of the PA-30 pitch feedbacks including sensor and actuator dynamics is contained in Appendix A.

To provide a reference for the improved autoland system proposed later, an idealized PA-30 system performance analysis will be made in which sensor dynamics are assumed to be perfect and the sink rate and airspeed schedules are approximated as shown in Fig. 11. These commanded schedules divide the autoflare program into three phases which are summarized in Table 2. For the present assessment, only the deceleration and flare regions are considered.

Considering the altitude control channel as shown in Fig. 9 the sink rate error, $\dot{h}_\epsilon$, is

$$\dot{h}_\epsilon = -\dot{h}_{BARO} + \dot{h}_c \qquad (1)$$
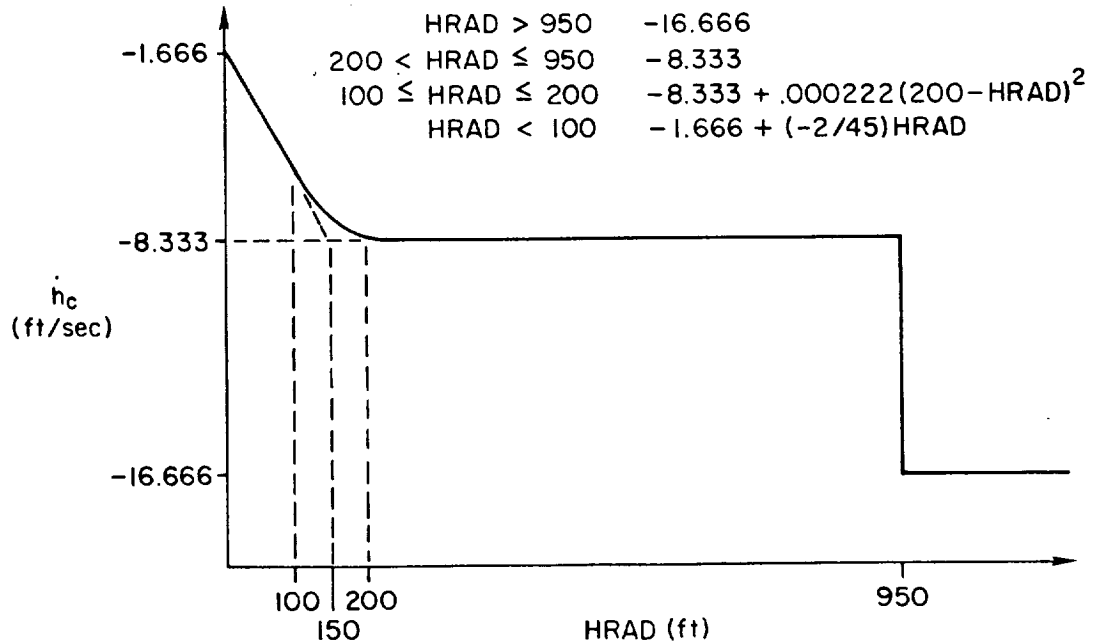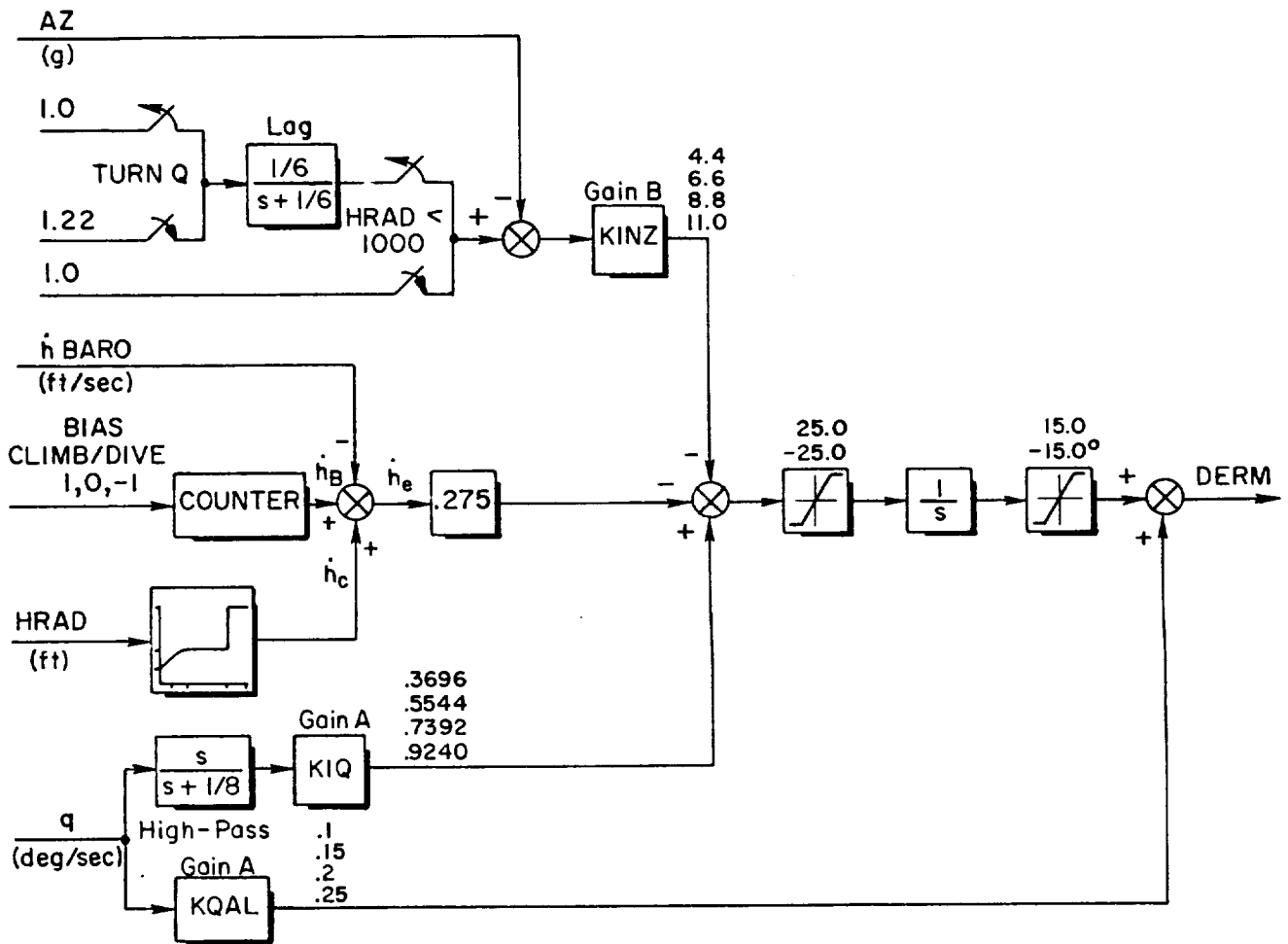
Figure 9. PA-30 Pitch Autoland Mechanization
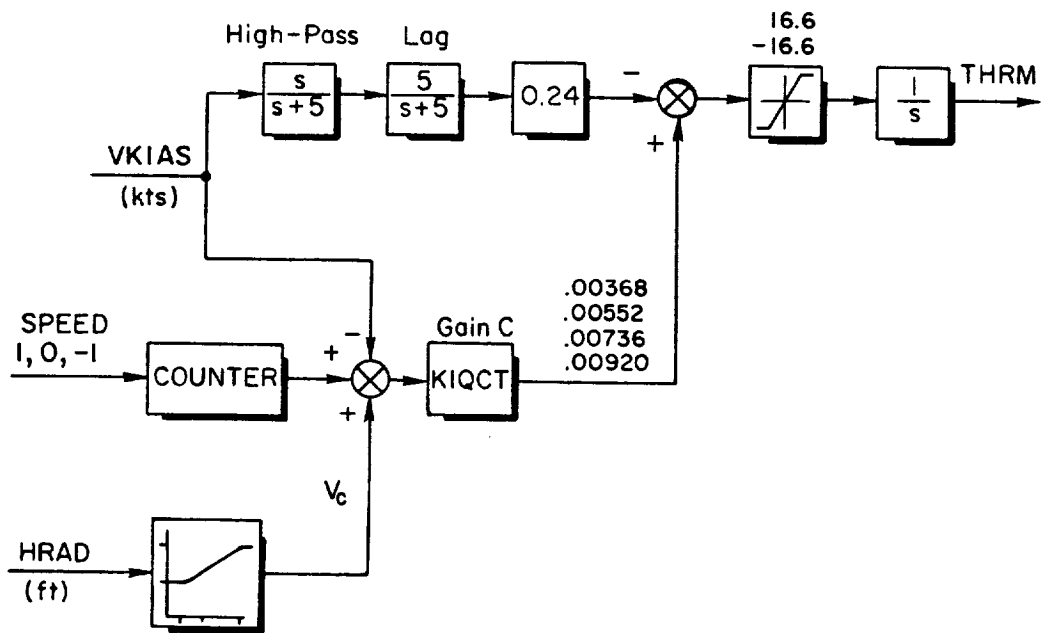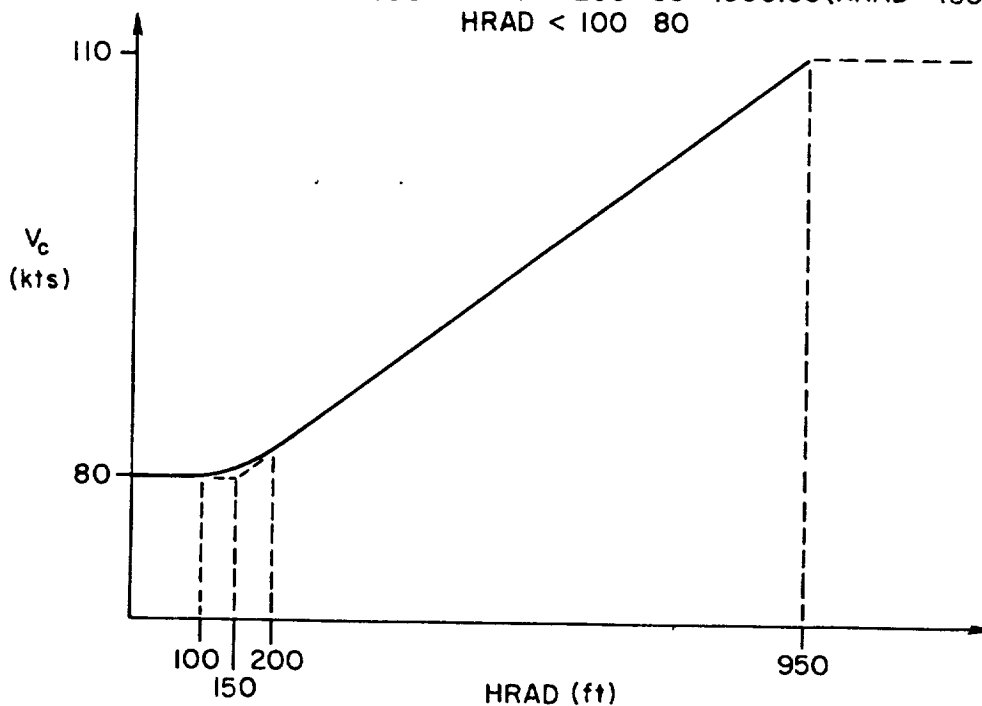
Figure 10. PA-30 Autothrottle Mechanization

TABLE 2.   THREE PHASES OF PRESENT BCS AUTOFLARE
AS MECHANIZED ON PA-30

Ⓐ — constant speed descent region

$h_R > 950$ ft

$\dot{h} = -1000$ ft/min

$V_a = 110$ kts (airspeed)

Ⓑ — deceleration region

150 ft $< h_R < 950$ ft

$\dot{h} = -500$ ft/min

V_a decreases linearly with h_R from 110 ft to 80 kt

Ⓒ - flare region

$0 < h_R < 150$ ft

$|\dot{h}|$ decreases linearly with h_R from -500 ft/min to -45 ft/min

$V_a = 80$ kt
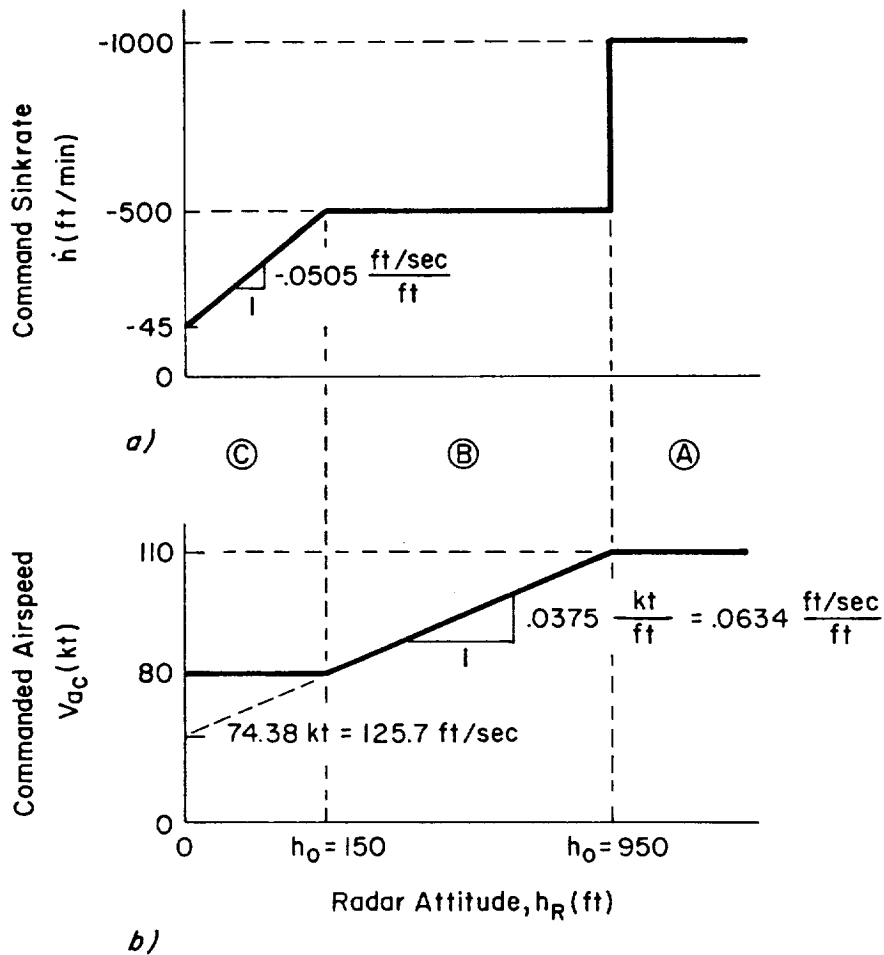
Figure 11. Simplified Sink Rate and Airspeed Schedules

If the system works perfectly, the sink rate error is near zero, i.e.,

$$\dot{h}_\epsilon \doteq 0$$

Thus, the sink rate closely follows the $\dot{h}$ schedule

$$\dot{h}_{BARO} \doteq \dot{h}_c = -500 \text{ ft/min} = -8.333 \text{ fps} \qquad (2)$$

Since the sink rate is constant in the deceleration region, the altitude is

$$h = \int_0^t \dot{h} \, dt + h_D$$

$$= h_D + \dot{h}t$$

$$= 950 - 8.333t \text{ ft} \tag{3}$$

where $t = 0$ @ $h_D = 950$ ft. Thus, over the deceleration region from 950 ft to 150 ft, the altitude change, Δh, is

$$\Delta h = 150 - 950 = -8.333 \, t_o \tag{4}$$

from which

$$t_o = 96.0 \text{ sec}$$

at start of flare (independent of wind).

The throttle loop may be considered in a similar fashion resulting in

$$V_a \doteq V_{a_c}$$
$$\tag{5}$$
$$= 125.7 + 0.0634 \, h_R \text{ fps}$$

The primary source of variation in touchdown point will be due to the effect of steady winds and thus in the following idealized analyses we consider only steady horizontal winds (independent of altitude.)

a. Velocity Relations

The basic velocity relations are shown in Fig. 12 according to the above assumptions. This diagram is shown for positive flight path angles, i.e., climb; however, the relations will also apply to descent
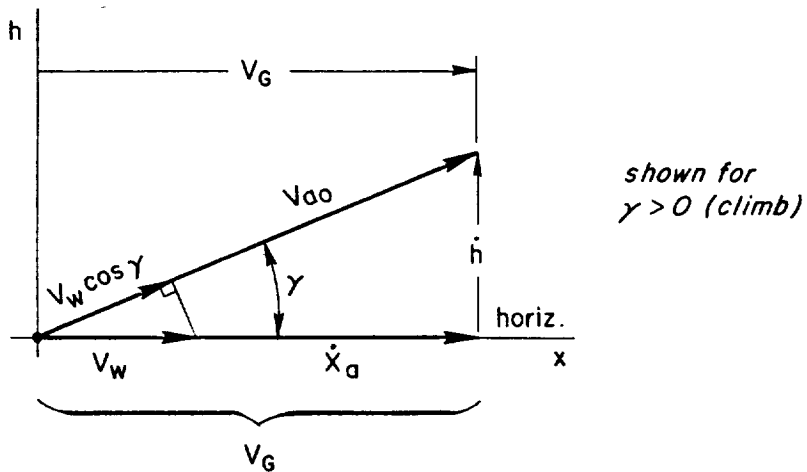
Figure 12. Velocity Relations

flight conditions. Since the flight path angle γ will always be small (i.e., a few degrees) the ground speed may be readily approximated as simply the algebraic sum of the wind speed and aircraft airspeed

$$V_G = V_w + \dot{X}_a \tag{6a}$$

$$\doteq V_w + V_a \tag{6b}$$

where V_w is the velocity of the airmass with respect to the ground, V_a is the velocity of the aircraft with respect to the moving airmass. The sink rate is then given by Eq. 7

$$\dot{h} = V_G \tan \gamma \tag{7a}$$

$$\doteq (V_w + V_a)\gamma \tag{7b}$$

b. Horizontal Distance Traveled

The horizontal distance traveled in the deceleration region is directly affected by windspeed and is

$$X = \int_0^t V_G dt = \int_0^t (V_W + 125.7 + 0.0634h)dt$$

$$= (V_W + 125.7)t + 0.0634 \int_0^t (950 - 8.333t)dt$$

$$= (V_W + 185.9)t - 0.2642 \, t^2 \tag{8}$$

Deceleration region trajectories computed from Eqs. 3 and 8 are plotted in Fig. 13 for the no wind condition and for 30 kt head and tail winds. The curvature seen in the trajectories is a consequence of the steady reduction in airspeed according to the schedule of Fig. 11 combined with a constant sink rate. The horizontal distance traveled in the deceleration region X_0 is found from Eq. 8 evaluated at $t_0 = 96$ sec.

$$X_0 = 96 \, V_W + 15,412 \text{ ft} \tag{9}$$

X_0 is plotted in Fig. 14 as function of windspeed. The flight path angle at the end of the deceleration region, γ_0 is found from Eq. 7b and as

$$\gamma_0 = \frac{\dot{h}}{V_W + V_{a_0}} = \frac{8.333}{V_W + 135.2} \tag{10}$$

and is also plotted as a function of windspeed in Fig. 14.

c. Idealized System Response in Flare

In the flare region the idealized sink rate response is (from Figs. 9 and 11):
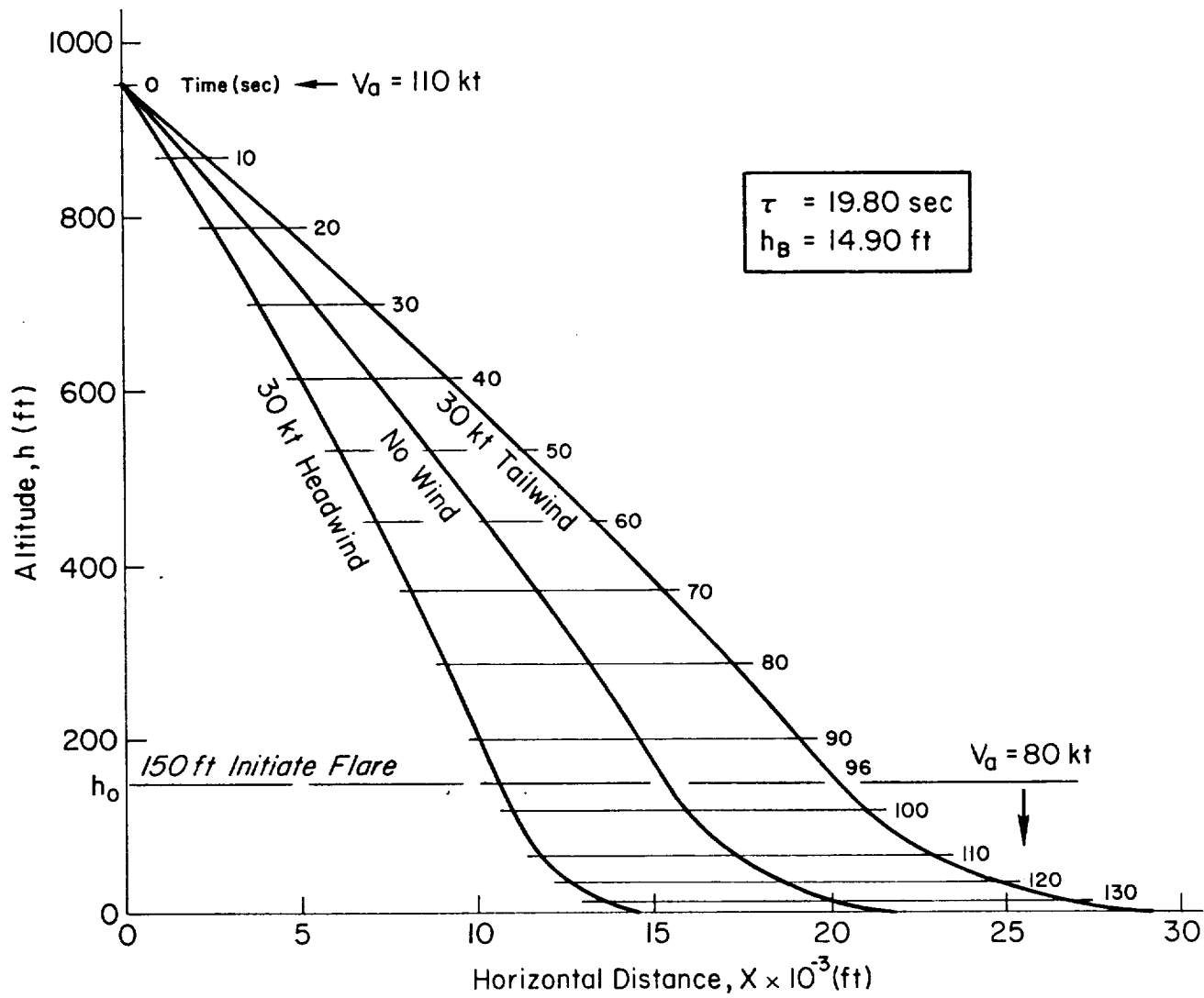
Figure 13. Effect of Horizontal Winds on Existing
"HIMAT BCS" in PA-30
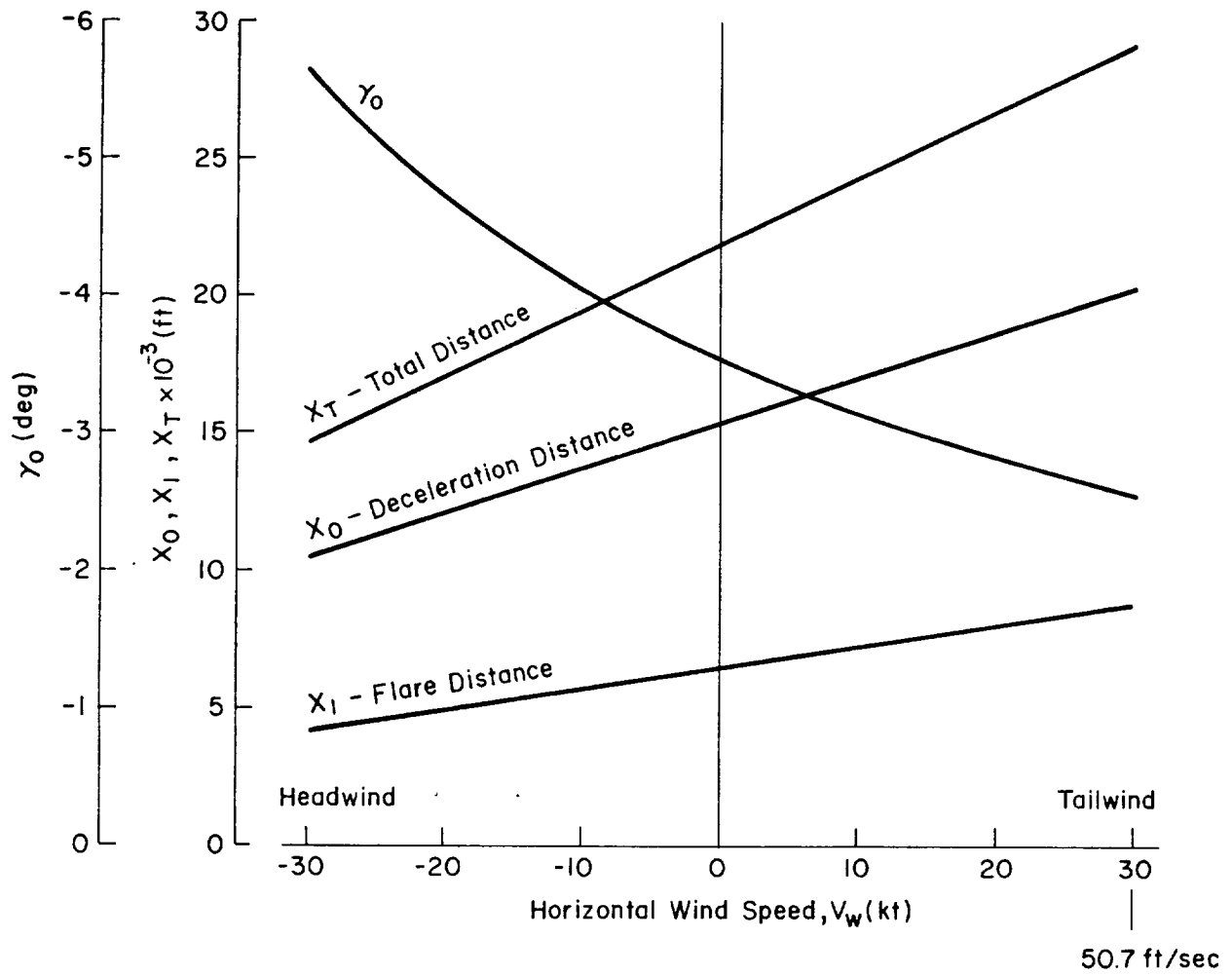
Figure 14. Effect of Wind Speed on Horizontal Distance Travelled

$$\dot{h}_\varepsilon = -\dot{h}_{BARo} - \dot{h}_c - \dot{h}_{BIAS}$$

$$= -\dot{h} - 0.0505h - 0.75 \doteq 0$$

$$\tag{11}$$

$$= \dot{h} + 0.0505(h + 14.9)$$

$$= \dot{h} + \frac{1}{\tau}(h + h_B) \doteq 0$$

where the flare time constant is:

$$\tau = \frac{1}{K_h} = \frac{1}{0.0505} = 19.80 \text{ sec}$$

and K_h is set by the 80 kt airspeed, no wind flare condition.

The ordinary first order differential equation in Eq. 11 forms an initial value problem to define the flare trajectory when combined with two initial conditions.

$$h(0) = h_o = 150 \text{ ft} \tag{12}$$

$$\dot{h}(0^+) = \dot{h}(0^-) = -8.333 \text{ fps} \tag{13}$$

where now t is measured from the start of flare. It should be noted that while the sink rate in Eq. 13 is independent of wind the corresponding flight path angle will not be. These two initial conditions require the continuity of altitude and glideslope at the deceleration/flare interface. Laplace transforming Eq. 11

$$\left(sh(s) - h(0)\right) + \frac{1}{\tau}h(s) = -\frac{1}{\tau}\frac{h_B}{s} \tag{14a}$$

$$h(s) = \frac{h_o}{(s + 1/\tau)} - \frac{h_B/\tau}{s(s + 1/\tau)} \tag{14b}$$

Inverse Laplace transforming gives the altitude as function of time

$$h(t) = h_0 e^{-t/\tau} - h_B(1 - e^{-t/\tau}) \tag{15a}$$

$$= (h_0 + h_B)e^{-t/\tau} - h_B \tag{15b}$$

$$= 164.9 \, EXP(-t/19.8) - 14.9 \tag{15c}$$

d. Time for Touchdown t_1

The elapsed time to touchdown measured from the start of flare, t_1, is derived as follows.

$$h(t_1) = (h_0 + h_B) \, e^{-t_1/\tau} - h_B = 0 \tag{16a}$$

$$e^{-t_1/\tau} = \frac{h_B}{h_0 + h_B} \tag{16b}$$

$$t_1 = -\tau \ln \left(\frac{h_B}{h_0 + h_B} \right)$$

$$= -19.80 \, \ln \left(\frac{14.9}{150 + 14.9} \right) = 47.6 \, sec \tag{17}$$

e. Altitude Bias, h_B

The altitude bias, h_B, in Eq. 11 is used to set the altitude below the runway for the zero sink rate asymptote (see Fig. 15) positive values of h_B, insure that the sink rate at touchdown will be greater than 0, i.e., $\dot{h}(t_1) < 0$.
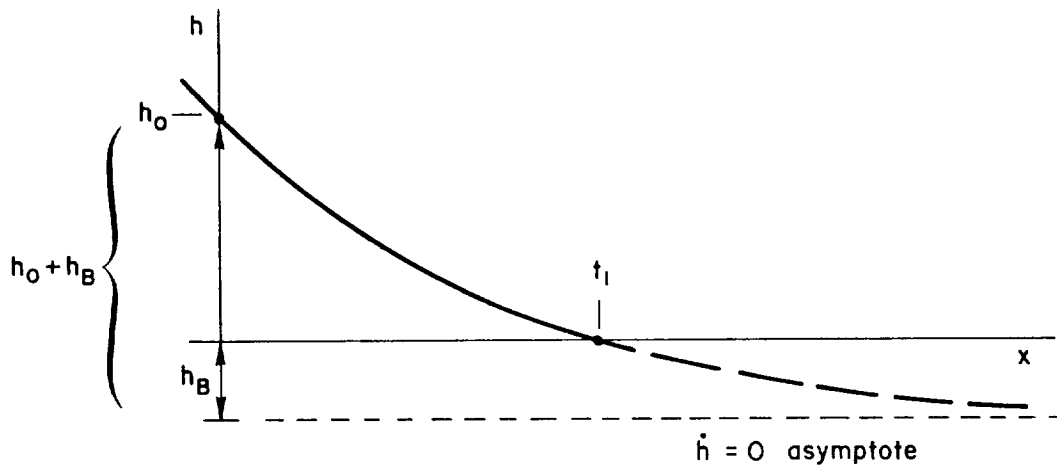
Figure 15. Definition of h_B

f. **Sink Rate at Touchdown**

From differentiation of Eq. 15 the sink rate at touchdown is

$$\dot{h}(t_1) \quad = \quad -\left(\frac{h_o + h_B}{\tau}\right) e^{-t_1/\tau}$$

$$= \quad -\left(\frac{h_o + h_B}{\tau}\right)\left(\frac{h_B}{h_o + h_B}\right)$$

$$= \quad -\frac{h_B}{\tau} \quad = \quad \text{constant} \tag{18}$$

From the preceding, it may be seen that the altitude variation, the time for touchdown, and the sink rate at touchdown are all independent of windspeed.

g. **Horizontal Travel in Flare**

The horizontal distance traveled during flare (measured from flare initiation) is

$$X(t) = V_G t = \left(V_w + V_{a_o}\right)t = (V_w + 135.2)t \qquad (19)$$

where V_{a_o} is a constant 135.2 fps (80 kts) during flare. The distance traveled in flare to touchdown, X_1, is

$$X_1 = V_G t_1$$

$$= (V_w + 135.2)(47.6) \qquad (20)$$

Thus, the distance traveled in flare _is_ a function of windspeed and is plotted in Fig. 14. The total distance traveled in the deceleration and flare regions X_T, is obtained by summing Eqs. 9 and 20, i.e.

$$X_T = X_o + X_1$$

$$= 143.6 \, V_w + 21,848 \qquad (21)$$

The total distance is also plotted in Fig. 14.

h. Summary

While this mechanization produces quite acceptable sink rates at touchdown, the landing dispersions are highly dependent upon initial approach alignment and the direction and magnitude of atmospheric disturbances. Furthermore, the ground pilots view of the landing through the TV monitor will vary from landing to landing because of these same alignment and atmospheric factors. This makes it difficult for the pilot to monitor for proper autoflare and generally contributes to the

requirement for several practice approach and landings with the PA-30 aircraft just prior to each HIMAT flight.

2. Lateral/Directional Mechanization

PA-30 autoland roll and yaw axis mechanization block diagrams are presented in Figs. 16 and 17, respectively.

Unfortunately, there is no onboard lateral flight path sensor for the roll or yaw axis during autoflare as is the case for the longitudinal axis. Therefore the ground pilot must continue to perform this function via the T.V. display and uplink commands to the vehicle. The uplink inputs are discrete left or right yaw rate commands. The HIMAT backup control system is based on body angular rate sensors and has no direct measure of bank angle. However, since turn rate is directly proportional to bank angle in a coordinated turn, the yaw rate may be substituted for roll attitude. The roll axis mechanization is thus a turn rate command, zero turn rate hold system.

The ground pilot inputs discrete turn rate commands until the desired directional path is achieved and then, with the command removed, the roll axis controller attempts to maintain zero yaw rate from that desired directional path. The integral of yaw rate error is fed back to provide a tight control structure at low frequency, i.e., trim.

As noted previously, the yaw axis (Fig. 17) consists of a conventional washed out yaw rate damping feedback and a turn coordination circuit which combines washed out yaw rate with lagged lateral acceleration. That this provides turn coordination may be seen as follows:

$$\frac{K_1}{(s + 1)} a_y + \frac{K_2 s}{(s + 1)} r = \frac{K_1}{(s + 1)} \left(a_y + \frac{K_2}{K_1} \dot{r} \right)$$

Now if the lateral acceleration sensor is located along the vehicle x-axis and at the center of rotation for forces applied at the rudder, then it senses only vehicle translation and not rotation due to rudder deflection. This is the ideal sensor location for the signal to be used
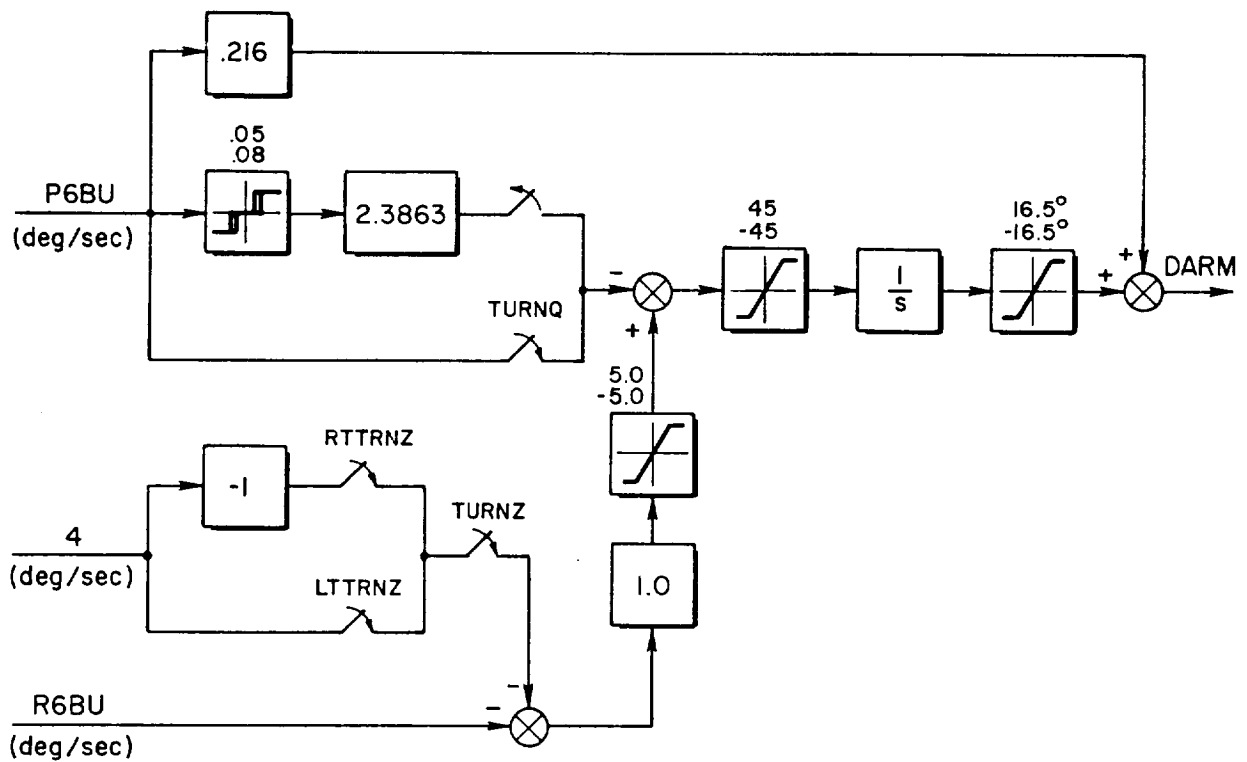
Figure 16. Roll Autoland (From Reference 6)
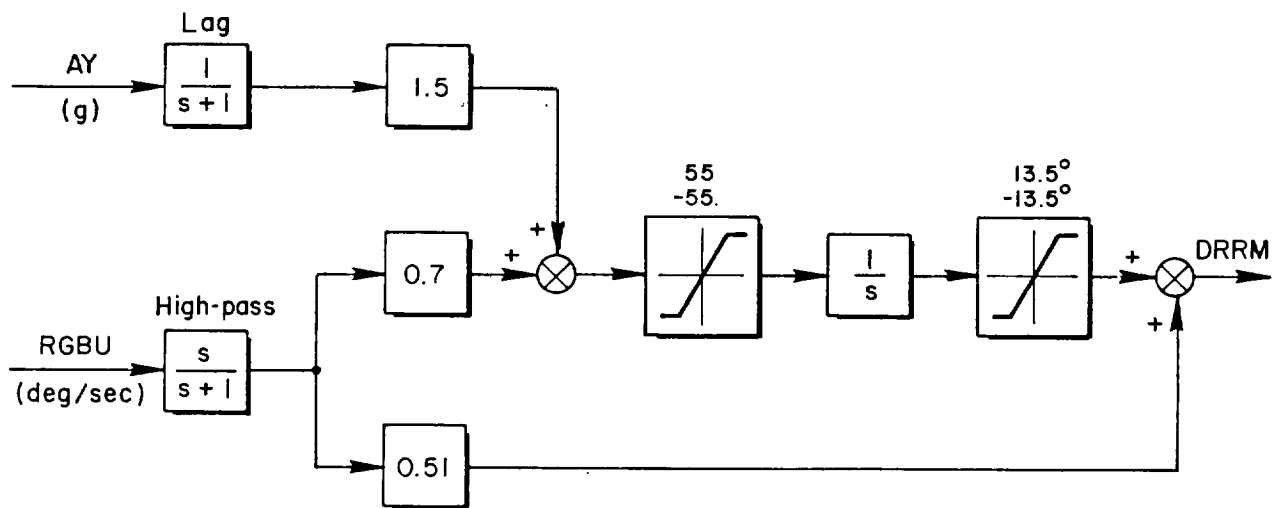
Figure 17. Yaw Autoland (From Reference 6)

for turn coordination and to be uncontaminated by rudder induced yaw acceleration due to the damper function. In simple terms

$$a_{y_{cg}} \doteq Y_v v + Y_{\delta_r} \delta_r$$

$$a_{y_s} = a_{y_{cg}} + X_a \dot{r}$$

$$\doteq Y_v v + Y_{\delta_r} \delta_r + X_a \dot{r}$$

and the accelerometer is located at a distance X_a from the c.g. for which the $X_a \dot{r}$ component will tend to offset the $Y_{\delta_r} \delta_r$ component. Then one is left with $Y_v v$ (or $Y_\beta \beta$) as the major part of the acceleration sensed. If the sensor cannot be placed at this ideal location due to physical constraints, then an equivalent signal can be synthesized by summing the sensor signals as noted above and with $K_2/K_1 = X_a$. The resulting signal is then integrated to to maintain zero v (or β) trim.

This overall lateral/directional mechanization would probably be adequate under absolutely calm wind and full, three dimensional vision conditions. However, in the presence of turbulence, crosswind, or wind shear, the bang–bang nature of the command makes precision path control impossible. The task is further complicated by the two dimensional display characteristics noted previously in Subsection A.3.

The Ref. 6 early PA-30 flight checkout verifies this assessment by specifically commenting that

> "it was difficult to control roll attitude, combat drift, etc."

and

> "the major piloting task of the autoland mode is the lateral heading control task."

An example of the lateral control imprecision and pilots' workload is given in Fig. 18 which has been taken from the Ref. 6 flight records.
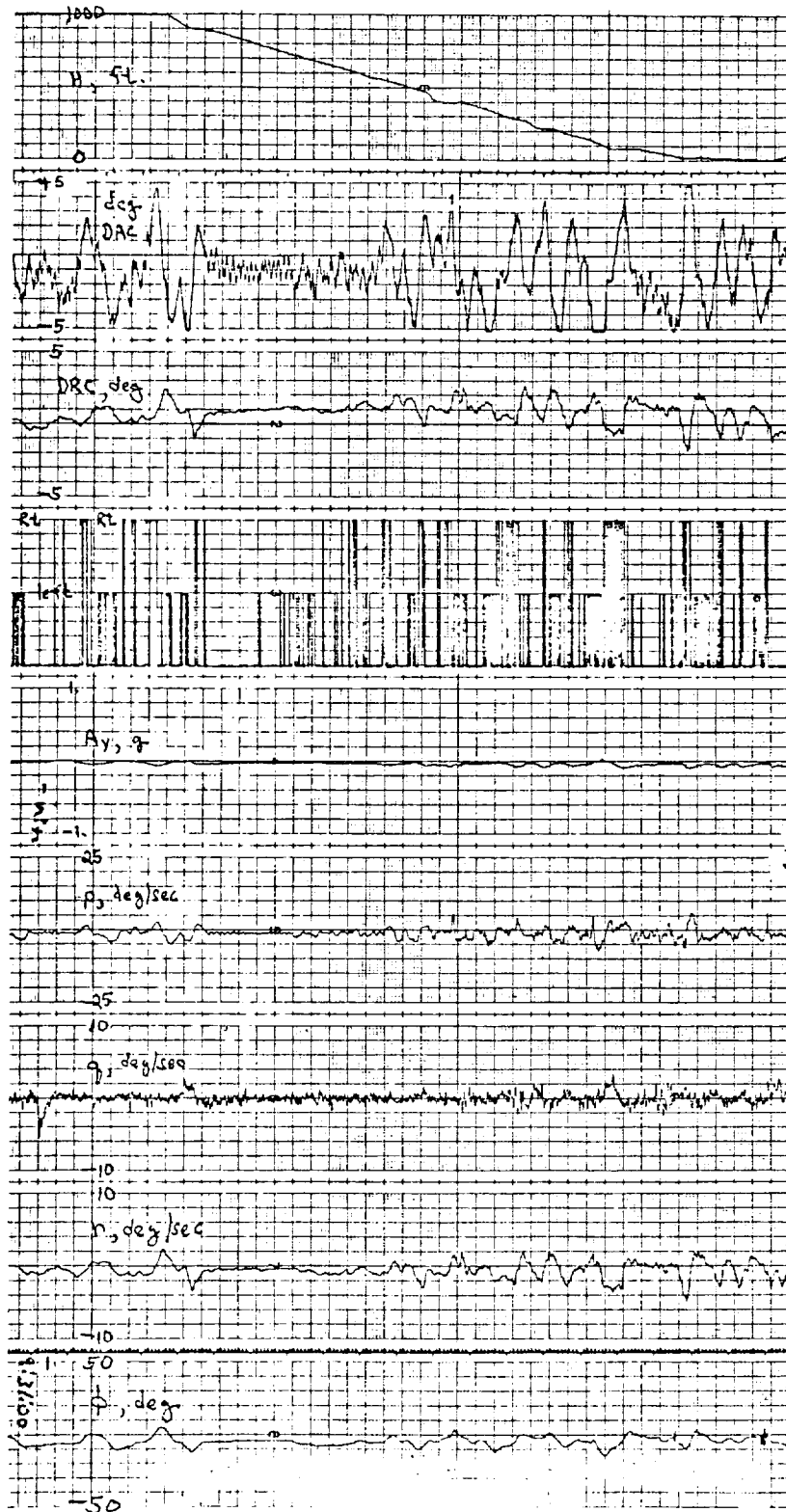
Figure 18. Lateral Autoland Response on Flight No. 11
3d Landing (Gains 421)

SECTION III

IMPROVED AUTOLAND CAPABILITY

One goal of this study is to synthesize an "improved" terminal control autoland capability for RPRV's (and the PA-30). The improvements sought involve both consistency of terminal conditions and easing of ground pilot workload. Further, in the interest of timely implementation potential and overall cost, it is desirable to make as much use of existing DFRF equipment and facilities as possible.

The essence of any good performing automatic landing and flare system lies in making the aircraft tightly track an approach beam and then wind proofing the flare to a smooth landing at a consistent touchdown point and touchdown sink rate. Thus, two separate automatic modes are involved in the "improved" autoland system: automatic beam tracking to produce consistent flare initiation conditions and an automatic flare mode which minimizes the influence of head, tail, and crosswind conditions encountered during the approach and flare. An additional consideration is minimization of any transients due to switching from the beam tracking to the autoflare mode. The end result is a vehicle/automatic controller system which greatly reduces ground pilot visual and mental workload by providing essentially invariant approach and landing conditions to monitor.

For the automatic beam tracking mode it is proposed that the present ground pilot station synthetic ILS flight director concept be extended to use the flight director needle command deflection signals as the basic deviation (or error) input to the flight control mechanization hosted in the ground computer. Otherwise the system operates on down-linked signals from onboard sensors and up-linked surface position commands as is now accomplished. Figure 19 pictures the concept in simplified block form consistent with Fig. 1.

For the improved autoflare mode the "variable τ" algorithm and mechanization developed by Boeing (Ref. 7) for the B-737 aircraft is
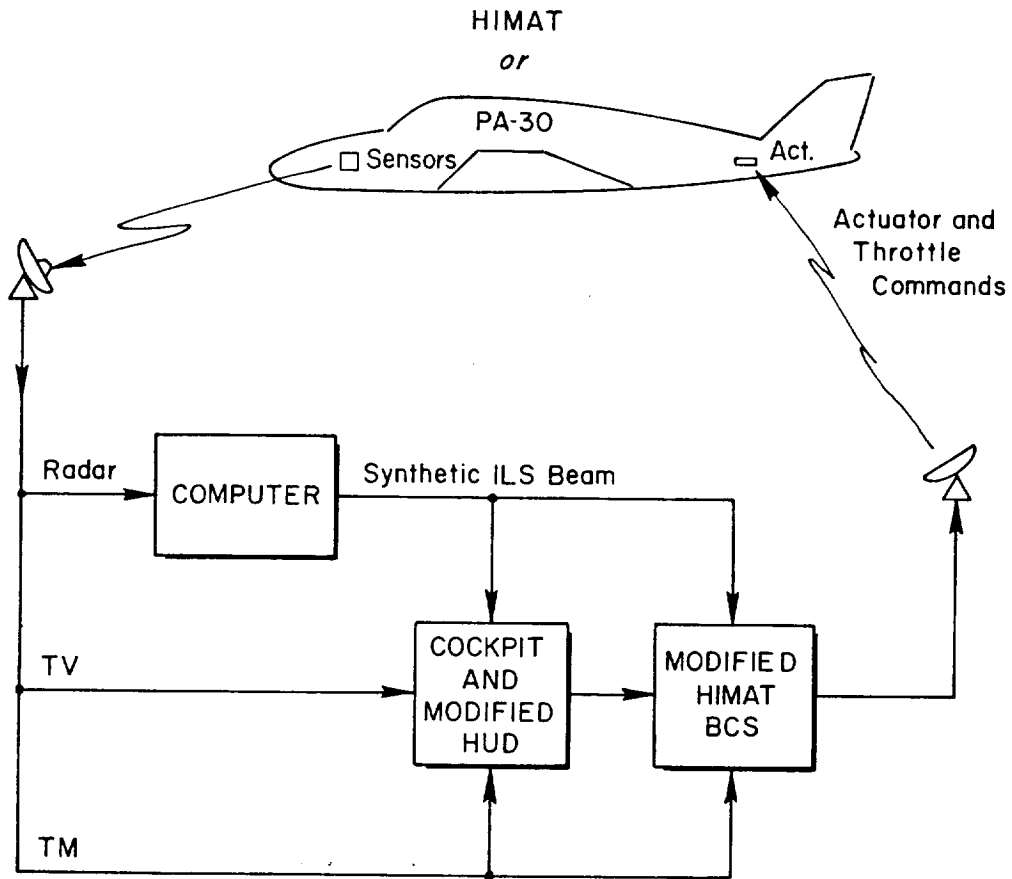
Figure 19. Improved Autoland System

adopted. In this system the time constant of the flare law (τ) is varied with ground speed to produce essentially invarient touchdown distance and sink rate from a given flare initiation height despite the presence of head or tail winds.

One of the main sources of touchdown dispersions for conventional flare laws using pre-fixed h and $\dot{h}$ gains is the sensitivity to approach ground speed as affected by steady winds. This sensitivity is due to the time exponential nature of altitude and sink rate decay during flare, resulting in a fixed flare <u>duration</u> from a given altitude. The flare distance from a given altitude will therefore be proportional to ground speed, which in turn depends upon the wind. A high flare initiation altitude compounts the problems.

Variation of h or $\dot{h}$ gains with ground speed produces different time exponential (variable τ) decay of altitude and sink rate such that longitudinal flare <u>distance</u> remains fixed at a cost of slight variation in sink rate at touchdown.

Incorporation of ground speed correction generally is considered to require an onboard inertial navigation sensing package which would be too costly and bulky for RPRV (or PA-30) application. Fortunately, Boeing (Ref. 7) has already addressed this problem for their B-737-200 and developed an autoflare law which utilizes a "pseudo" measure of ground speed. Additional features of the Boeing longitudinal mechanization are the provision of pre-flare glideslope tracking, transient free transition from glideslope tracking to flare initiation and incorporation of runway referencee, radar altitude rate ($\dot{h}_R$) for the flare. Thus, this mechanization incorporates all the features desired for the RPRV improved longitudinal approach and autoland modes. For the lateral axis a rather simple beam tracking, wings level, flare mechanization such as employed in the Lockheed L-1011 and Compass Cope is proposed.

The following subsection describes the longitudinal mechanization in more detail. Idealized system performance is then presented in the next subsection for comparison with the current autoland responses discussed in Section II. The third subsection describes the proposed lateral system mechanization.

A. LONGITUDINAL BEAM TRACKING AND AUTOFLARE

1. Mechanization

A block diagram of the proposed mechanization is presented in Fig. 20. Except for the glideslope error (h_{GSE}) input, all sensed parameters are the same as in the present autoflare mechanization (Fig. 9). Switching and signal fading between modes is on the basis of a pre-selected, runway referenced, flare initiation radar altitude, h_{R_o}, as follows:

a. $h_R > h_{R_o}$

The beam tracking mode is a conventional proportional plus integral system. Note that when $h_R > h_{R_o}$, $K_{GSE} \equiv 1$, h_{RL} is constant (limit value) and the integral gain is $K_{I_e} K_{h_R} h_{RL}$. The integral path nulls the beam deviation error while the lagged normal acceleration and pitch rate feedback paths provide, respectively, heave error and short period attitude damping. The latter two feedbacks are of the same form as in the present autoland deceleration and flare mechanization.

The additional derived sink rate feedback path, $\hat{\dot{h}}$, provides the "pseudo" measure of ground speed. This may be noted by observing that in the steady state (above $h_{R_{limit}}$):

$$h_{RL} = \text{constant}$$

$$h_{RL} \left(\frac{s}{T_F s + 1} \right) = 0$$

$$\hat{\dot{h}} = \dot{h}_{bias} + \left\{ \frac{T_F s}{(T_F s + 1)} + \frac{1}{(T_F s + 1)} \right\} \dot{h}_{CF}$$

$$= \dot{h}_{bias} + \frac{(T_F s + 1)}{(T_F s + 1)} \dot{h}_{CF}$$

Figure 20. Integrated Glide Slope/Variable Tau Flare Control Law

38

$$= \dot{h}_{bias} + \dot{h}_{CF}$$

Thus, $\hat{\dot{h}}$ is proportional to complementary filtered barometric altitude rate as the vehicle descends the glideslope plus a small bias to assure a firm touchdown rate. Since the glideslope is fixed with respect to the ground, the rate of descent along the glideslope is proportional to vehicle ground speed, i.e. $\dot{h} = V_G \tan \gamma$. The $\hat{\dot{h}}$ feedback provides a beam deviation bias which initially causes the vehicle to fly above the glideslope until the $\hat{\dot{h}}$ signal is cancelled by the integral of beam error path. Therefore the output of the integrator becomes proportional to vehicle ground speed in the steady state descent along the glideslope.

b) $h_R < h_{R_0}$ — When the flare initiation altitude is reached several things happen simultaneously to rapidly and smoothly transition the system into the autoflare mode. First, in the beam tracking path, the gain K_{GSE} is rapidly faded to zero so that the integrator output, K_{I_e}/s, holds its output (which is proportional to ground speed, V_G, at the time of changeover). Secondly, the h_{RL} signal comes off its limit value and starts to decrease. Thirdly, the switch opens in the first order lag path of the complementary filtered altitude rate, $\dot{h}_{CF}$, and the signal in this path starts to decay at a time constant T_F. At the same time the decreasing radar altitude, h_{RL}, passing through the washout circuit produces a signal proportional to $\dot{h}_R$. The two rate signals complement one another to produce up elevator to initiate the flare, i.e.,
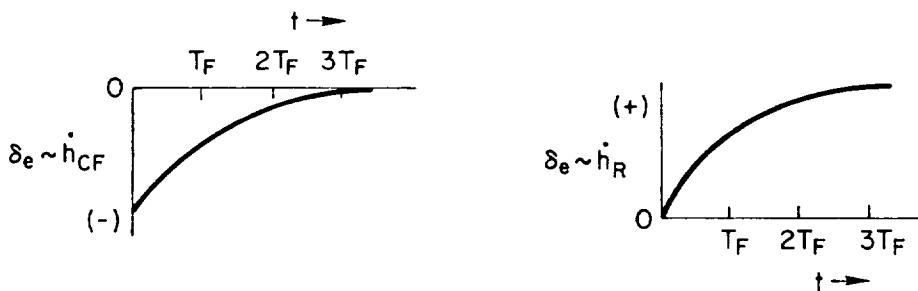
Thus, the signals produce a smooth transition to an autoflare system that is completely runway referenced within three time constants, T_F, after flare initiation.

The variable τ autoflare block diagram may then be considered in the simplified form shown in Fig. 21. The elevator command for flare, δ_{e_F}, is

$$\delta_{e_F} = K_{h_R}V_G h_R + \frac{s}{(T_F s + 1)} h_R + \frac{T_F s}{(T_F s + 1)} \dot{h}_{CF} + \dot{h}_{BIAS}$$

$$\doteq K_{h_R}V_G h_R + \dot{h}_R + T_F \ddot{h}_{CF} + \dot{h}_{BIAS}$$

$$\doteq K_{h_R}V_G \left(\frac{s}{K_{h_R}V_G} + 1\right) h_R + \dot{h}_{BIAS} + T_F \ddot{h}_{CF}$$

$$\doteq K_{h_R}V_G(\tau s + 1) h_R + \dot{h}_{BIAS} + T_F \ddot{h}_{CF}$$
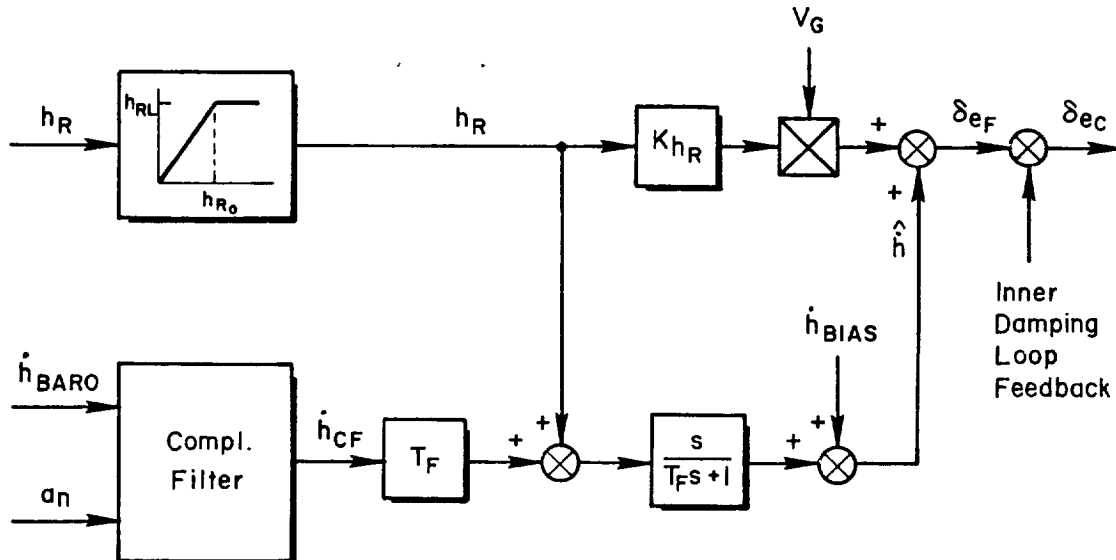
Figure 21. Simplified Autoflare Block Diagram

where $\tau = 1/K_{h_R}V_G$ is the ground speed "variable tau" and the contribution through the complementary filter is primarily a smoothing term.

The end result is a full runway reference, ground speed adjusted flare law. Example flare trajectories from the Ref. 7 B-737 performance assessment with wind variation from -15 to +25 kts are shown in Fig. 22. While the insensitivity of the touchdown point to wind is quite apparent, it should be noted that the slight variation in flight paths will result in similar variation in sink rates at touchdown. These aspects will be assessed in greater detail in the next subsection.

As a final note, in addition to achieving the desired performance goals the mechanization also is compatible with the existing HIMAT BCS (and PA-30) autoflare mechanization. Figure 23 shows the present autoflare (mechanized for the PA-30) as solid lines and the paths and blocks necessary to incorporate the integrated glideslope/variable tau flare laws in dashed lines. The improved system requires only a minimum of added circuitry plus incorporation of the glideslope error input. The circuitry could be built into the onboard backup control system with the GSE signal transmitted via up-link. Since all other sensors are already onboard, loss of the up/down communication link could automatically result in the system reverting to the present HIMAT/PA-30 autoflare configuration as a part of an autononous landing configuration.

2. Idealized Performance

The present system is subject to significant variation in touchdown point in steady winds as shown in Figs. 13 and 14. In this section it will be shown that this problem may be essentially eliminated by use of the proposed system which employs automatic tracking of the synthetic ILS followed by a "variable τ" flare law.

The idealized trajectory for the proposed system is shown in Fig. 24. It will be demonstrated that for the proposed system:

- The trajectory is completely defined by specifying h_D, γ_0, flare airspeed (V_{a_0}), zero wind flare time constant (τ_0) and touchdown sink rate ($\dot{h}(t_1)$).
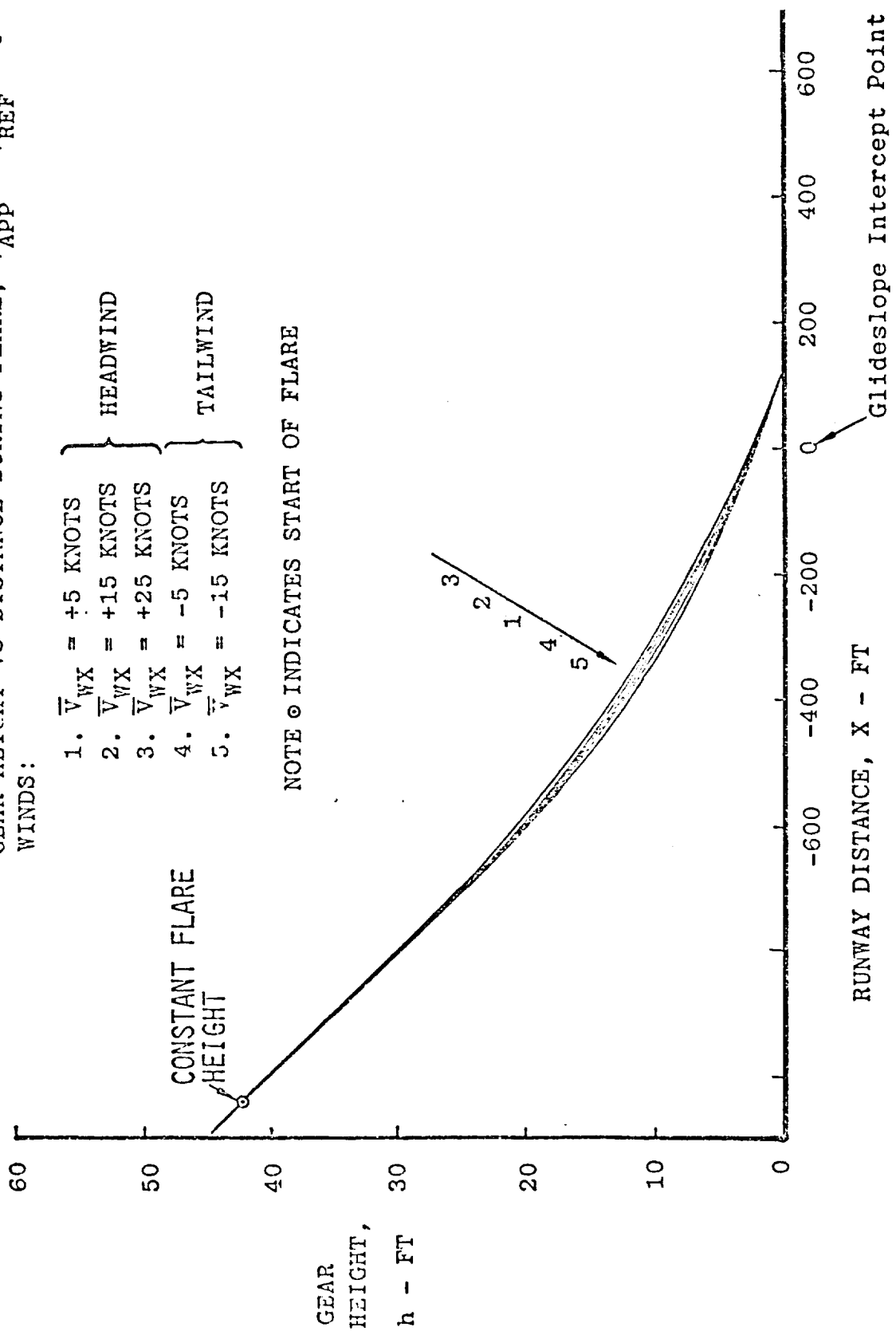
Figure 22. "Variable Tau" Flare Law Performance for Various Approach Groundspeeds Due to Wind
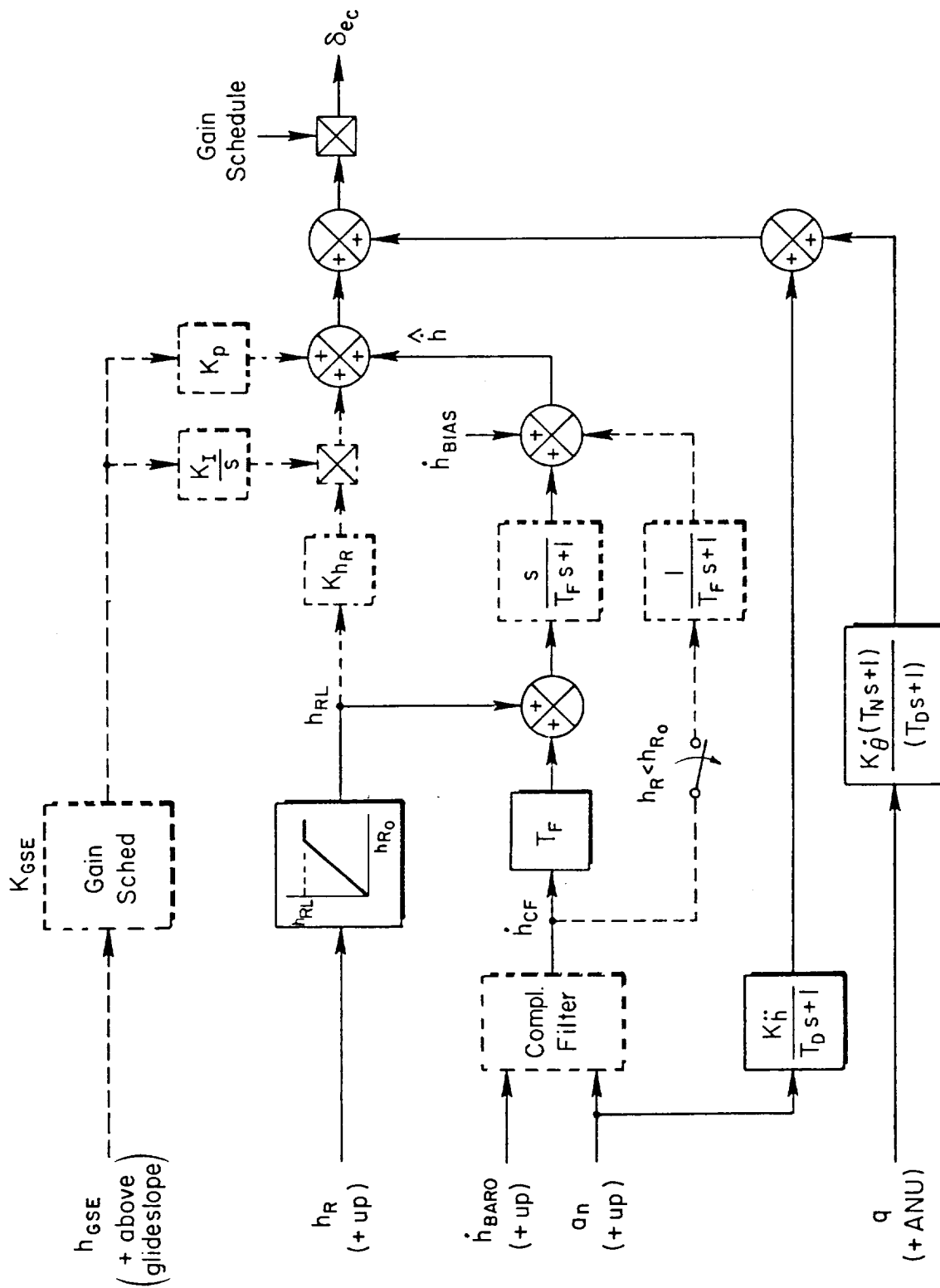
Figure 23. Compatibility of Present and Proposed Autoflare Mechanizations
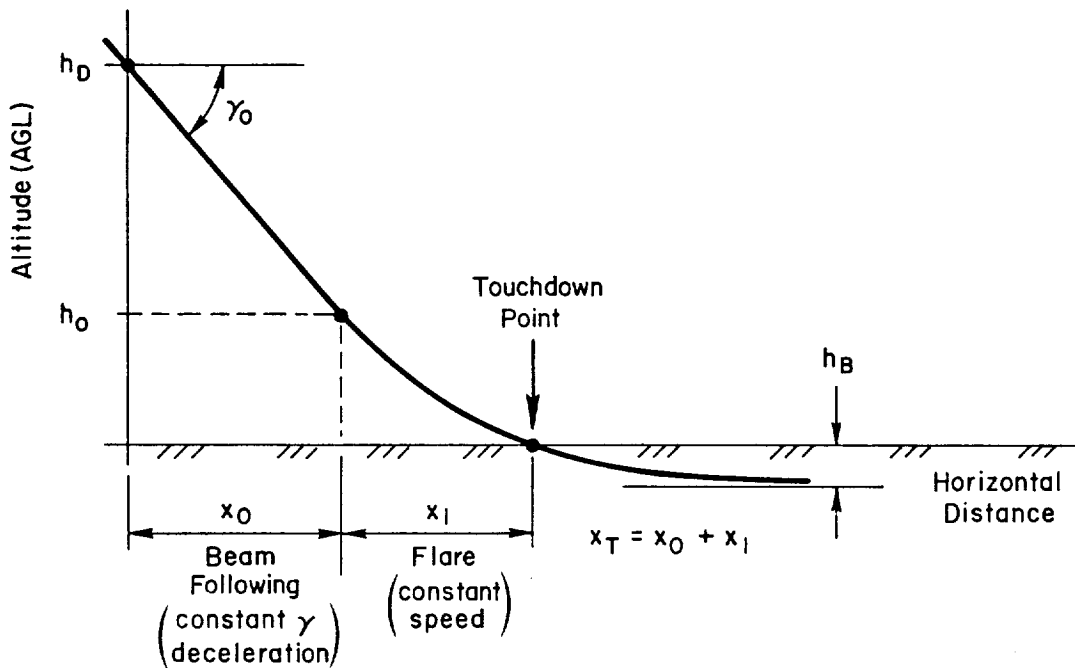
Figure 24. Trajectory for Proposed System

- Once defined, the trajectory shape is invariant with wind, in particular, h_o is independant of wind but <u>does</u> vary with choice of τ_o, V_{a_o}, γ_o, and $\dot{h}(t_i)$.

- Unlike the existing system, touchdown time and touchdown sink rate <u>do</u> vary with wind velocity, but not significantly.

- The proposed and existing system always have (slightly) different flight paths before flare if deceleration occures during the approach phase.

a. Synthetic ILS Beam Following

For purposes of comparison with the preceeding analysis of the existing system, it will be assumed in the following that the ILS tracking region coincides with the deceleration region and that transition to flare is made at $h_o = 150$ ft as in the existing schedule. These assumptions are <u>not</u> necessary and perhaps not even desirable for the actual implementation of this system but will be used here only for purposes of comparison. It is shown in Appendix D that the speed and altitude

schedules can generally be considered independent and that the beam tracking system should perform adequately either at constant speed or with a scheduled speed variation in the region between 110 kts and 80 kts as used in the present PA-30 schedule, Fig. 11. The total distance traveled in the beam tracking deceleration region, X_o, is:

$$X_o = \left(\frac{h_o - h_D}{\tan \gamma_o}\right) \doteq \left(\frac{h_o - h_D}{\gamma_o}\right) > o \qquad (22)$$

where $h_o = h_o (\tau_o, V_{a_o}, \gamma_o, \dot{h}(t_1))$ will be determined in the next section.

b. Variable τ Flare Law Ideal Altitude Response

As noted previously, the "variable τ" flare law concept is used to fix the flare trajectory in space essentially independent of wind by making the flare time constant τ a function of windspeed. The time constant τ is therefore redefined as

$$\tau = \tau_o \frac{V_{G_o}}{V_G} \qquad (23)$$

where τ_o, V_{G_o} are the no wind parameters. Following Ref. 8 Eq. 23 is substituted into Eq. 11 multiplied by $1/K_h$ giving

$$\frac{\tau_o V_{G_o}}{V_G} \frac{dh}{dt} + (h + h_B) = 0 \qquad (24)$$

Since

$$\frac{dh}{dt} = \frac{dh}{dx} \frac{dx}{dt} = \frac{dh}{dx} V_G \qquad (25)$$

Eq. 24 becomes

$$\tau_o V_{G_o} \frac{dh}{dx} + (h + h_B) = 0 \qquad (26)$$

Equation 26 is an ordinary differential equation in spatial variables for the flare trajectory and is independent of steady wind. By analogy to Eq. 15b

$$h(x) = (h_o + h_B) e^{-x/\tau_o V_{G_o}} - h_B \qquad (27)$$

where x is measured from the flare initiation point.

c. **Initial and Final Trajectory Points**

Since Eq. 27 is independent of wind, the flare initiation height, h_o and touchdown distance, X_1, measured from flare initiation are independent from wind also. From Eq. 24, evaluated at the start of flare,

$$h_o = -\frac{\tau_o V_{G_o}}{V_G} \dot{h}_o - h_B$$

$$= -\frac{\tau_o V_{G_o}}{V_G} (V_w + Va_o) \gamma_o - h_B$$

$$\doteq -\tau_o Va_o \gamma_o - h_B \qquad (28)$$

(recall that $Va_o \doteq V_{G_o}$)

Thus, Eq. 22 becomes

$$X_o = -\tau_o Va_o - \left(\frac{h_B + h_D}{\gamma_o} \right) \qquad (29)$$

From Eq. 27 evaluated at touchdown (h = 0)

$$X_1 = -\tau_o V_{G_o} \ln \left(\frac{h_B}{h_o + h_B} \right)$$

$$= -\tau_o Va_o \ln \left(\frac{-h_B}{\tau_o Va_o \gamma_o} \right) \qquad (30)$$

Using the PA-30 values of $\tau_0 = 19.8$ spec, $h_B = 14.9$ ft, and $Va_0 = 80$ kts as in Section II; X_0, X_1, h_0 and X_T are plotted as functions of the glideslope at flare initiation γ_0 in Fig. 25. The ideal flare trajectory as defined by Eq. 27 is identical for all wind speeds, however, the actual system with additional feedbacks and finite bandwidth for the various feedback loops will show some slight variation in trajectory with windspeed, e.g., Fig. 22; however, this variation is very small compared to that for the existing BCS system and thus the preceding analysis is quite adequate for assessing the proposed system.

d. Comparison Trajectories for Proposed and Existing Systems

It is difficult to directly compare the proposed system with the existing BCS autoflare as implemented on the PA-30 because even the idealized trajectories have slightly different shapes. Specifically the constant $\dot{h}$ region in the existing system produces a curved trajectory if deceleration occurs (see Fig. 13). Probably the most meaningful way of comparing the two systems is to specify the same sink rate at touchdown (no wind) for both systems. As will be shown shortly, this will occur if h_B and $\tau = \tau_0$ are the same for the two systems. If the flare airspeed, V_{a_0}, and the flight path angle at flare initiation are also the same, the shape of the flare trajectory of the proposed system in any wind will be the same as for the existing system with no wind. This may be seen in Fig. 25 by noting that the h_0 and X_1 values for the proposed system correspond to the existing system values with no wind at the appropriate $\gamma_0 = -3.5$ deg.

Because of the slight difference in shape of the trajectories before flare in the two systems, they differ in X_0 and X_T for $\gamma_0 = -3.5$ deg. It may be seen that the total travel for the proposed system will be several thousand feet less.

e. Sink Rate at Touchdown for the Variable τ System

As noted above, spatial quantities such as touchdown distance and flare initiation height are ideally independent of wind speed for the
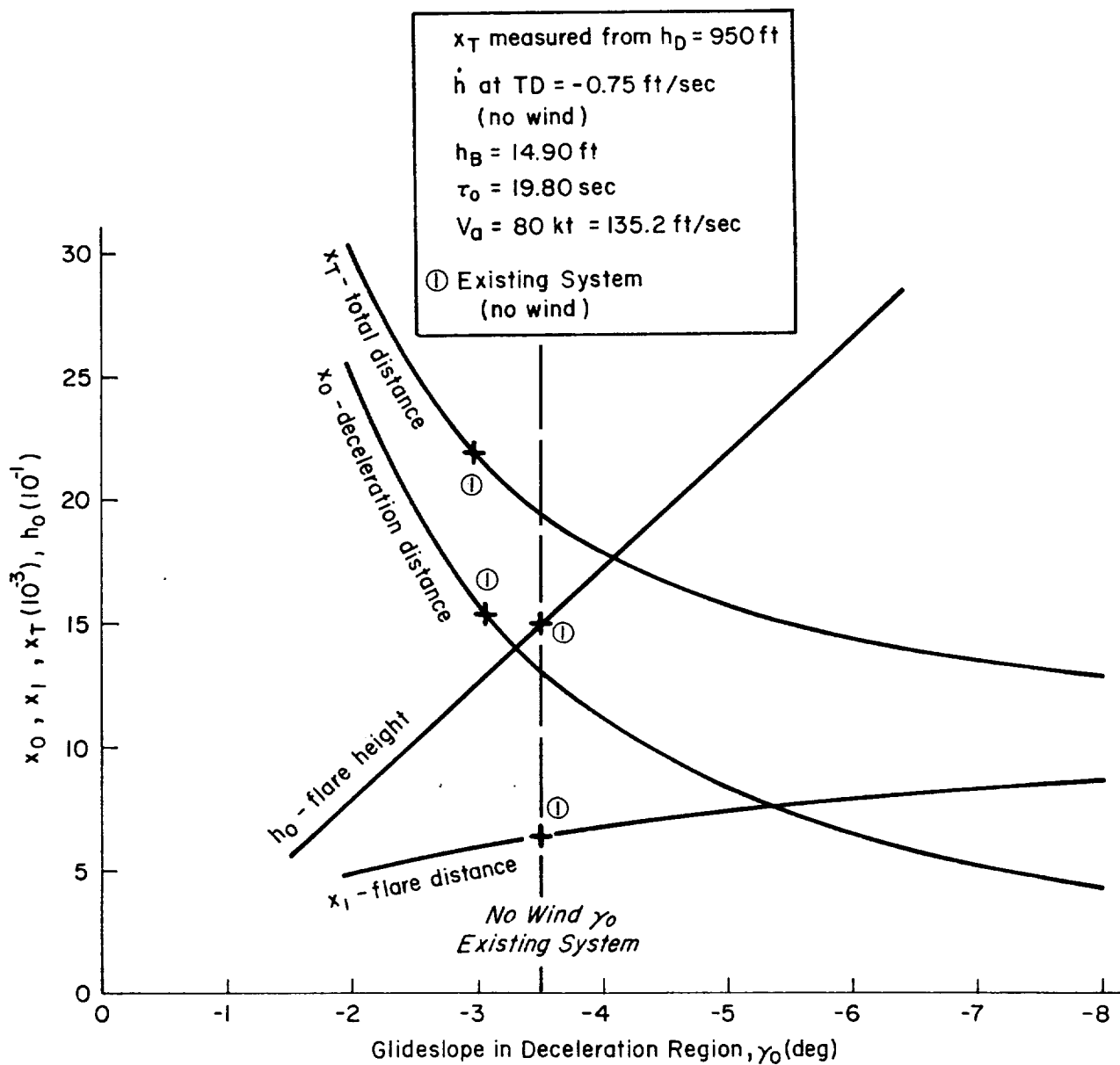
Figure 25. Effect of γ_0 on 'Variable τ' Trajectory

variable τ system. However, time dependent quantities such as sink rate at touchdown and touchdown time do vary with wind speed, a situation which differs from the present BCS autoflare law. The sink rate at touchdown may be derived from Eq. 24 by setting h = 0.

$$\dot{h}(t_1) \;=\; -\,\frac{h_B V_G}{\tau_o V_{G_o}}$$

$$=\; -\,\frac{h_B}{\tau_o}\left(1 + \frac{V_w}{Va_o}\right) \tag{31}$$

As may be seen from Eq. 31, the sink rate at touchdown varies directly with windspeed. Since the slope of flight path at touchdown is independent of wind speed, the difference in sink rate is due to the direct variation of ground speed with wind speed for a constant airspeed. The effect is not significant as shown in Fig. 26.
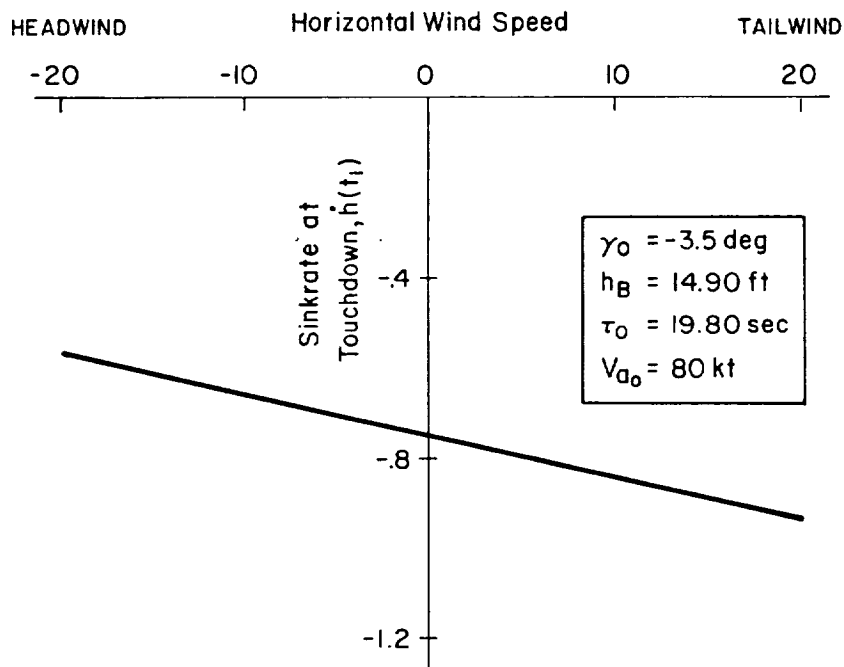
Figure 26. Variation of Touchdown Sink Rate With Wind for the Proposed System

f. Touchdown Time for the Variable τ System

The touchdown time for the variable τ system is computed as shown below.

$$X_1 = X(t_1) \doteq (V_w + Va_o) t_1$$

From Eq. 29

$$t_1 = X_1/(V_w + Va_o)$$

$$= \left(\frac{-\tau_o \, Va_o}{V_w + Va_o}\right) \ln \left(\frac{-h_B}{\tau_o \, Va_o \, \gamma_o}\right) > 0 \tag{32}$$

$$< 0 \qquad\qquad < 0$$

As shown in Eq. 32, touchdown time varies inversely with windspeed such that the airplane lands sooner with the tail wind, as the consequence of the higher groundspeed and a constant X_1. This is in distinction to the present BCS autoflare system where the elapsed time in flare is 47.6 sec independent of wind.

Thus, in summary, the primary effect of the beam follower and the variable τ flare law is to trade the temporal invariance of the existing system for spatial invariance. The value of this tradeoff is that the aircraft will always land at essentially the same point on the runway. As a consequence, the same landmarks may always be used by the ground pilot to monitor correct function of the approach and autoflare systems.

B. LATERAL BEAM TRACKING AND FLARE CONTROL

Lateral control is considerably simpler than longitudinal in that synthetic beam (runway centerline) lateral deviation information can be derived from the radar tracking signal and ground computer and transmitted to the flight control system throughout flare as well as approach. However, the deviation accuracy and signal noise may degrade somewhat as the vehicle nears the runway. Thus, the vehicle can be automatically controlled to the runway centerline until very close to touchdown and therefore minimize lateral drift due to crosswinds.

Past PPRV's (HIMAT, 3/8 scale F-15, etc.) have generally employed skid type landing gear which is designed to be sufficiently sturdy to survive crabbed landings and thus avoid complicating the manual control task just prior to touchdown. There appears to be no reason to alter this landing technique and unnecessarily complicate the flight control mechanization.

Thus, a simple, proven lateral mechanization such as used in the L-1011 (Ref. 9) and Compass Cope RPV (Ref. 10) is proposed. This mechanization, Fig. 27, employs beam error, lateral acceleration, and roll attitude inputs to aileron control. There are no crossfeeds to rudder. The beam error is integrated to minimize effects due to crosswind. Rate of beam error is generated by passing the signal through a washout circuit. The rate signal is summed with lagged lateral acceleration (from a body mounted accelerometer) and roll attitude to produce a complementary filtered damping term. This complementary filter may not be required for the RPRV facility however. It is noted in Ref. 9 that if the ILS beam is fairly clean the complementary filtering is not necessary. Since the "synthetic ILS" beam is computer generated and transmitted to the flight control system at a known sample rate, "beam noise" should be quite narrow band and readily handled.

After flare initiation the beam error gain is reduced to zero as a function of radar altitude (runway referenced) so the roll attitude control loop becomes dominant as the vehicle approaches touchdown. The roll command becomes zero and assures a wings level touchdown so that there will be no danger of a wing strike. As with the longitudinal axis, the vehicle lateral response during flare will be consistent in each landing and therefore reduce the pilot monitoring workload. Of course, lateral drift due to cross winds will build during the wing leveling phase and will be dependant upon specific conditions of each landing.

It appears the only way to assure a wing level touchdown is to feedback bank angle from an airborne vertical gyro. This should be no particular problem since the HIMAT does carry a V.G. as a part of the emergency recovery system (but its output is not used for active control)
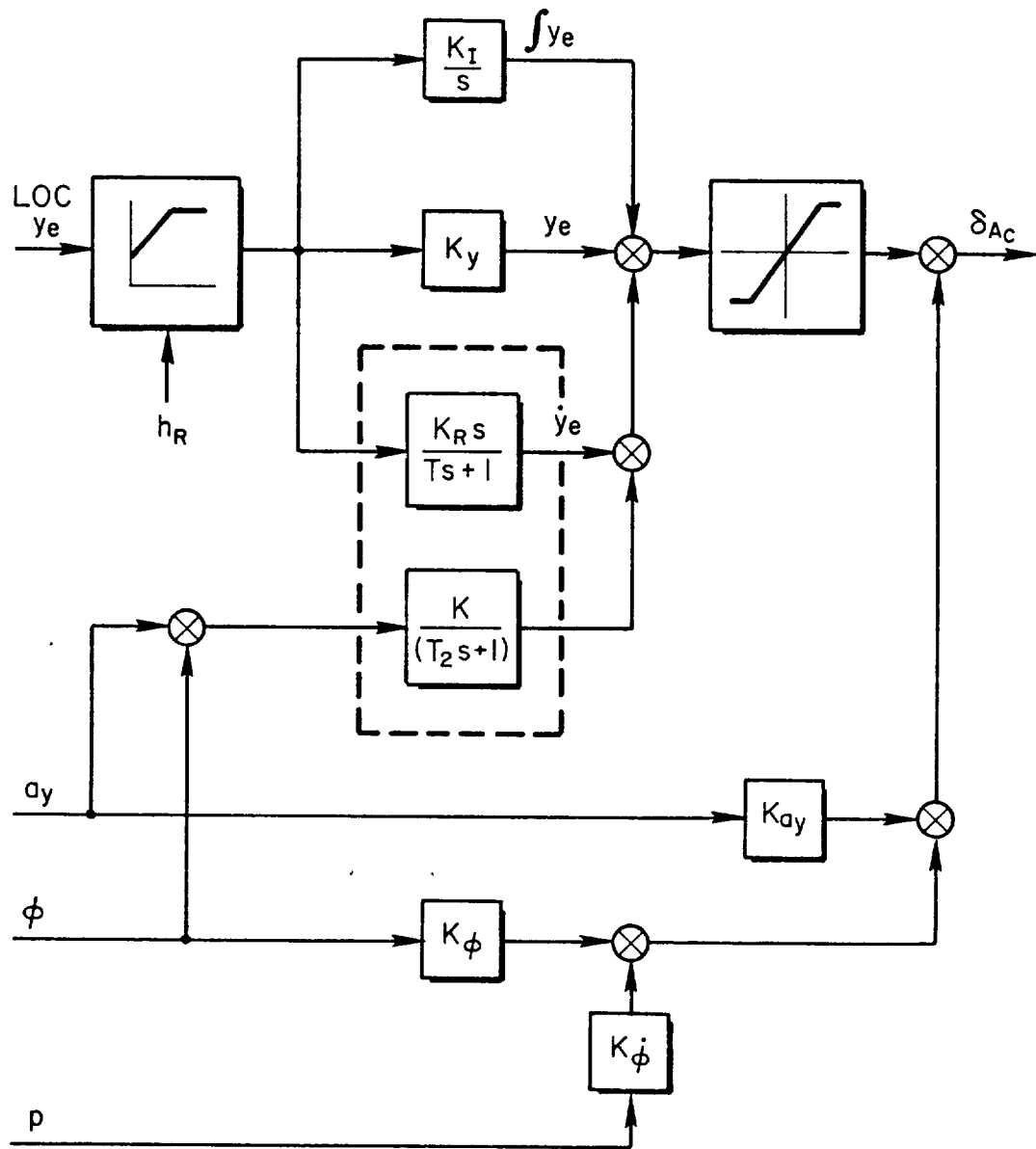
Figure 27. Proposed Lateral Autoland

and the PA-30 apparently employs a V.G. roll output for the manual roll command controller (Fig. 7 and Table 1). Presumably any future RPRV's will have similar needs for attitude signals. It is only necessary that the sensor output be employed in a direct manner in the autoland beam tracking and flare modes.

Integration of the improved lateral autoland control, a manual roll rate command mode, and the present HIMAT backup control system (BCS) is shown in Fig. 28. The manual roll rate command mode is employed to fly the vehicle to localizer beam acquisition. The autoland mode is then engaged to track the beam through flare. In the event of uplink or downlink failure, the system will revert to the present backup control mode with turn commands, r_c, from either the current chase plane control mode or to the autonomous navigation and orbit mode discussed later.

The rudder axis control system can remain the same as in the present autoland system since its function is to provide yaw rate damping and turn coordination.
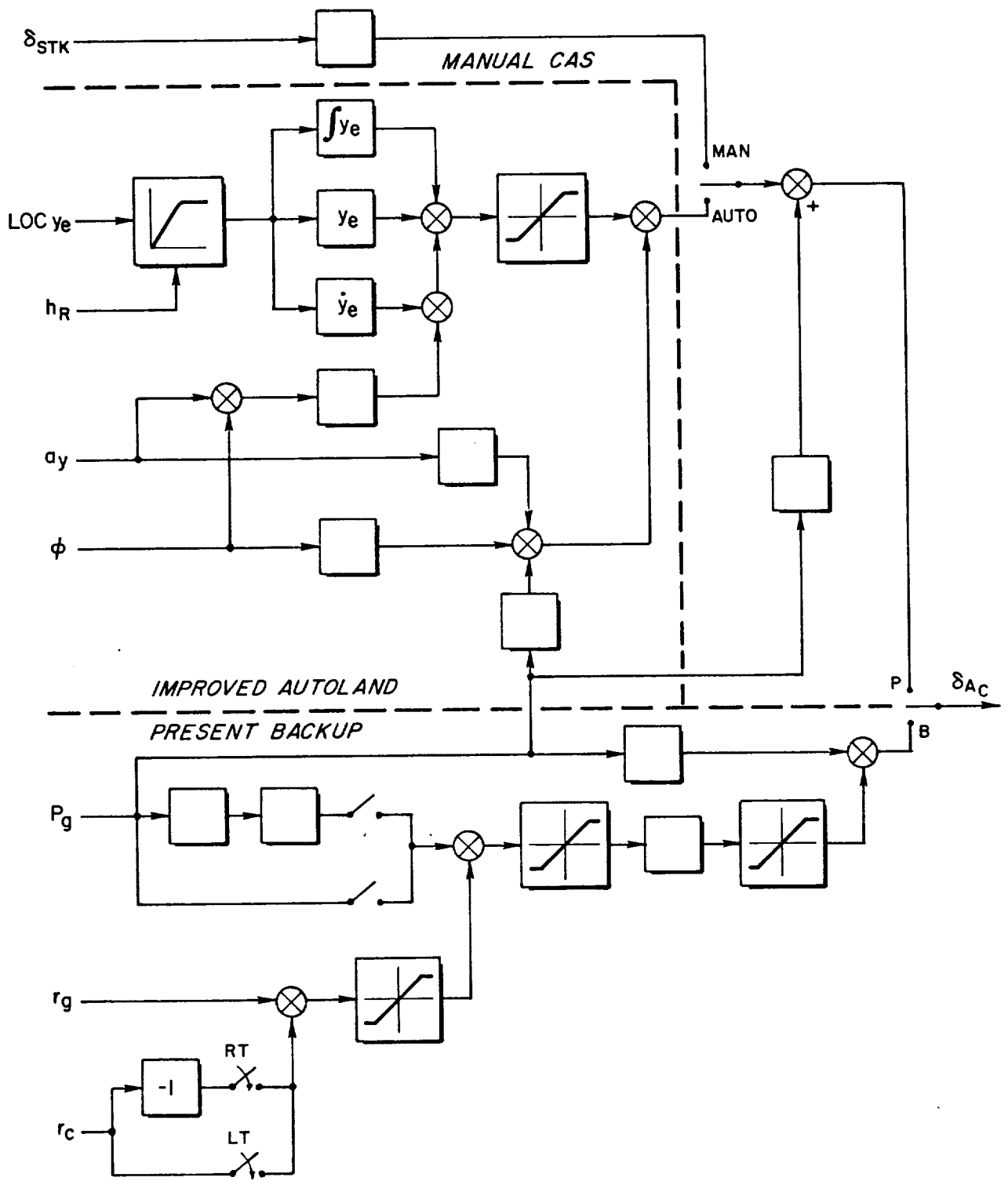
Figure 28. Possible Integration of Automatic and Manual Lateral Control Modes

SECTION IV

PROPOSED HEAD-UP APPROACH AND LANDING DISPLAY

The current (Ref. 4) head-down ADI and head-up T.V. displays and their shortcomings were summarized in Section II. In this section a relatively simple scheme is presented to enhance the head-up T.V. display to alleviate current problems. The specific goals of the improved display are to

- integrate appropriate cockpit panel data onto the T.V. display so that the pilot can fly the complete approach and landing using the head-up display as the primary visual information.

- incorporate status and flight director information to minimize pilot workload in monitoring automatic beam following and landing flare system performance and in accomplishing the task manually.

Means of enhancing T.V. display for the accomplishment of these goals have also been addressed in Refs. 11 and 12. For example, Ref. 11 describes advantages and limitations of several different glide slope type information aids superimposed on the T.V. display from body-fixed versus inertially stabilized camera mountings. The display aids included fixed reticle, glide slope reference lines augmented by rate and acceleeration information. The latter is in effect a beam director display. A piloted simulation involving three different sizes and types of aircraft showed the beam director to result in the least displacement, attitude, and control force variances with either the body-fixed or inertially stabilized camera systems. The director algorithms were of the form

$$\varepsilon_{GS} = h_e + a_1 \dot{h}_e + b_1 a_n$$

$$\varepsilon_{LOC} = y_e + a_2 \dot{y}_e + b_2 a_y$$

where ε_{GS} and ε_{LOC} are the director glide slope and localizer deviations, respectively. As will be shown later, this algorithm does not include all of the feedbacks considered necessary in Ref. 13 for good pilot-centered display but it is compatible with the automatic beam following mechanizations proposed in the previous section and tends to indicate a simple display of the elevator command would probably ease the pilot workload during the approach.

Reference 11 did not address the landing flare maneuver. However, this aspect has been quite adequately covered by the Ref. 12 simulation investigation in which several parameters were superimposed on the T.V. landing view. This investigation even used the PA-30 aircraft as the example vehicle. It was determined that the most consistent flare and touchdown was achieved with a longitudinal dynamic display of radar altitude and altitude rate. The display parameters were ratioed in much the same manner as the two major feedback paths of the automatic flare law previously presented in Fig 21.

The Ref. 12 simulation also investigated the usefullness of glide slope and localizer information during the approach phase and came to much the same conclusions found in Ref. 11. However, Ref. 12 incorporated various flight condition and attitude cues to assess the added benefit (or confusion) aspects. It was found that inclusion of airspeed, altitude, and altitude rate digital readouts were of definite benefit. Recommendations were made for the location of these parameters on the T.V. monitor. A horizon line and a roll attitude indicator were separately assessed. Attitude information is generally considered to be highly beneficial by providing lead on path control and thereby reducing pilot workload while improving performance. It was found in Ref. 12, however, the roll attitude indication was ignored by the pilots. This may have been due to the particular display symbology employed and the visual clutter it introduced. It was determined that inclusion of the horizon line was beneficial.

Based upon the results of Refs. 11 and 12, the approach director display format of Fig. 29 has been selected. In this example the aircraft is below the synthetic glide slope beam (FD_{GS}) and to the left of
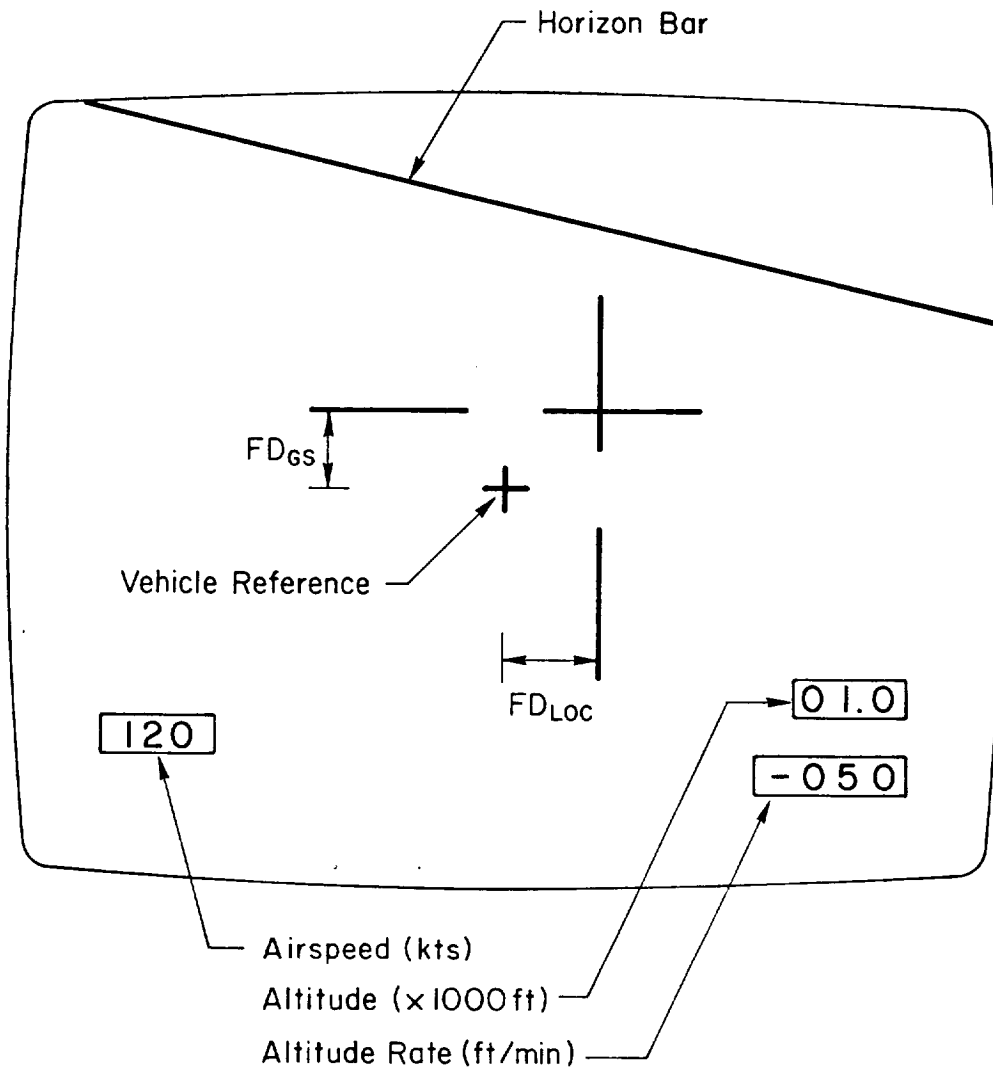
Figure 29. Proposed Landing Approach Display Augmentation

the runway centerline (FD_{LOC}). The horizon bar indicates the aircraft is pitched down and banked left. To prevent the horizon bar from ever leaving the T.V. screen or interfering with the other display parameters, the pitch gain should be very low. The horizon bar thus becomes primarily a display of bank angle. Airspeed, altitude, and altitude rate are located as recommended in Ref. 12. Figure 30 is an example of the approach display augmentation superimposed on the different T.V. views of Fig. 5. These assume the aircraft to be in the same location with respect to the runway in each case but with different bank and heading angles. By flying the vehicle reference cross to the flight director bars the vehicle will follow the synthetic ILS beam to the runway.

The pilot should be alerted to approach to altitude for flare initiation by a flashing symbol. This might be the vehicle reference cross or the altitude numeric. A few feet above flare initiation altitude the display should change to the format indicated in Fig. 31. Here the runway localizer director bar and airspeed numeric continue the same function as in the approach mode. The horizon bar is removed and replaced by a runway reference and the two glide slope bars move independently of one another with the right hand bar indicating radar altimeter altitude from the runway and the left hand bar indicating rate of descent. Bar deflection gains are selected so that the desired exponential flare results in the bars being aligned (horizontally) and simultaneously approaching and reaching the runway bar at vehicle touchdown. The example of Fig. 31 indicates the sink rate to be excessive for the immediate altitude. Log scales are used to increase display sensitivity as the vehicle approaches ground level.

The following subsections address in more detail implementation of flight director beam following and landing flare algorithms and an optical means of superimposing the video and computer generated information.

A. BEAM FOLLOWING MONITOR/DIRECTOR MECHANIZATION

In the automatic beam following mode the ground pilot must monitor for proper error nulling and corrective action for any large deviations
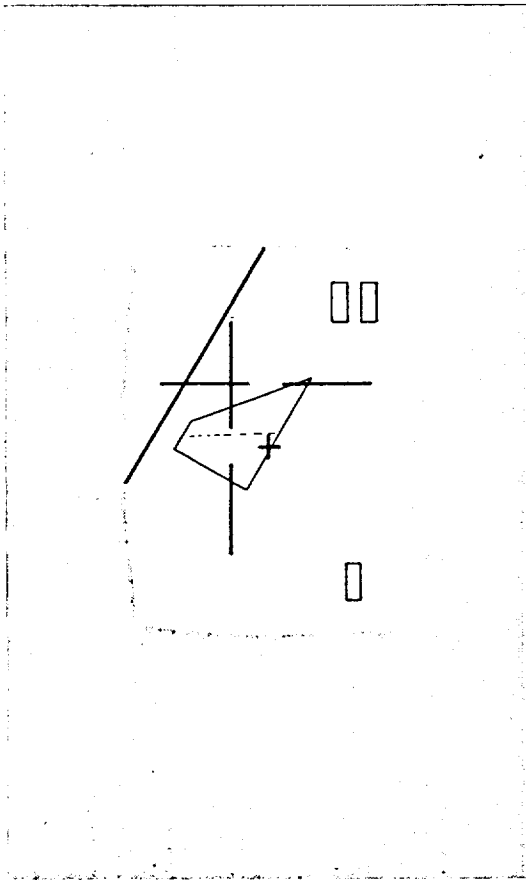
Restricted view of runway, aircraft banked.
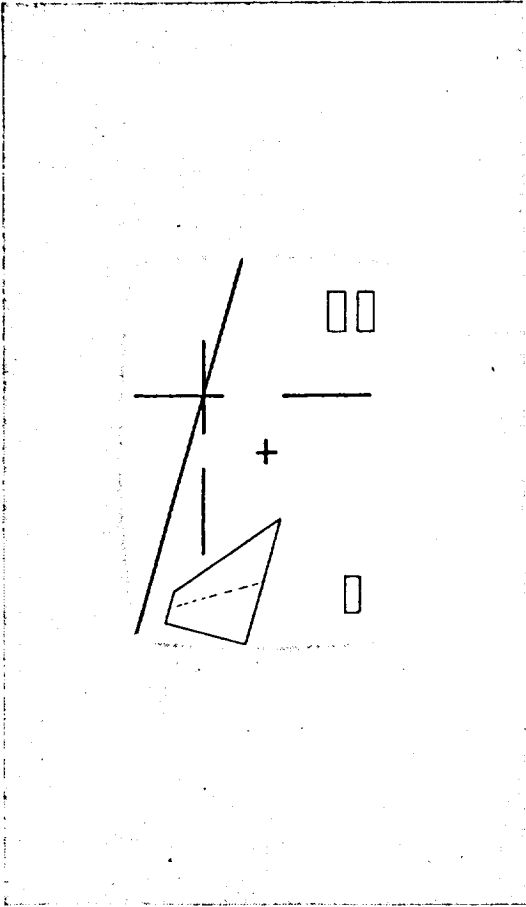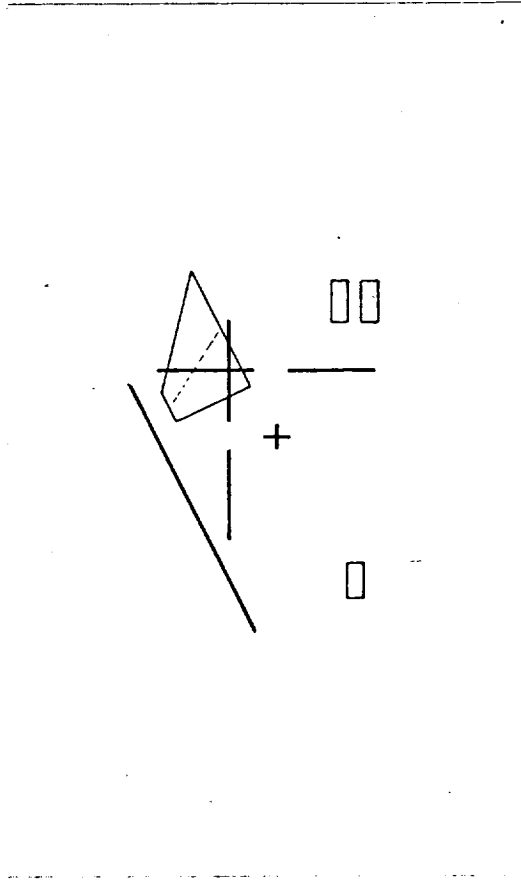
Unrestricted view of runway.

Restricted view of runway, aircraft banked.

Restricted view of runway, aircraft banked.
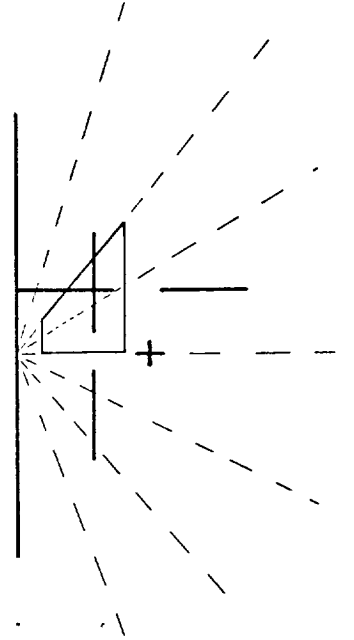
Figure 30. Example of Approach Display Augmentation Superimposed on Different T.V. Views of Runway
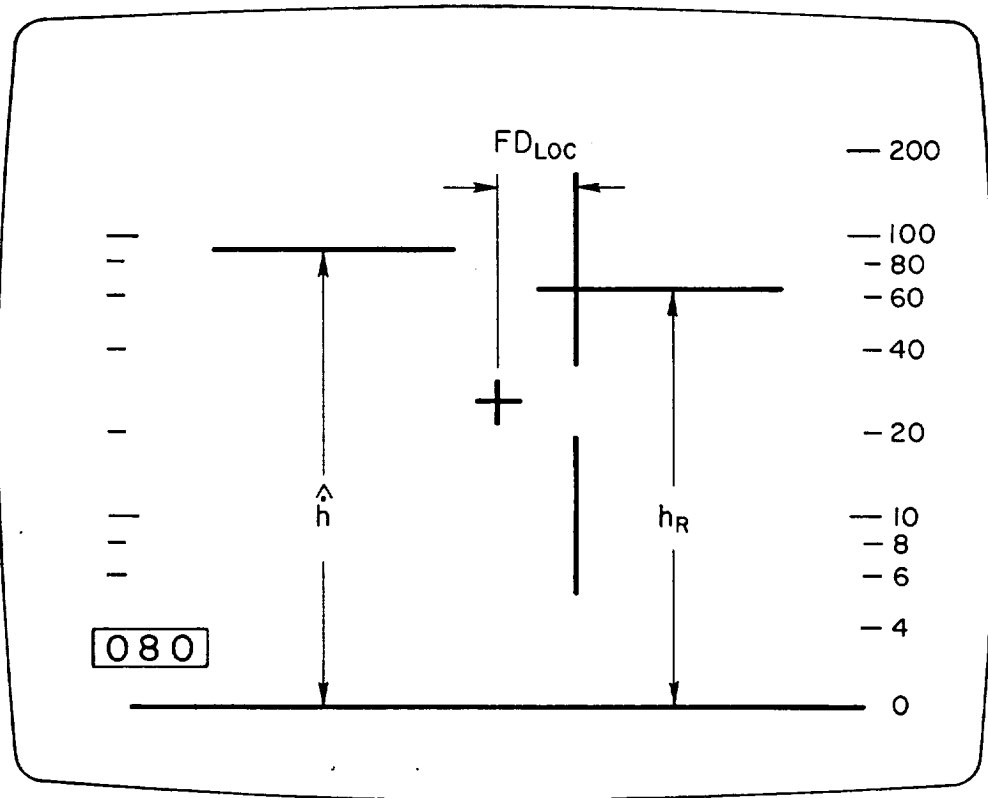
Figure 31. Proposed Landing Flare Display Augmentation

due to external disturbances. This function can be served by display-
ing, for example, an indicator deflection proportional to beam error
alone. However, in the manual mode the display must take into account
various pilot-centered director requirements including

- ability of pilot to distinguish between responses
  due to external disturbances and his corrective
  inputs.

- elimination of any integral of beam error feed-
  back so the display does not ramp off to its
  limits during any periods of unattended opera-
  tion.

- provision of effective controlled element dynam-
  ics which approximate K/s in the bandwidth region
  over which the pilot is attempting control.

The first two of these requirements define a display algorithm dif-
ferent from that employed by the automatic beam follower mode previously
presented. To avoid any unnecessary and confusing transients when
switching from auto to manual, or vice versa, it is desireable that one
display concept be used for both modes. Thus, the manual mode should
prevail.

The basic considerations for selection of longitudinal flight direc-
tor system feedbacks are summarized in Table 3 from Ref. 13. It should
be noted that the key beam feedbacks are beam deviation and deviation
rate (in our case h_{GSE} and $\dot{h}_{GSE}$). Beam error integration is not desired
as noted previously. Washed out pitch attitude is desired to provide
short term feedback of vehicle response to pilot inputs and therefore
prevent any tendency to over control. These three feedbacks provide
precise beam following capability. Including pitch rate allows indepen-
dent control of the short period damping ratio.

A resulting beam-derivative plus pitch attitude system is shown in
generic form in Fig. 32 where G_h^{FD} and G_θ^{FD} are the respective feedback
functions.

A central consideration of the pilot-centered requirements is that
the feedback gains and equalizations be selected so that the net

TABLE 3. CONSIDERATIONS FOR SELECTION OF LONGITUDINAL SYSTEM FEEDBACKS

FEEDBACKS	GUIDANCE AND CONTROL REQUIREMENTS		PILOT CENTERED REQUIREMENTS	
	PRIMARY REQUIREMENT	COMMENTS	PRIMARY REQUIREMENT	COMMENTS
Pitch Attitude, $\theta \rightarrow FD_c$	Short period attitude regulation	Must be washed out to avoid standoff between θ and d	Command bar consistency	Mid-frequency flight director motions should look like pitch attitude
Pitch Attitude Rate, $\dot{\theta} \rightarrow FD_c$	Short period damping	Need to lag at high frequency to avoid a busy display	Minimum pilot compensation. Remnant suppresion.	Provided K/s-like response at frequencies beyond the phugoid
Beam Rate, $\dot{d} \rightarrow FD_c$	Vertical path damping	Beam noise is critical -- may require complementary filter with a_z	Minimum pilot compensation. Path mode consistency. Remnant suppression.	Provides K/s-like effective controlled element
Beam Deviation, $d \rightarrow FD_c$	Vertical path following	Must be range compensated to avoid stability problems and still achieve required accuracy	Path mode consistency	Low frequency flight director should look like beam deviation
Beam Integration $\int d\ dt \rightarrow FD_c$	Path angle trimming	Long time constant required for stability reduces regulation effectiveness	Path mode consistency	Results in inconsistencies between command and beam errors after periods of unattended operation
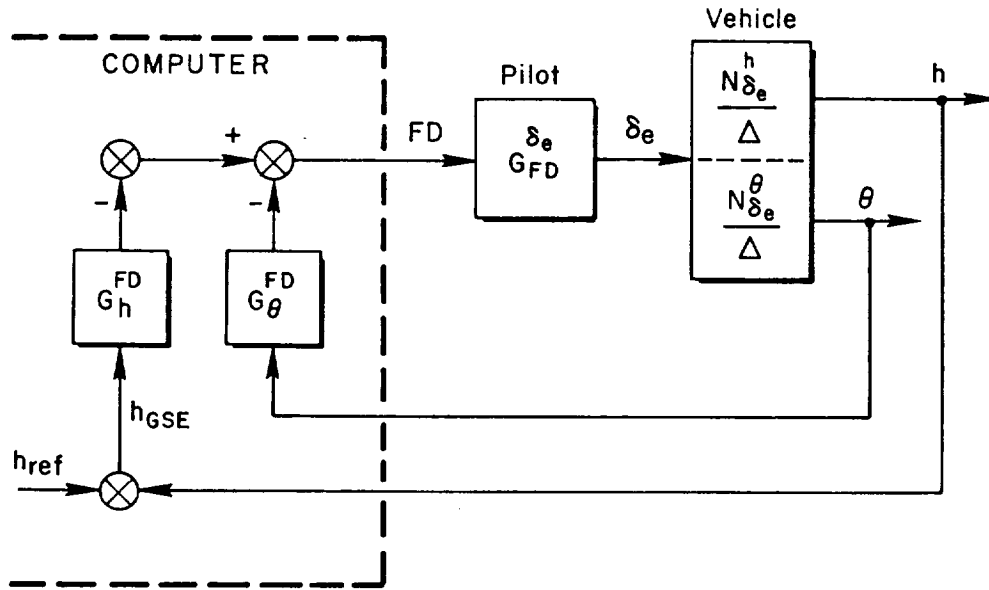
Figure 32. Simplified Director/Vehicle Block Diagram

transfer characteristics from elevator, δ_e, to director instrument displacement, FD, look approximately like an integration, K/s. As shown in Ref. 13, the analytical procedure for assessing and establishing this result is to add the component vehicle transfer function with their associated equalization. The effective flight director transfer function is then,

$$\frac{FD}{\delta_e} = \frac{G_\theta^{FD} N_{\delta_e}^\theta + G_h^{FD} N_{\delta_e}^h}{\Delta}$$

where $N_{\delta_e}^\theta$ and $N_{\delta_e}^h$ are the vehicle pitch and altitude response numerators, respectively. In keeping with the feedbacks of Table 3, the feedback transfer characteristics are:

$$G_\theta^{FD} = \frac{K_\theta s}{\left[s + \left(1/T_{wo}\right)\right]} + K_{\dot\theta} s = \frac{K_{\dot\theta} s \left[s + \left(1/T_{wo} + K_\theta/K_{\dot\theta}\right)\right]}{\left(s + \left(1/T_{wo}\right)\right)}$$

$$G_h^{FD} = K_h + K_{\dot h} s = K_{\dot h} \left(s + \left(K_h/K_{\dot h}\right)\right)$$

Figure 33 is a Bode-Siggie amplitude sketch of the director transfer function numerator, $G_\theta^{FD} N_{\delta_e}^\theta + G_h^{FD} N_{\delta_e}^h$, particularized for the PA-30 dynamic and the Ref. 13 recommended equalization values (see Table 4). The numerator roots are determined by the intersection of the gain closure line and the various σ and jw amplitude loci in Fig. 33. Selecting a value of +0.035 rad/ft for the gain K_h^*/K_θ^* produces effective flight director zeros identified by the symbols (█) and results in the flight director numerator $N_{\delta_e}^{FD}$ shown.

A sketch of the open-loop director/vehicle, $N_{\delta_e}^{FD}/\Delta$, Bode asymptote and phase is given in Fig. 34. The selected director equalization and gains are seen to result in the desired K/s-like amplitude ratio over a large frequency region where the pilot might be expected to close the loop (potential crossover region). The phase sketch for this linear analysis indicates there is no instability problem regardless of how high a crossover the pilot might try to achieve. Actually, however, the effective time lags (τ) due to the up/down link communication can be expected to produce a phase curve such as the dashed line in Fig. 34. This still allows a bandwidth of 2 rad/sec without any pilot generated lead and somewhat greater than 2 rad/sec if pilot lead is employed.

It should be emphasized that the parameters of this example longitudinal flight director law are particularized to the PA-30 dynamic characterized. For such a director to work properly with any other vehicle, the feedback gains, time constants, etc., must be rescheduled to match that vehicle. This is not difficult in that it merely requires repeating the foregoing analysis to select the gains and equalization. These are then set into the display algorithm in the ground computer for each vehicle.

The lateral flight director algorithm is of the same form as the longitudinal except that the feedbacks are localizer y_e and $\dot{y}_e$, washed out roll attitude and roll rate. These feedbacks are all consistent with the autoland mechanization of Fig. 27, however, the appropriate gains, time constants, etc., must be tailored to each vehicle using the same analytic approach discussed above.
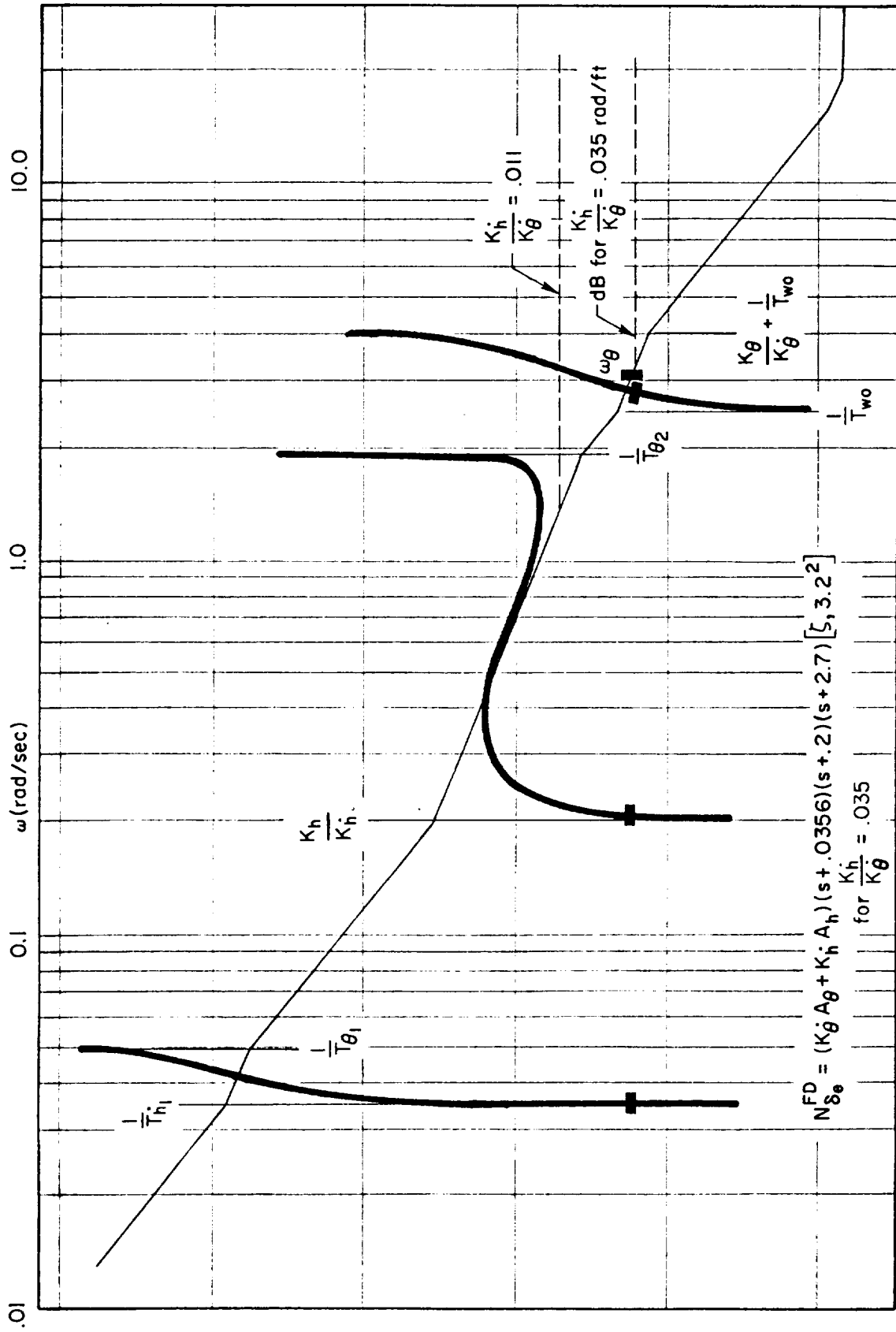
Figure 33. Bode-Siggie Amplitude Sketch of the Director Transfer Function Numerator

TABLE 4. SELECTED EQUALIZATION VALUES

EQUALIZATION	EXPRESSION	DESIRED LOCATION AND VEHICLE VALUE (rad/sec)	SELECTED EQUALIZATION	REMARKS
Pitch Washout	$\dfrac{1}{T_{wo}}$	$< \omega_{sp} = 3.51$ $> \dfrac{1}{T_{\theta_2}} = 1.93$	2.5	Washout less than ω_{sp} to provide attitude stability but greater than $1/T_{\theta_2}$ for wind-proofing and to maintain altitude bandwidth.
Pitch Attitude	$\dfrac{1}{T_{wo}} + \dfrac{K_\theta}{K_{\dot\theta}}$	$> \omega_{sp} = 3.51$	4.0	Pitch attitude lead set to improve short period damping and extend the region of K/s by having the resulting ω_θ zeros cancel the ω_{sp} poles
Altitude	$\dfrac{K_h}{K_{\dot h}}$	$\dot{=} \omega_p = 0.16$	0.2	Greater than ω_p to avoid a "busy" display and the low frequency closed-loop d/d_c amplitude droop, yet maintain mid-frequency phase margin
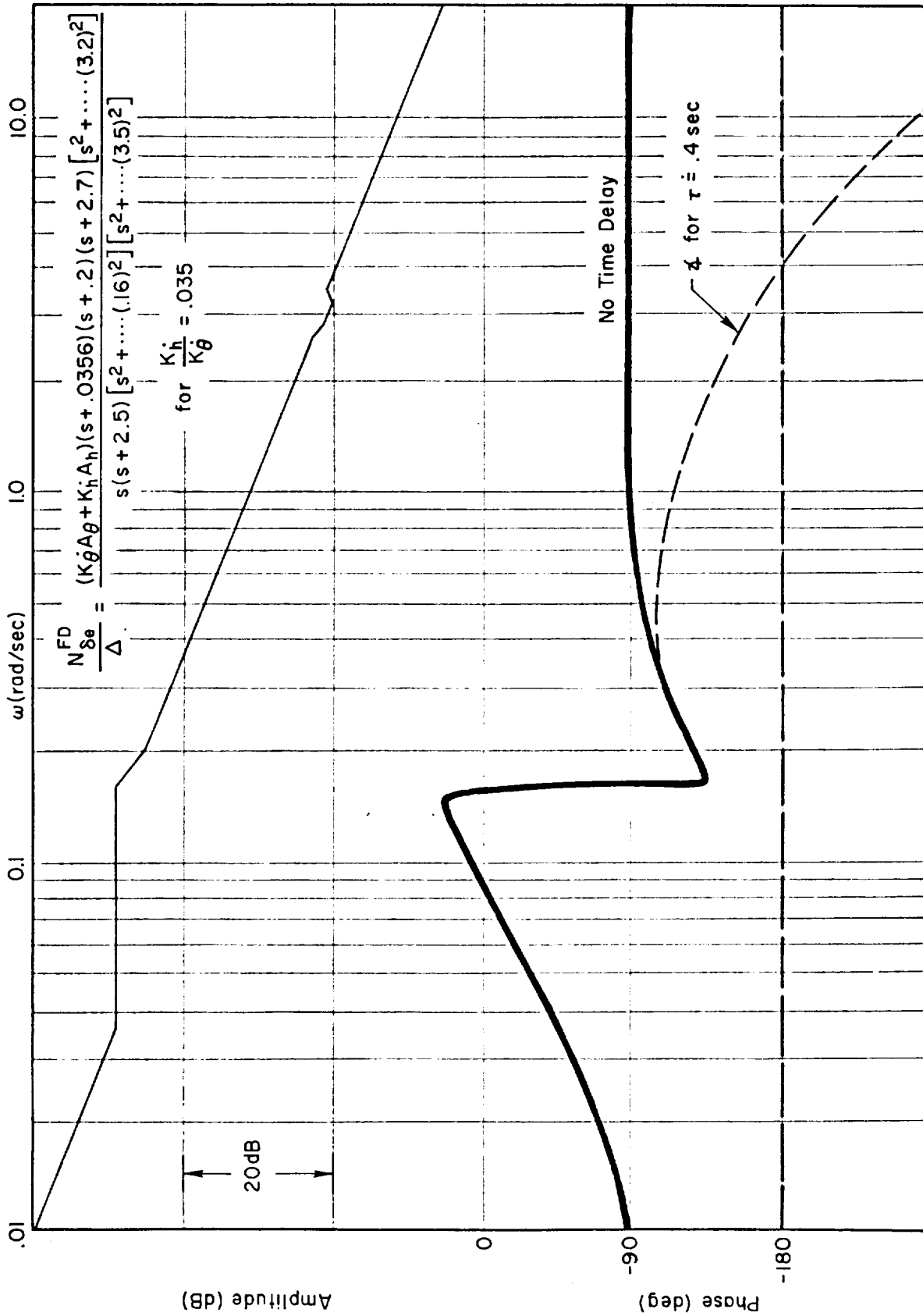
Figure 34. Open Loop Director/Vehicle Amplitude Asymptote and Phase Plot For PA-30 Aircraft Dynamics

B. LANDING FLARE MONITOR/DIRECTOR MECHANIZATION

The landing flare is basically a terminal control problem to maintain the proper relationship between h and $\dot{h}$ to touchdown. Therefore, for monitoring the longitudinal autoflare system (Fig. 21) the two components of the elevator command, i.e., $K_{h_R}V_G h_R$ and $\dot{h}$, are displayed as in Fig. 31. This provides lead information to the pilot in that he can independently discern sink rate and altitude above the runway. If the two signals simultaneously approach zero the autoflare is functioning properly. If sink rate should become excessive for any reason, the pilot can immediately detect it, take over manual control, and correct the situation.

For manual flare control, there again should be no change in the display format from that employed in the automatic mode. Fortunately, there is no problem in that the same h_R and $\dot{h}$ parameters are consistent with the manual display recommended from the Ref. 12 simulation. Thus upon reaching the flare initiation altitude the longitudinal monitor/director display signals are obtained from the Fig. 20 autoland block diagram. This is shown in simplified form in Fig. 35.
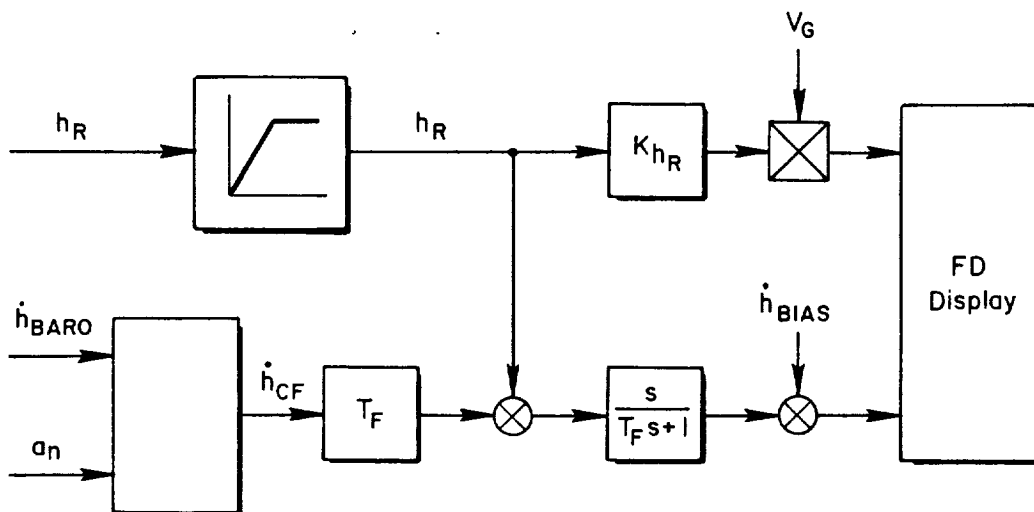
Figure 35. Landing Flare Monitor/Director Mechanization

The lateral axis control task during flare is to maintain the air-craft flight path along the runway centerline. This is accomplished by continuing tracking to the synthetic ILS beam all the way to touchdown (or to the lowest altitude for which the "beam" can be adequately gener-ated). Thus, the lateral beam tracking function remains the same for flare as for approach and monitor/director mechanization is unchanged.

C. DISPLAY IMPLEMENTATION

There are several possible means of combining the monitor/director displays with the present T.V. monitor. One is to electronically super-impose the two signals directly into the monitor screen. A second, less expensive approach is to optically superimpose the T.V. scene and a CRT generated display via a combining glass. This latter has been employed very successfully in several simulators fabricated at STI. This approach does require a reduced light level in the room containing the simulator. It is understood that the ground pilot station is presently operated in semi-dark conditions for better T.V. viewing and to minimize distractions in the pilots' peripheral view. Thus, the combining glass approach is recommended.

A possible layout is sketched in Fig. 36. This requires only the addition of a CRT and combining glass to the present ground station.
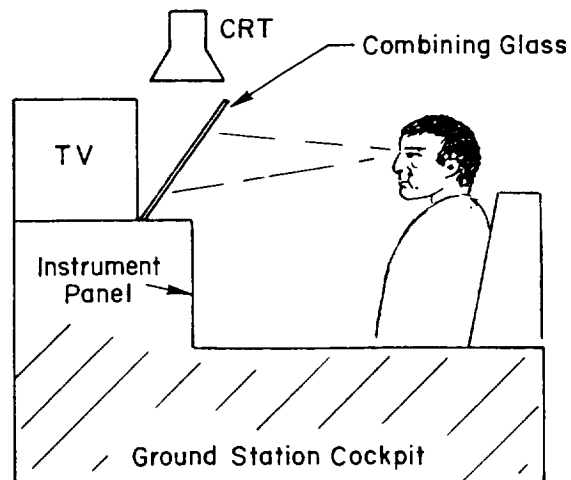
Figure 36. Proposed Means of Superimposing Flight
Director Symbology on the T.V. View

The combining glass is set at a 45 deg angle in front of the T.V. monitor. The display symbology of Figs. 29 and 31 is generated on the CRT and projected onto the combining glass. The pilot then sees the two views superimposed. This approach offers a distinct advantage in that the CRT display brightness can be independently controlled to optimize contrast between the real world T.V. scene and the director symbology.

SECTION V

AUTONOMOUS ORBITING ALGORITHMS FOR RPV'S

A. INTRODUCTION

This working paper documents the derivation of simple, orbit-about-a-fixed-point algorithms for autonomous navigation of a remotely piloted vehicle (RPV). This can form a preliminary basis for one of the on-board navigation software modules.

The basic problem is one of providing a "safe orbit" capability in the event of loss of ground-to-air communications links. The autonomous mission phases or "modes" consist of: detecting uplink loss and determining current vehicle and wind states; proceeding to the safe orbit area; initiating and maintaining an orbit about a fixed ground point; and after a predetermined number of orbits, exiting the orbit mode and proceeding toward a possible autonomous landing. Of course, any of the autonomous modes could be interrupted in the event of uplink recovery, and should allow for return to manual control. This working paper discusses the orbit maintenance mode only.

The constraints assumed are that:

- The vehicle is subjected to winds aloft, which without correction would cause drift out of the safe orbit area, during the 5 to 15 minute orbit mode period.

- The only information available to the vehicle is its position and an estimate of the wind vector at uplink loss, and continuous signals for airspeed and Euler heading angle (from onboard gyros or integrated rate gyros).

- The module output is roll angle command (of course this is kinematically similar to a yaw or heading rate command). For simplicity -- and in view of the "emergency" nature of the mission -- speed control via autothrottle is not considered, and airspeed and altitude, for the moment, are assumed constant.

For this preliminary analysis, sensor noise and drift, and changes in the wind vector are assumed to be zero. The vehicle model is kinematic (with no sideslip or dynamics). Further analyses should look at the effects of these variables on orbiting accuracy.

The remainder of this paper describes two algorithms. The first is for a circular path; the second, improved one is for dead reckoned wing pointing, which results in superelliptical orbits. Both are given in analytical terms, unembellished. Some trajectory plots are given, resulting from digital simulation. The appendices give time histories.

B. CIRCULAR ORBIT ALGORITHM

1. Problem: Fly Circular Path Over Ground, Under Steady Wind

Assume:

- Constant airspeed magnitude, $|\bar{V}_a|$

- Zero sideslip, no vehicle dynamics

- Heading angle, ψ, available

- Orbit begins at $t=0^+$

- Initial flight path is tangent to desired circle

- Constant (inertial) wind vector $(\bar{V}_w)$

Now, referring to Fig. 37, the ground speed is,

$$\bar{V}_g = \bar{V}_a + \bar{V}_w$$

$$\bar{V}_a = U \cos \psi \, \bar{I} + U \sin \psi \, \bar{j}$$

$$\bar{V}_w = V_w \bar{I}$$

$$\bar{V}_g = (U \cos \psi + V_w)\bar{I} + U \sin \psi \, \bar{j}$$
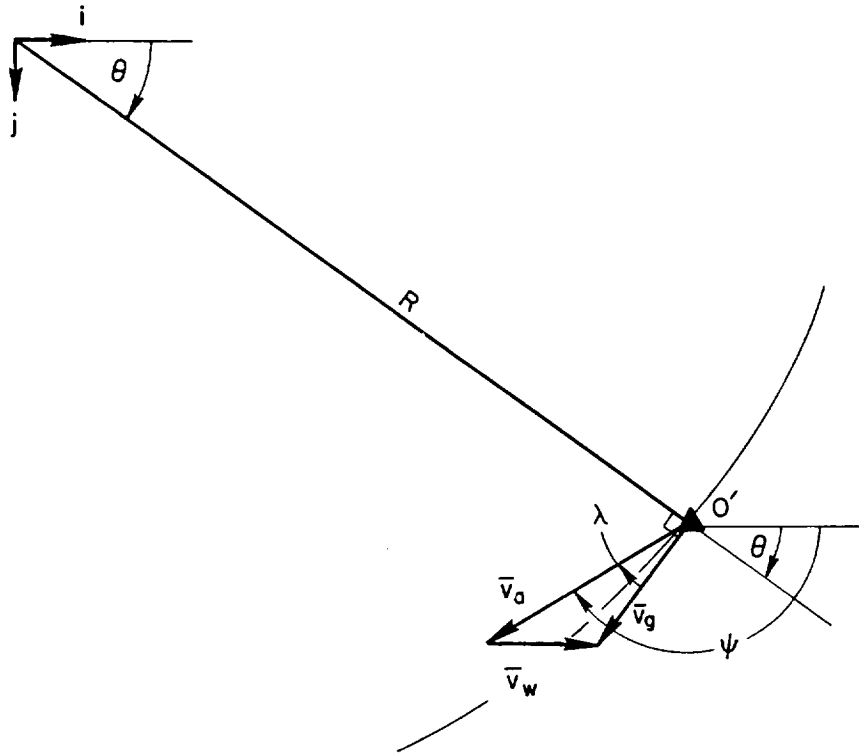
Figure 37. Circular Path Geometry

Then,

$$\lambda = \cos^{-1}\left(\frac{\bar{V}_a}{||\bar{V}_a||} \cdot \frac{\bar{V}_g}{||\bar{V}_g||}\right)$$

$$\lambda =$$

$$\cos^{-1} \frac{\begin{Bmatrix} U \cos \psi + V_w \\ U \sin \psi \end{Bmatrix} \times \begin{Bmatrix} U \cos \psi \\ U \sin \psi \end{Bmatrix}}{\sqrt{U^2 \cos^2 \psi + 2UV \cos \psi + V^2 + U^2 \sin^2 \psi} \times \sqrt{U^2 \cos^2 \psi + U^2 \sin^2 \psi}}$$

$$= \cos^{-1} \frac{\left(U^2 \cos^2 \psi + UV \cos \psi + U^2 \sin^2 \psi\right)}{U\sqrt{U^2 + 2\,U\,V \cos \psi + V^2}}$$

$$\lambda = \cos^{-1} \frac{(U + V \cos \psi)}{\sqrt{U^2 + 2UV \cos \psi + V^2}} \quad , \quad \text{the (estimated flight path angle}$$

The circular arc angle θ is,

$$\psi = \theta + \frac{\pi}{2} + \lambda$$

$$\theta = \psi - \frac{\pi}{2} - \lambda$$

Now, we need to compute a command flight path angle, $\lambda_c(\theta, V, U)$, which will result in a circular (inertial) trajectory. Consider Fig. 38. Let the current position, O', be the origin of an inertial coordinate system. The problem is then to find x, y corresponding to the intersection of $\bar{V}_a$ and $\bar{V}_w$ loci, referenced to the known flight path tangent through the current position.*

The wind vector anchor point locus is

$$x = -y \tan \theta - V$$

and the aircraft velocity locus is,

$$x^2 = U^2 - y^2$$

Combining:

$$x^2 = y^2 \tan^2 \theta + 2 \, Vy \tan \theta + V^2 = U^2 - y^2$$

$$\sec^2 \theta \, y + 2V \tan \theta \, y - \left(U^2 - V^2\right) = 0$$

and the solution to this is:

$$y_c = \frac{2V \tan \theta \pm \sqrt{4 \, V^2 \tan^2 \theta + 4 \sec^2 \theta \left(U^2 - V^2\right)}}{2 \sec^2 \theta}$$

$$= \frac{V \tan \theta + \sqrt{U^2 \sec^2 \theta - V^2}}{\sec^2 \theta}$$

---

*Note: In general, there will be two solutions (clockwise and counterclockwise); therefore, suitable logic must be employed later.
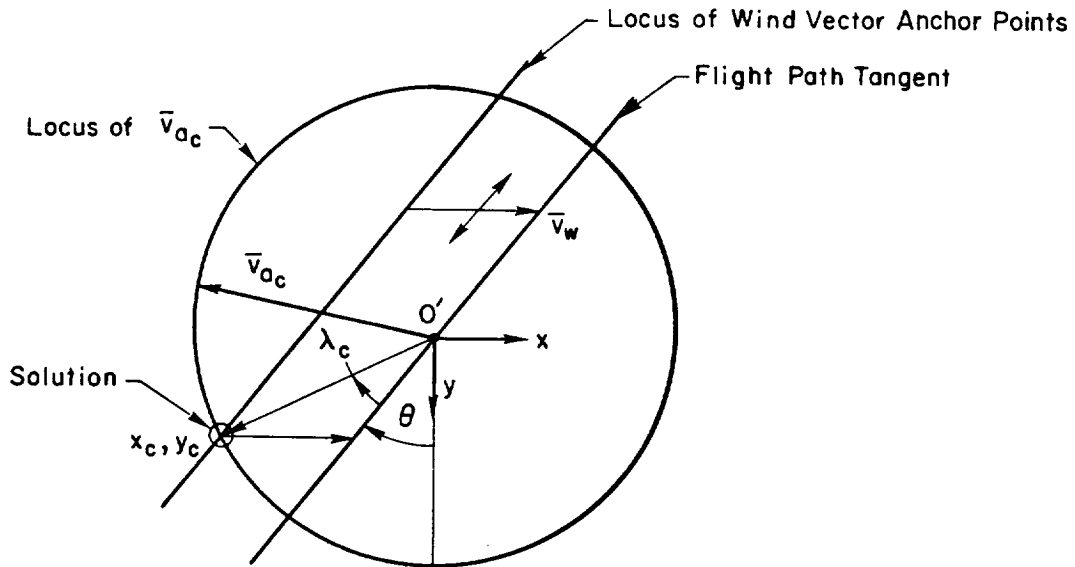
Figure 38. Command Flight Path Angle
for Circular Path

$$y_c = \cos \theta \left(V \sin \theta \pm \sqrt{U^2 - V^2 \cos^2 \theta}\right)$$

and

$$x_c = -y \tan \theta - V$$

By pointing the aircraft (located at O') toward x_c, y_c, the resultant velocity will be along the tangent, exactly.

The command flight path angle corresponding to this is

$$\lambda_c = \cos^{-1} \frac{\bar{V}_a}{||\bar{V}_a||} \times \bar{t}$$

where $\bar{t}$ is the unit tangent:

$$\bar{t} = -\sin \theta \, \bar{I} + \cos \theta \, \bar{j} \quad \text{(for clockwise flight)}.$$

Therefore,

$$\lambda_c = \cos^{-1} \frac{(- x_c \sin \theta + y_c \cos \theta)}{\sqrt{x_c^2 + y_c^2}}$$

We need to compute the command roll angle which corresponds to this path angle. To do this, first consider the ground speed along the circular arc and, knowing this, we can compute the bank angle required for circular motion at radius R.

$$\bar{V}_{g_c} = \bar{V}_{a_c} + \bar{V}_w$$

$$= \left[- U \sin (\theta + \lambda_c) + V_w \right] \bar{I}$$

$$+ U \cos (\theta + \lambda_c) \bar{J}$$

Therefore,

$$||\bar{V}_{g_c}|| = U_{g_c}$$

$$= \sqrt{U^2 \sin^2 (\theta + \lambda_c) - 2 U V \sin (\theta + \lambda_c) + V^2 + U^2 \cos^2 (\theta + \lambda)}$$

$$U_{g_c} = \sqrt{U^2 - 2 U V \sin (\theta + \lambda_c) + V^2}$$

Now, consider Fig. 39. To generate the required acceleration $(= U_{g_c}^2 / R)$ directed toward the center of the circle, both longitudinal and lateral components must be generated, where

$$a_x' = \frac{U_{g_c}^2}{R} \sin \lambda_c$$
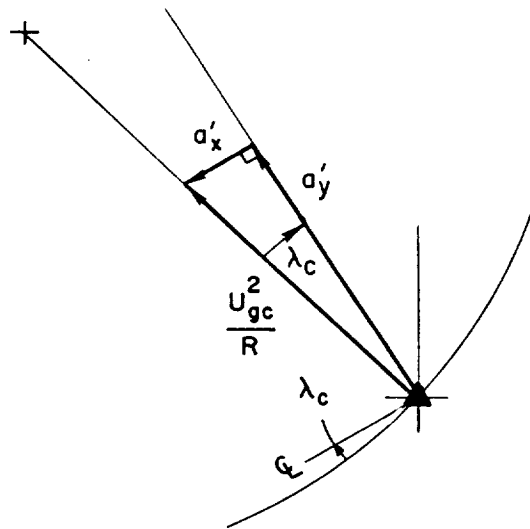
Figure 39. Resultant Acceleration Vectors

$$a_y' = \frac{U_{gc}^2}{R} \cos \lambda_c$$

The means for generating accelerations in the aircraft axes are engine thrust and coordinated roll-yaw. Therefore

$$T_c = ma_x' = m \frac{U_{gc}^2}{R} \sin \lambda_c$$

$$\phi_c = \tan^{-1} \frac{U_{gc}^2}{gR} \cos \lambda_c$$

If _only_ roll commands are used, the situation is more difficult. In general, since the centripetal acceleration vector is skewed to the radius during crosswind flight, the center of curvature will translate relative to the desired center. The translation direction will be _crosswind_ ($\bar{W} \times \bar{V}_w$ direction), with a magnitude bounded by ($2R \sin \lambda_c$) per orbit (this is considerably less than if no wind correction was used).

To compensate for this, we could modulate the roll command on the up- and down-wind portions to give more or less lateral acceleration than originally, so the net center translation would be zero. This probably would give an elliptical, fixed orbit.

To do this we would need to find a $\phi_c = \phi_c + \phi'_c$ such that

$$\int_0^{2\pi} \phi'_c \, d\theta = \frac{1}{gR} \tan^{-1} \int_0^{2\pi} U_{g_c} \sin \lambda_c \cos \lambda_c \, d\theta$$

subject to the appropriate boundary conditions. This is an inconvenient task at best and a good guess might be:

$$\phi'_c(\theta) = -\frac{1}{gR} \tan^{-1} \frac{U_{g_c}^2}{R} \sin \lambda_c \cos \lambda_c \sin \theta$$

(Approximate, for roll control only)

This gives no change in acceleration at the crosswind positions ($\theta = 0$, π); an acceleration decrement at upwind $(\theta = \pi/2)$, and increment at downwind $(\theta = 3\pi/2)$, of the proper magnitude.

3. Vehicle Motion

A simplified set of fixed airspeed kinematic equations can be used to compute the resulting trajectory (for preliminary validation), i.e.,

$$\dot{x} = U \cos \psi + V_w$$

$$\dot{y} = U \sin \psi$$

$$\dot{\psi} = \frac{g}{U} \tan \phi_c$$

4. Results

Figures E-1 to E-5 of Appendix E show resulting orbiting time histories for the circular algorithm. These give x, y inertial positions (X1, X2) and heading angle (X3) as a function of time, for various vehicle airspeeds for a fixed 100 ft/sec wind velocity. As can be seen, when airspeed is high relative to wind speed, the time history is stable. As airspeed becomes closer to wind speed, the x and y peaks begin to drift away, linearly with time. Also, sharper "cusps" appear in the y trace, corresponding to higher turn rates on the downwind legs. When the wind speed is half the airspeed, the algorithm diverges, and orbit is not achievable.

These results are summarized in Fig. 40. This shows the xy trajectory as a function of wind-to-airspeed ratio. When the wind is less than 0.25 of the airspeed, the drift during the first orbit is quite small. Above this ratio the trajectory becomes increasingly elliptical and eventually diverges. The progression in drift rate suggests an exponential divergence with wind to airspeed ratio.
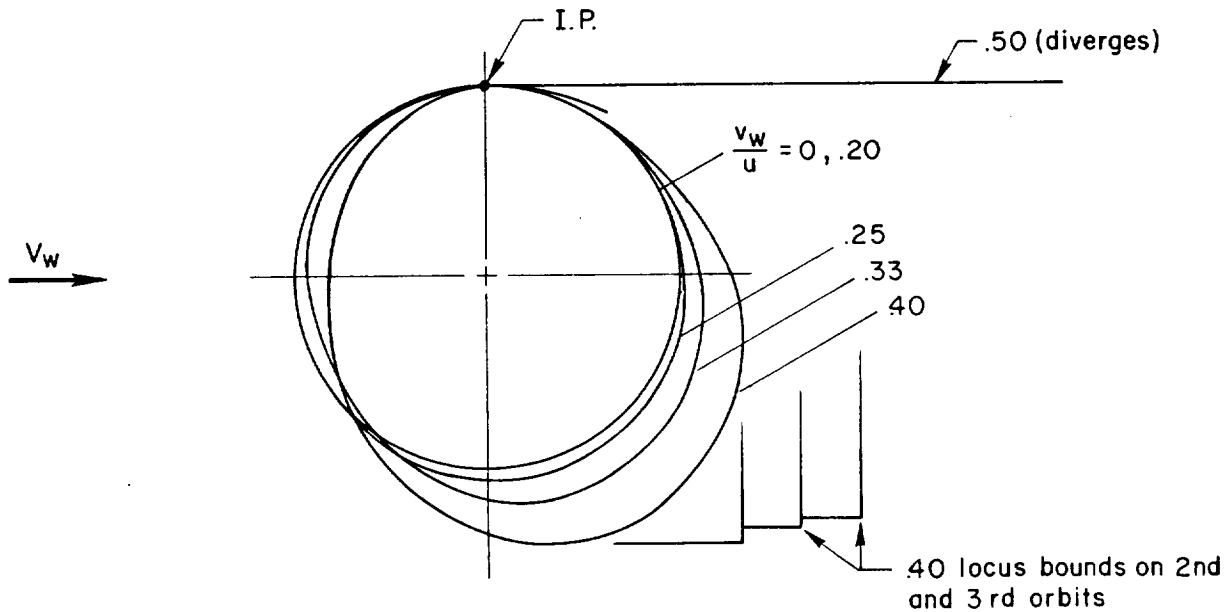
Figure 40. First Orbit Trajectories for Circular Algorithm, as a Function of Wind to Airspeed Ratio

This is confirmed in Fig. 41 which shows the orbit drift velocity as a function of wind speed (both normalized by airspeed). In a realistic worst case situation where the wind aloft was 0.40 of the airspeed, the drift velocity would be one order of magnitude less than the wind speed. For a 15 minute flight of a low speed aircraft (V_a = 200 ft/sec), this could still give nearly a 1-1/2 mile drift (on an extremely windy day). On a more typical day (V_w = 30 ft/sec) with an approach configured HiMAT-like vehicle (V_a = 300 ft/sec), the total drift would be less than 50 ft! So this algorithm appears extremely sensitive to relative wind and air speed.

The divergence of this circular algorithm is of course a consequence of the residual acceleration during portions of the orbit. As
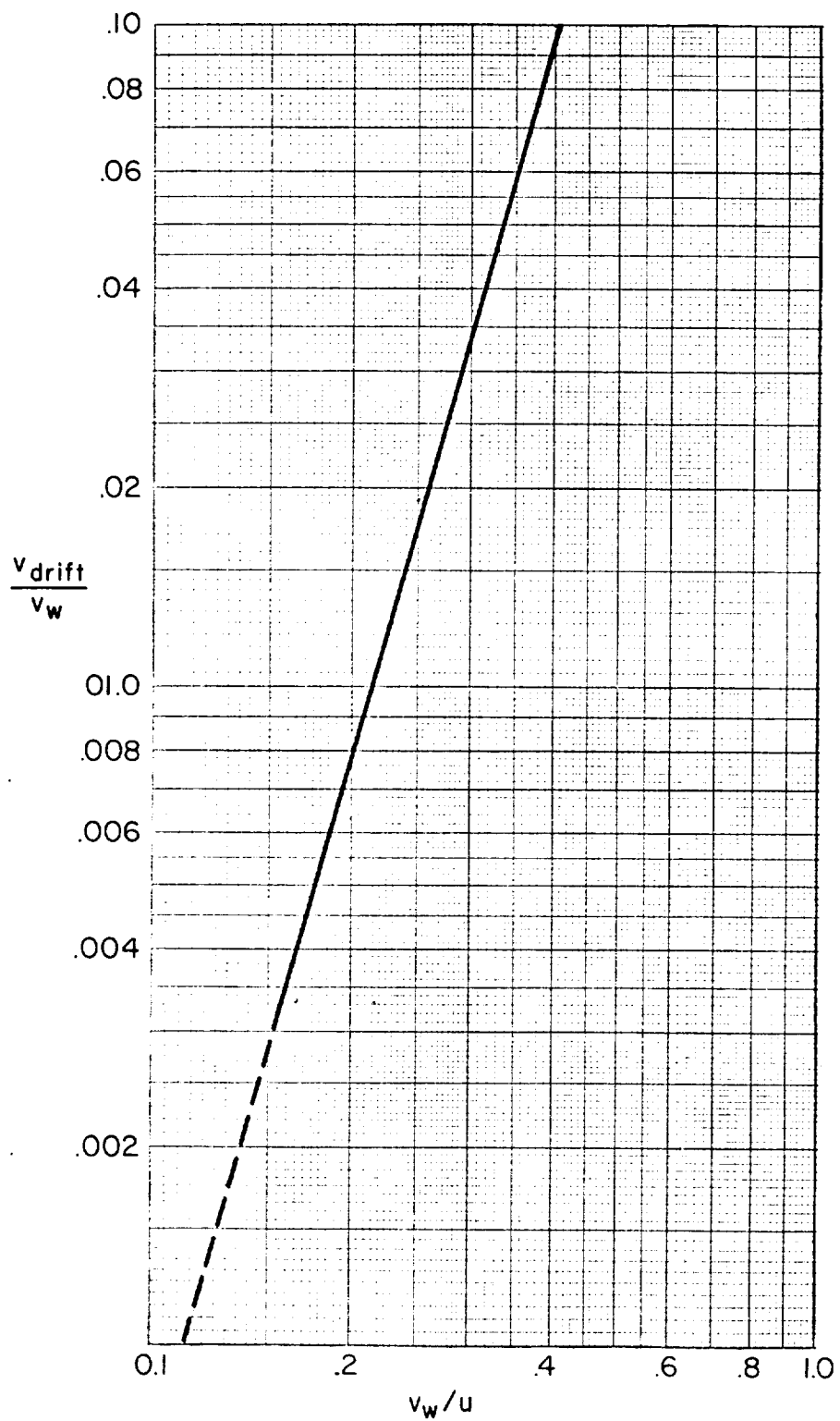
Figure 41. Effect of Wind-to-Airspeed Ratio on Orbit
Drift Rate, Circular Path Algorithm

mentioned, either incremental roll angle command modulation or auxiliary throttle control could be used to cure this.

Further simulation runs indicated that this algorithm is insensitive to the initial orientation relative to the wind vector, and this factor is not related to the divergence.

C. DEAD RECKONED WING-POINTING ALGORITHM

A simpler and more effective way of maintaining a stable orbit can be realized by taking a few hints from these results as well as extant naval search and rescue flying techniques. Such "wing pointing" techniques give proper alignment of the centripetal acceleration vector, and are usually combined with altitude or airspeed modulation to give the desired stable orbit.

In the current problem, altitude or speed modulation is not desirable. Also, of course, a circular resultant orbit is an overly restrictive requirement. Too, the divergence of the above orbiting algorithm may be related to failure to establish an imaginary orbit reference point. Consideration of all these factors leads to a simple, "dead reckoned wing-pointing" algorithm.

1. Problem

Fly closed path over ground, under steady wind, such that the acceleration vector lies along the wing, is of appropriate magnitude, and is directed toward a fixed point.

Assume:

- Constant airspeed magnitude, $|\bar{V}_a|$
- Zero sideslip, no vehicle dynamics
- Heading angle, ψ, available
- Orbit begins at $t=0^+$
- Constant wind vector, $\bar{V}_w$
- Fixed point on ground is x_o, y_o

2. Analysis
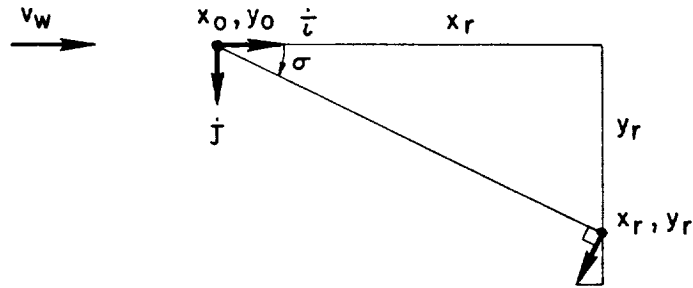
Figure 42. Dead Reckoned Reference Form

Let $x_o = y_o = 0$. Dead reckon X_r, Y_r from

$$\dot{x}_r = U \cos \psi + V_w \tag{33a}$$

$$\dot{y}_r = U \sin \psi \tag{33b}$$

Then, the orbital reference angle is:

$$\sigma = \tan^{-1} \left(\frac{y_r}{x_r}\right)$$

From the definition of wing pointing, set:

$$\psi \equiv \sigma + \frac{\pi}{2}$$

Then,

$$\frac{d\psi}{dt} \equiv \dot{\sigma} = \frac{d}{dt} \tan^{-1}\left(\frac{y_r}{x_r}\right)$$

$$= \frac{1}{1 + u^2} \frac{du}{dt} \quad , \quad \text{where } u = \frac{y_r}{x_r}$$

$$(\text{for } \pm \pi/2)$$

$$\frac{du}{dt} = \frac{d}{dt}\left(\frac{y_r}{x_r}\right) = \frac{\left(x_r \dot{y}_r - y_r \dot{x}_r\right)}{x_r^2}$$

$$\frac{d\psi}{dt} = \dot\sigma = \frac{1}{[1 + (y_r/x_r)^2]} \times \frac{(x_r \dot y_r - y_r \dot x_r)}{x_r^2}$$

$$= \frac{x_r \dot y_r - y_r \dot x_r}{\left(x_r^2 + y_r^2\right)}$$

Since,

$$\dot x_r = U \cos \psi + V_w$$

$$\dot y_r = U \sin \psi$$

Then

$$\frac{d\psi_c}{dt} = \frac{x_r\, U \sin \psi - y_r \left(U \cos \psi + V_w\right)}{\left(x_r^2 + y_r^2\right)} \qquad (34)$$

which leads to the command roll angle,

$$g \tan \phi_c = \dot\psi_c U$$

$$\phi_c = \tan^{-1} \frac{U}{g} \dot\psi_c \qquad (35)$$

Figures F-1 to F-3 of Appendix F show the resulting time histories for this algorithm. This confirms that orbit stability is independent of relative air and wind speeds (up to the limiting case of $V_a = V_w$). The drift rate is zero, within the limits of numerical computation accuracy. The shape of the orbit itself is dependent on relative speeds, and results in a superellipse for non-zero windspeed. This is elongated along an axis perpendicular to the wind, as shown in Fig. 43. As wind speed increases, the dimensions of the superellipse expand. Also shown in Fig. 43 are the arc lengths covered by the vehicle during equal increments of time.
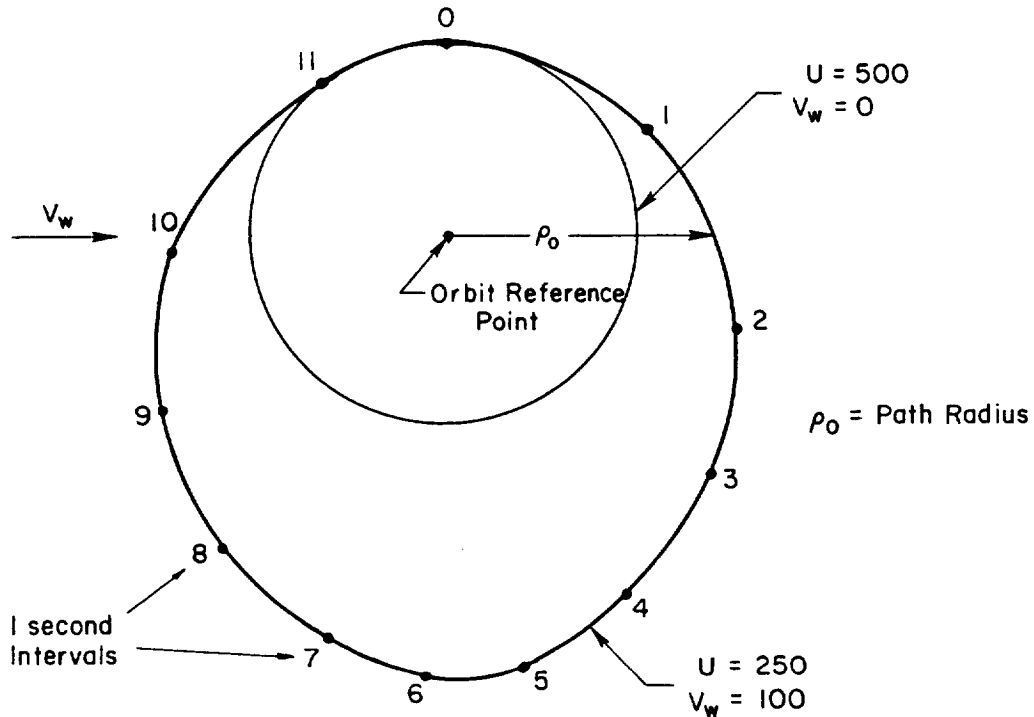
Figure 43. Effect of Wind and Airspeed on Vehicle
Orbit Shape, Wing Pointing Algorithm

Further analyses have shown that this algorithm obeys Kepler's Law
of Areas, i.e., equal areas of arc are swept out in equal lengths of
time. Also, it is not an inverse distance-squared form resulting in
simple planetary-like ellipses, but instead results in a higher order
trajectory.

D. CONCLUSIONS AND RECOMMENDATIONS

A wing pointing algorithm, where the heading rate is varied so that
the wing always points towards a dead reckoned orbit reference point, is
the recommended approach to maintaining autonomous RPV orbits in the
presence of winds. The resulting superelliptical orbit is entered when
the vehicle is parallel to the estimated wind. The required heading
rate is translated to a roll angle command. The basic requirements for
mechanizing the algorithm are: onboard inertial heading and airspeed

signals; an estimate of wind speed at orbit initiation; and onboard firmware/hardware computation of the needed trigonometric, arithmetic and integration operations (of Eqs. 33, 34, and 35).

Clearly, the next step in these analyses should be to examine the effects of non-idealized assumptions, such as:

- Actual wind variation (magnitude and direction)

- Sensor noise, drift and resolution

- Vehicle dynamics

- Interface with other autonomous modes

More real-world data is needed to perform these analyses.

SECTION VI

AUTONOMOUS NAVIGATION AND LANDING CONSIDERATIONS

Upon loss of uplink signal it is desired (Ref. 3) that the onboard control system autonomously navigate from any point at which uplink loss occurs to a safe orbit area, deorbit, and land. The performance requirements for the system include maintenance of a position accuracy within a CEP of 100 feet when operating with radar updates. For safe orbiting, the required accuracy is a CEP of 3 to 4 nmi. An additional performance objective is a CEP of 1 nmi as this would allow consideration of an autonomous recovery mode (landing) as an extension to the system concept. The system is to operate in a latitude/longitude coordinate system with radar position updates in the same form.

This can be accomplished by using a simple navigation and control scheme similar to that employed in the Aquila RPV (Ref. 14). The Aquila is a small reconnaissance drone which includes an autonomous dead reckoning and orbit mode upon loss of telemetered uplink command.

A key element in the Aquila system is a strapdown magnetometer which senses vehicle heading. The magnetometer and associated electronics is off-the-shelf, small, and light weight (4.5 cubic inch, 3.5 oz.). It measures the magnetic field in vehicle x, y, z coordinates with the x and y components used to calculate magnetic heading. When operating in a relatively small area (such as the DFRF test area) of known declination and magnetic anomaly and with calibration for vehicle magnetic fields, the sensed heading is quite accurate.

Under normal operations, vehicle range, azimuth, and altitude from the FPS-16 tracking radar can be uplinked and stored in an onboard navigation computer module. Vehicle position and groundspeed can then be computed in either polar or rectangular coordinates. When combined with onboard sensing of airspeed and heading, the direction and magnitude of

wind can be determined and maintained in the computer. Likewise, heading and range from the vehicle current position to the position coordinates of a safe orbiting area can be computed continuously. Then upon loss of uplink the vehicle can be immediately commanded to the heading of the safe orbit area. Estimated groundspeed can be calculated from measured airspeed and the wind data stored in the computer. The vehicle is then dead reckoned to the safe orbit position on the basis of heading, groundspeed, and elapsed time. Again, the basics of this navigation system are contained in the Aquila RPV and need only minor computational additions.

Upon reaching the coordinates for entering the autonomous orbit mode, the computer can command the vehicle into the wind pointing orbit of Section V and a barometric rate of descent. The vehicle will then spiral down until a deorbit command can be given. Deorbit is established by radar altimeter and heading measurements. After reaching a preselected radar altitude and the appropriate heading, the vehicle is commanded to a wings level, constant heading descent to the lakebed runway. Autonomous flare and landing can then be accomplished by the proposed (or present) flare control law (Section III).

Based upon available data, it appears that the Edwards precision bombing range would provide a safe orbit area with the possibility of an autonomous landing. Figure 37 is a map of the precision bombing range and shows that an orbit of up to 5 miles diameter can be easily accommodated. The orbit can be made target to an extension of the runway 25 centerline. By flying the orbit in a clockwise direction the vehicle can intercept the runway alignment and then fly a straight approach to landing.

Figure 38 is a topographical representation of the terrain elevation versus range along the approach to runway 25. It shows the ground to be essentially a constant slope of approximately 0.7 deg. If the Fig. 2 2.8 deg descent is retained, the approach would be flown at about 2 deg with respect to the ground.
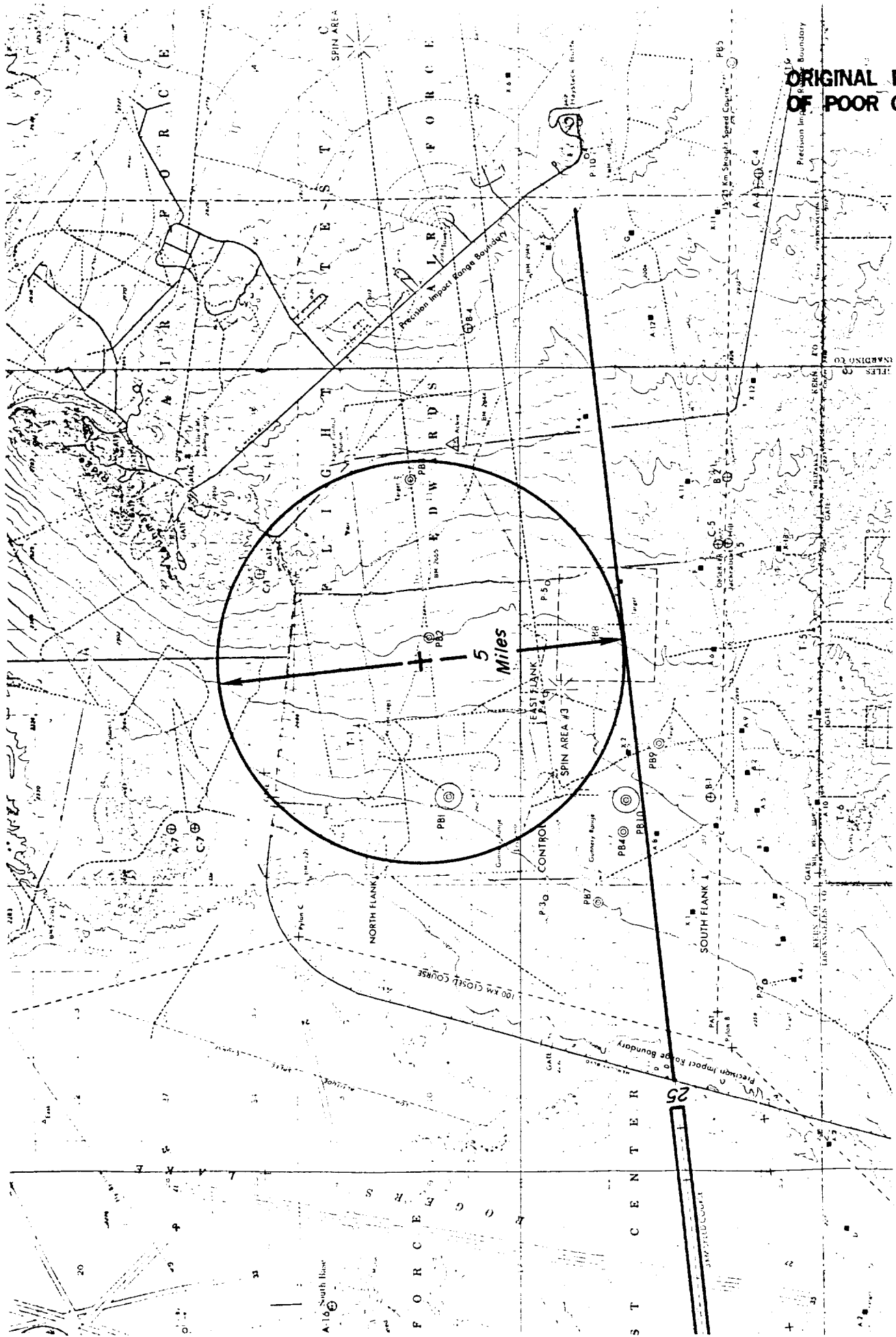
Figure 37. Proposed Autonomous Orbit and Approach Pattern Within the
Precision Impact Range Boundaries
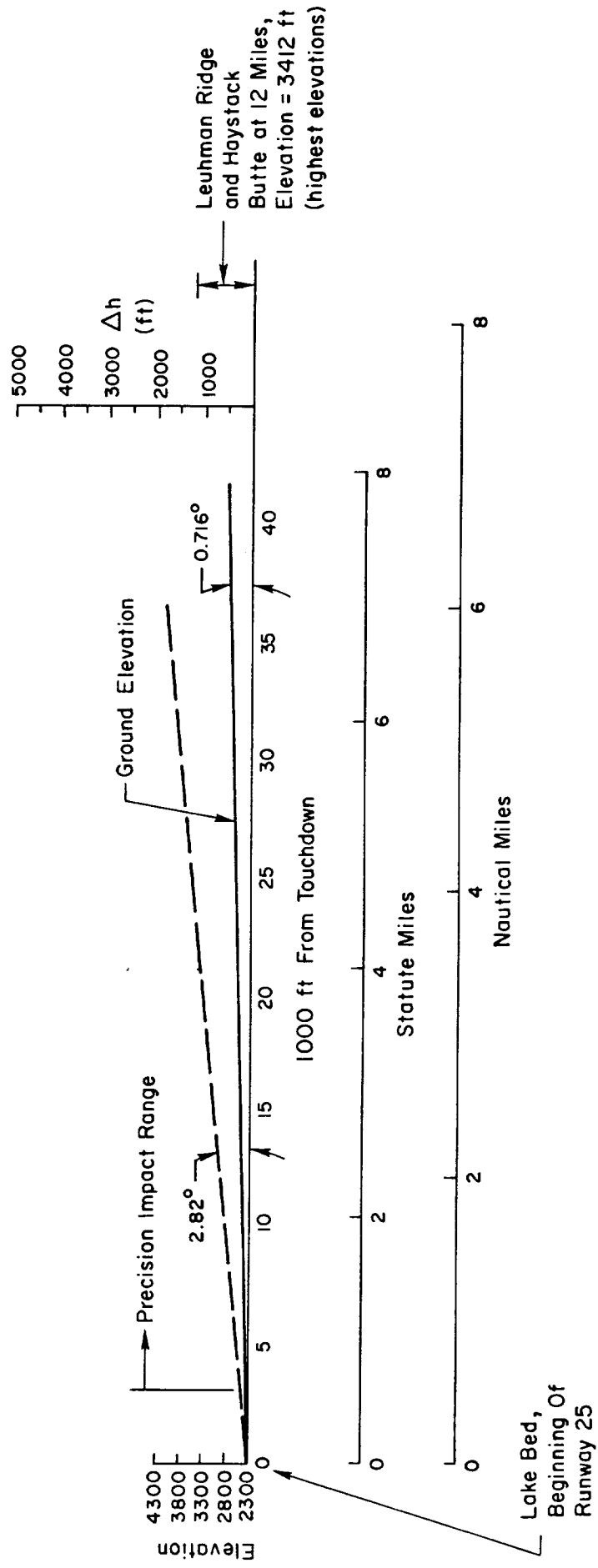
Figure 38. Ground Elevation on Runway 25 Centerline Approach
Through Precision Impact Range

This approach may or may not result in a landing on runway 25 but, in any case it should

      -- be close

      -- not cause any safety problems

      -- minimize risk of property or vehicle damage

Thus, it appears that the autonomous navigation, orbit, and landing is not only feasible but highly promising.

REFERENCES

1. Anon, HIMAT AV-1 Fact Sheet, OFS 870-81-1, 5 May 1981.

2. Telecon, Mr. Jack Kittrell, NASA, DFRF, 19 May 1982.

3. Anon, Statement of Work for Autonomous RPRV Navigation, Guidance, and Control, Contract NAS4-2866.

4. Gee, Shu W., et al., Development of Systems and Techniques for Landing on Aircraft Using Onboard Television, NASA TP-1171, Feb. 1978.

5. Gera, Joseph, HIMAT BCS Validation During Approach and Landing Using the PA-30 Airplane; Program Plan, 15 April 1978.

6. Edwards, John W., Summary of Flight Tests and Analysis of the HIMAT BCS Approach and Landing System Using the PA-30 Airplane, Interval DFRF Memo AR/VD&C/JWE/98, 22 Nov. 1978.

7. Lambergts, A. A., "What You Always Wanted to Know About the Pitfalls of Autoland Flare Control System Design, But Were Afraid to Ask," paper presented at Meeting 48, SAE Aerospace Control and Guidance Systems Committee, Melbourne, FL, Oct. 28-30, 1981.

8. Lambregts, A. A., and J. F. Creedon, "Development and Flight Evaluation of Automatic Flare Laws With Improved Dispersion," AIAA Paper 80-1757.

9. Foster, J. L., "Microwave Landing System Effect on the Flight Guidance and Control System," AIAA Paper 72-755, Aug. 1972.

10. Smitchers, A., and R. R. Huber, "RPV Autoland," SAE Paper 751113, Nov. 1975.

11. Marhav, S. J. and A. J. Grunwald, "Display Agumentation in Manual Control of Remotely Piloted Vehicles," J. Aircraft, Vol. 15, No. 3, Mar. 1978.

12. Howard, J. C., Display Requirements for the Final Approach and Landing Phase of a RPV Mission, NASA TMX-62346, Apr. 1974.

13. Hoh, R. H., R. H. Klein, and W. A. Johnson, Development of an Integrated Configuration Management/Flight Director System for Piloted STOL Approaches, NASA CR-2883, Aug. 1977.

14. Anon, Aquila RPV System Technology Demonstration Program. Volume I: System Description and Capabilities, USARTL-TR-78-37A, Apr. 1979.
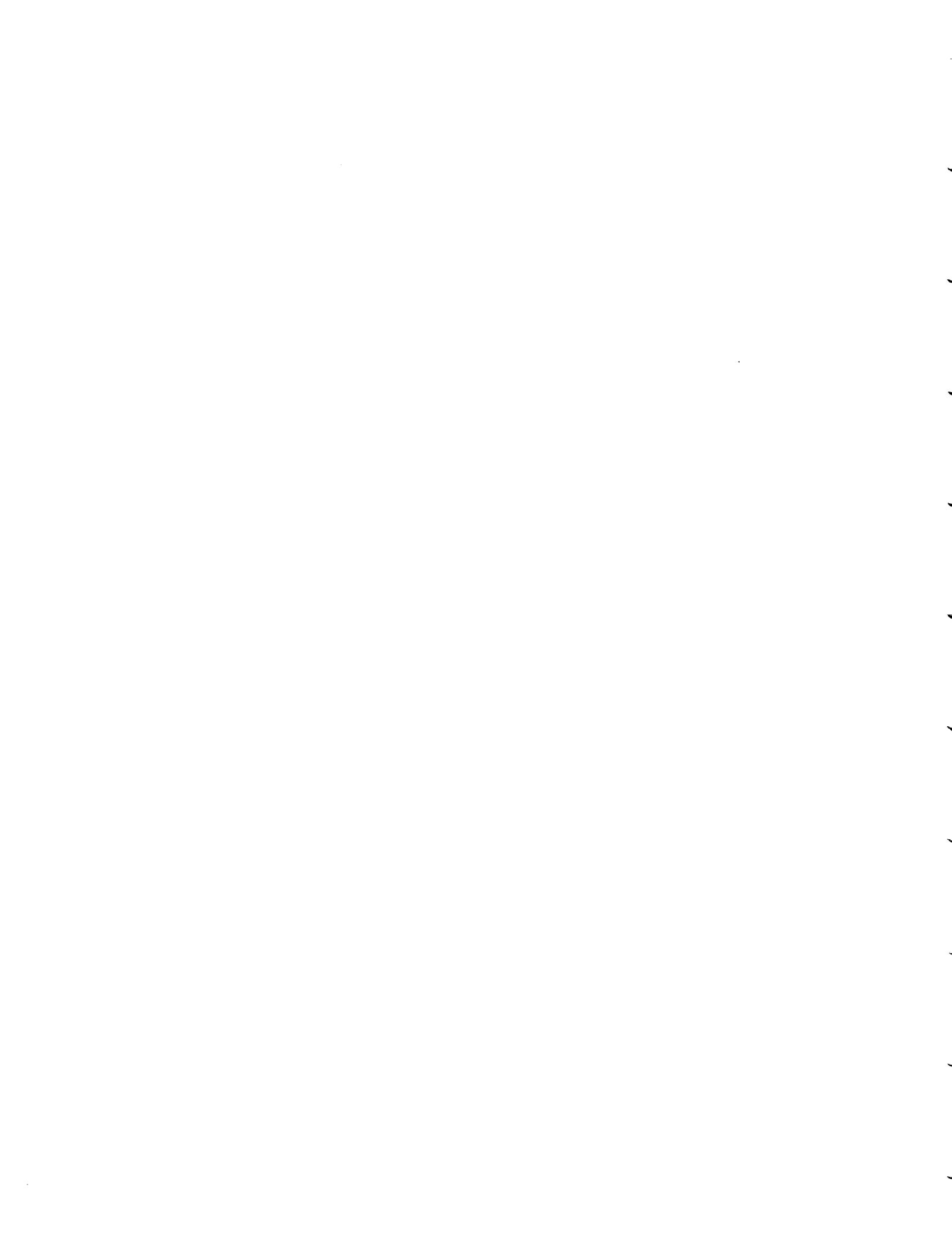
APPENDIX A

A. RECONSTRUCTION OF THE PA-30 LONGITUDINAL AIRFRAME AND FLIGHT CONTROL SYSTEM MODEL

This appendix documents an effort to reconstruct the mathematical model of the PA-30 airframe and flight control system for the longitudinal modes employed in Ref. A-1. There Edwards presents flight test data for evaluation of the HIMAT approach and landing backup control system (BCS) using the PA-30 airplane, results of a nonlinear simulation implemented on the NASA Dryden CYBER computer, and results from linear analyses of the pitch autoland system. It was desired to use these analytical models in this study (Ref. A-2). However, a check of the Ref. A-1 analysis showed some large discrepancies. It was then necessary to reconstruct the Ref. A-1 model and this required combining the Ref. A-1 data with data from other sources, i.e., Ref. A-3 through A-7. As a result, a linear, small perturbation longitudinal model of the airframe and BCS control system has been developed which matches selected root locus and Bode plots from Ref. A-1. This model is presented in Subsection 1 and the process by which it was generated is discussed in Subsection 2.

1. Reconstructed Model

The linear longitudinal model of the airframe and flight control system presented in Ref. A-1 is reproduced here as Table A-1. The pressure altitude of 3350 ft above sea level corresponds to a radar altitude of 1000 ft above ground level. The true airspeed of 186 ft/sec is an approximation of the approach speed of 110 kt indicated. The values of N_z and N_x imply a flight path angle of −5 deg and at this speed is consistent with a rate of descent of 1,000 ft/min. These flight parameters, along with geometric and inertial data obtained from Refs. A-3 through A-7, are summarized in Table A-2.

Linearized small perturbation longitudinal airframe equations are given in Table A-3 consistent with the assumptions and notation of Ref. A-8 for stability axes. The nondimensional and dimensional stability and control derivatives finally evolved are given in Table A-4. These derivatives when used with the equations of motion of Table A-3 produce the Table A-5 bare airframe transfer functions. The Table A-5 denominator checks closely with that of Table A-1. Table A-1 does not contain transfer function numerators (zeros) but the correctness of the Table A-5 zeros are implied from the loop closures to be discussed below.

Figure A-1 shows the portion of the BCS flight control system consisting of feedbacks to the elevator. (The autothrottle system will be considered later). The control system gains are summarized in Table A-6 as a function of switch position. It should be noted that the gains in the proportional and integral pitch rate feedback paths are not the same as given in Ref. A-1. Transfer function models for key control system elements are presented in Table A-7. Provision is made in Fig. A-1 for effective time delay and hysteresis in the elevator feedback but they were not included in the initial analysis.

To verify that the model outlined above matches the closed-loop dynamics of Ref. A-1, loop closures were made in the same sequence as in Ref. A-1. Figure A-2 shows the closure of the rate of climb loop, $\dot{h} \rightarrow \delta_e$, with the a_z and q loops open. Without the latter loops closed, the phugoid mode is driven unstable. Figure A-3 shows the comparable locus of Ref. A-1. The close agreement verifies $N_{\delta_e}^h$ in Table A-5 and the use of KIHD in Table A-6.

Figure A-4 shows the closure of the pitch rate loops about the rate of climb loop but with the a_z loop open. The pitch rate closure restabilizes the phugoid mode while destabilizing the servo mode. This closure corresponds to the loci labeled "q_1" in Fig. A-5 (taken from Ref. A-1). The close agreement of Figs. A-4 and A-5 at switch position 4 verifies the $N_{\delta_e}^\theta$ numerator and the KQAL and KIQ gains shown in Table A-6. (As will be explained in Subsection 2, these q loop gains are not those given in Ref. A-1 but rather come from Ref. A-9).

Finally, Fig. A-6 shows the closure of the last loop, $a_z \rightarrow \delta_e$, with the other loops closed. It may be seen that this loop has rather minimal effect. This closure should be compared to the "a_{n2}" loci of Fig. A-5. The close match of the final root location requires the B gain set at 4 (KINZ = 0.1919 deg/g) rather than at 2 as in Ref. A-1. Since this loop has little influence this difference can be neglected. The results tend to verify the $N_{\delta_e}^{a_z} a$ zeros of Table A-5.

The Fig. A-7 solid line Bode plot shows the resulting open-loop transfer function with the loop opened at the servo command point (the dashed curves will be discussed in the next section). The system gains correspond to the 441 setting for Table A-6 and thus this response may be compared to Fig. 24 in Ref. A-1, reproduced here as Fig. A-8. This comparison shows a good match between the amplitude and phase curves at low frequencies. The comparison does not appear good at high frequency however, because Fig. A-8 reflects a discrete frequency response in the w'-domain and includes digital artifacts not included in the s-domain analysis of Fig. A-7. As noted in Fig. A-7 this phase lag difference is equivalent to an effective time delay of about 0.063 sec which is appropriate for the uplink delay of Fig. A-1.

2. Reconstruction of the Model

Because complete details were not provided in Ref. A-1, considerable iteration and trial and error gain analysis was required to obtain the match presented in Subsection 1. The altitude and speed were specified for the reference case as 1000 ft AGL and 110 kt indicated. The flight path angle, γ, was derived from the BCS scheduled altitude rate command of 1000 ft/min at a radar altitude of 1000 ft. This is consistent with the n_z and n_x values given in Table A-1 since, if we assume the use of stability axes,

$$\sin^{-1}(0.0849) = \cos^{-1}(0.9964) = 4.9 \text{ deg}$$

From this flight condition the trim may be estimated using

$$L \doteq W \qquad\qquad (A\text{-}1a)$$

$$T = D + W\gamma_o \qquad\qquad (A\text{-}1b)$$

which gives an estimate of the trim lift coefficient as

$$C_L \doteq \frac{W}{(1/2)\rho U_o^2 S}$$

$$= 0.491 \qquad\qquad (A\text{-}2)$$

Since airframe aerodynamic, mass and geometric data are not specifically identified in Ref. A-1, an initial model was constructed from data in Refs. A-3 through A-7 and used to generate characteristic roots which were then checked against those shown in Table A-1. This initial estimate resulted in real short-period roots considerably different from those of Table A-1. After exploring the possibilities for uncertainties in the model, it was found necessary to extract the airframe parameters from the matrix equations of Table A-1. The state vector implies that the first four equations of the 8 × 8 "A" matrix are the longitudinal equations. It should be noted that this matrix indicates coupling of sideslip into the longitudinal motions and coupling of angle-of-attack and speed perturbations into the lateral-directional dynamics. The coupling of sideslip into the longitudinal motion does not seem justified since the airplane is supposedly in a symmetric ($\beta_o = 0$) flight condition. The fourth equation may be seen to be $\dot\theta = q$ consistent with Table A-3. The third equation is the pitching moment or $\dot q$ equation as indicated by the fact that the attitude element, M_θ, is zero. The first equation is the x-force equation since the θ element is consistent with ($-g \cos \theta_o$). The fact that the q term in this equation is zero indicates

C-2

the use of stability axes. Finally, the second or $\dot{\alpha}$ equation is equivalent to the z-force equation of Table A-3 divided by U_o as indicated by the fact that the q term in the second equation is exactly 1. Thus, the equations used in Ref. A-1 can be considered equivalent to those of Table A-3 with the exception of the state variable formulation and the use of α instead of w.

It may be immediately noted that the Ref. A-1 formulation neglects the derivative $C_{m_{\dot{\alpha}}}$ since its presence would require inclusion as an apparent product of inertia term in the inertia matrix. This apparently was not done in Ref. A-1. Neglecting $C_{m_{\dot{\alpha}}}$ reduces considerably the modeled airframe-alone short period damping.

Since the equations of motion are divided through by mass and moment of inertia, it is not possible to verify these parameters independently of the aerodynamics. However, assuming the values obtained from Refs. A-3 through A-7 are correct, the aerodynamic stability derivatives may be identified in the Ref. A-1 matrix equation elements. From the q element of the pitching moment equation, M_q = -3.38 sec^{-1} which implies C_{m_q} = -14.4 rad^{-1}, considerably lower than the value of -25 rad^{-1} given in Refs. A-3 and A-5. The α element of the $\dot{\alpha}$ equation is Z_w = 1.98 sec^{-1} and indicates a C_{L_α} of approximately 6.1 rad^{-1}. This is about 26 percent higher than the value obtained from the wind tunnel data of Ref. A-6 and probably reflects the 30 percent increase in lift curve slope which was mentioned in Ref. A-1 as being required for the PA-30 simulation model. The M_α derivative as extracted from the α element of the pitching moment equation is -5.68 rad^{-1} which implies C_{M_α} = -0.325 rad^{-1}, and, when used with the C_{L_α} value above, indicates a static margin of only 5 percent c, which would appear to be too low for actual flight of the PA-30. Some additional differences were also found in the drag and elevator effectiveness derivatives.

Once the airframe parameters were extracted, loop closure checks were performed as discussed in Subsection 1. Originally these root loci were generated using a gain/gain switch table in Ref. A-1. However, the Ref. A-1 A gains (q loop gains) did not produce a good match with the Ref. A-1 loop closures. It was found that q loop gains given in

Ref. A-9 provided an excellent match and these are given in Table A-6 combined with B and C gains from Ref. A-1. It is further assumed that these later of loop gains were actually used in flight.

A comparison between the derivatives extracted from the Ref. A-1 matrix and those derived from the Refs. A-3 through A-7 wind tunnel data, theoretical estimates, and simulation models are compared in Table A-8. The resulting difference in system dynamics is shown in Fig. A-7 where the frequency response shown by the solid line corresponds to the reconstructed model as derived from the Ref. A-1 matrix. The amplitude and phase curves shown in the dashed line corresponds to the Table A-8 derivative set obtained from Refs. A-3 through A-7. While the general shape of the magnitude and phase curves is quite similar, the Refs. A-3 through A-7 derivatives produce a much lower gain over the frequency range up to 10 rad/sec. This would result in considerable droop and sloppy control in the region above 1 rad/sec. Since the Ref. A-1 simulation appeared to match flight results very well it is presumed the Ref. A-1 aero coefficients are the better set. Thus, while the stability derivatives reconstructed from the Ref. A-1 matrix will be used in further analyses, it should be remembered that there is significant sensitivity to uncertainties in the airframe dynamics that may effect closed-loop response. Furthermore, it is not obvious that the Refs. A-1, A-3, or A-5 simulations adequately model the propwash effects.

3. Airframe Characteristics at 80 kts

After the airframe characteristics were reconstructed for 110 kts, the stability derivatives were adjusted for $n_z = 1$ g, $\gamma \doteq 0$ flight at 80 kts (see Table A-9). The four elevator transfer functions for this case are tabulated in Table A-10.

TABLE A-1. PA-30 APPROACH AND LANDING MATH MODEL FROM
REFERENCE A-1 (REPRODUCTION OF TABLE 2 IN REFERENCE A-1)

```
H = 3350.0    V = 185.00    MACH = .17    THRUST = 383.124

ALP =   4.8697    BTA =  0.0000    THA =   4.8697    PHI =   0.0000

DE  =    .6169    DA  =  0.0000    DR  =   0.0000    DO  =   0.0000

P   =  0.0000     Q   =  0.0000    R   =   0.0000

NX  =    .0849    NY  =  -.0646    NZ  =   -.9964
```

V,ALP,Q,THA,P,R,BTA,PHI

v	α	q	θ	P	r	β	ϕ
-.3570E-01	.1492E+02	0.	-.3216E+02	0.	0.	-.2204E+00	0.
-.1777E-02	-.1978E+01	.1000E+01	.3309E-12	0.	0.	0.	0.
-.3761E-03	-.5679E+01	-.3378E+01	0.	0.	0.	-.4446E-03	0.
0.	0.	.1000E+01	0.	0.	0.	0.	0.
0.	-.7313E+00	0.	0.	-.4105E+01	.1216E+01	-.4005E+01	0.
0.	-.1262E+00	0.	0.	-.5895E+00	-.5033E+00	.3707E+01	0.
.6441E-05	-.7697E-02	0.	0.	.8489E-01	-.9964E+00	-.1029E+00	.1732E+00
0.	0.	0.	0.	.1000E+01	.8520E-01	0.	0.

DE,THRUST,DA,CR

δ_e	T	δ_A	δ_R
.5955E+01	.8618E-02	0.	0.
-.2618E+00	-.2470E-04	0.	0.
-.4020E+02	.9080E-04	0.	0.
0.	0.	0.	0.
0.	-.1955E-03	.6624E+01	.7575E+00
0.	-.1941E-03	.1670E+00	-.3028E+01
0.	-.3110E-05	0.	.2009E-01
0.	0.	0.	0.

NZ,NY

-.1028E-01	-.1129E+02	0.	.1639E-04	0.	0.	0.	0.
.1388E-13	-.4426E-01	0.	0.	0.	0.	-.5916E+00	-.1924E-03
-.1485E+01	-.1188E-03	0.	0.				
0.	-.1788E-04	0.	.1155E+00				

```
MACH NO. = .17    ALTITUDE = 3350.00 FT
```

DENOMINATOR ROOTS

REAL	IMAGINARY	OMEGA	ZETA	TAU
-2.67980	-2.28068	3.51893	.76154	0.00000
-2.67980	2.28068	3.51893	.76154	0.00000
-.01591	-.15502	.15583	.10213	0.00000
-.01591	.15502	.15583	.10213	0.00000

TABLE A-2. FLIGHT CONDITION AND AIRCRAFT CONFIGURATION

Altitude, h	1000 ft above ground level 3350 ft above sea level
Airspeed, U_o	186 fps true (approximation of 110 KIAS)
Flight path angle, γ_o	-5 deg
Trim, C_L	0.49
Trim, C_D	0.056
Reference planform area, S	178 ft^2
Reference chord, c	5.00 ft
Weight, W	3600 lb
Pitch axis moment of inertia, I_x	1900 slug-ft^2

TABLE A-3. LONGITUDINAL AIRFRAME EQUATIONS

- Linearized small perturbation form

- Stability axis, $\gamma_0 = \theta_0$, $\alpha_0 = 0$

Equations of Motion

$$(s - X_u)u - X_w w + g \cos \theta_0 \theta = X_{\delta_e}\delta_e + X_{\delta_T}\delta_T$$

$$-Z_u u + (s - Z_w)w + (-U_0 s + g \sin \theta_0)\theta = Z_{\delta_e}\delta_e + Z_{\delta_T}\delta_T$$

$$-M_u u - (M_{\dot{w}} + M_w)w + (s^2 + M_q s)\theta = M_{\delta_e}\delta_e + M_{\delta_T}\delta_T$$

$$s\theta = q$$

Altitude Rate at the c.g., $\dot{h}$

$$sh = \dot{h} = \sin \theta_0 u - \cos \theta_0 w + U_0 \cos \theta_0 \theta$$

z-Axis Acceleration at Accelerometer Location, a_{z_a}

$$a_{z_a} = \dot{w} - U_0 \dot{\theta} + g \sin \theta_0 \theta - \ell_{x_a}\ddot{\theta}$$

Accelerometer is assumed to be mounted at the instant center for elevator inputs, $\ell_{x_a} = 1.21$ ft forward of c.g.

TABLE A-4. STABILITY AND CONTROL DERIVATIVES (110 kts)

NON-DIMENSIONAL		DIMENSIONAL	
STABILITY DERIVATIVES			
C_{D_u}	0	$X_u = \dfrac{\rho SU}{m}\left(-C_D - C_{D_u}\right)$	-0.03567 sec^{-1}
C_{D_α}	0.24 rad^{-1}	$X_w = \dfrac{\rho SU}{2m}\left(C_L - D_{D_\alpha}\right)$	0.07962 sec^{-1}
C_{L_u}	0	$Z_u = \dfrac{\rho SU}{m}\left(-C_L - C_{L_u}\right)$	-0.3121 sec^{-1}
C_{L_α}	6.15 rad^{-1}	$Z_w = \dfrac{\rho SU}{2m}\left(-C_{L_\alpha} - C_D\right)$	-1.976 sec^{-1}
C_{M_u}	0	$M_u = \dfrac{\rho SUc}{I_y}\left(C_M + C_{M_u}\right)$	0.0002425*(ft/sec)$^{-1}$
C_{M_α}	-0.325 rad^{-1}	$M_w = \dfrac{\rho SUc}{2I_y} C_{M_\alpha}$	-0.03048 (ft/sec)$^{-1}$
$C_{M_{\dot\alpha}}$	0	$M_{\dot w} = \dfrac{\rho Sc^2}{4I_y} C_{M_{\dot\alpha}}$	0 ft^{-1}
C_{M_q}	-14.4 rad^{-1}	$M_q = \dfrac{\rho SUc^2}{4I_y} C_{M_q}$	-3.376 sec^{-1}
CONTROL (ELEVATOR) DERIVATIVES			
$C_{D_{\delta_e}}$	0 rad^{-1}	$X_{\delta_e} = -\dfrac{\rho SU^2}{2m} C_{D_{\delta_e}}$	0 ft/rad sec^2
$C_{L_{\delta_e}}$	0.818 rad^{-1}	$Z_{\delta_e} = -\dfrac{\rho SU^2}{2m} C_{L_{\delta_e}}$	-48.45 ft/rad sec^2
$C_{M_{\delta_e}}$	-2.30 rad^{-1}	$M_{\delta_e} = \dfrac{\rho SU^2}{2I_y} C_{M_{\delta_e}}$	-40.12 $\left(\text{rad/sec}^2\right)^{-1}$

*Due to thrust axis 0.75 ft above and parallel to X_{stab}.

TABLE A-5. AIRFRAME-ALONE ELEVATOR TRANSFER FUNCTIONS (110 kts)

$$\Delta = [0.1185, 0.1620][0.762, 3.51]$$

$$N_{\delta_e}^{u} = -3.86(3.59)(-179.8) \frac{fps}{rad}$$

$$N_{\delta_e}^{w} = -48.5(157.4)[0.1086, 0.231] \frac{fps}{rad}$$

$$N_{\delta_e}^{\theta} = -40.1(0.0488)(1.926) \frac{rad}{rad}$$

$$N_{\delta_e}^{a_{z}a} = 0.0864[0.661, 0.0271][-0.982, 409.] \frac{ft/sec^2}{rad}$$

$$N_{\delta_e}^{\dot{h}} = 48.3(0.0356)(-15.64)(19.03) \frac{fps}{rad}$$

Notation: $K(a)[\zeta, \omega] = K[s + a][s^2 + 2\zeta\omega s + \omega^2]$

TABLE A-6. CONTROL SYSTEM GAINS

| SWITCH POSITION | GAIN | | | |
| | A | | B | C |
	KQAL rad/(rad/sec)	KIQ* rad/rad	KINZ deg/g	KIHD deg/fps
1	0.1	0.3696	0.0768	0.275
2	0.15	0.5544	0.1151	0.275
3	0.2	0.7392	0.1535	0.275
4	0.25	0.9240	0.1919	0.275

$$^*\text{KIQ} = 3.696 \text{ KQAL}$$

The gains for each of the 3 loops ($q \to \delta_e$, $a_z \to \delta_e$, $\dot{h} \to \delta_e$) may be varied independently by setting the "A", "B", and "C" switches. The gain set is specified by the ABC switch sequences, e.g., the "441" gains are (KQAL = 0.25, KIQ = 0.9240, KINZ = 0.1919, KIHD = 0.275)

TABLE A-7. CONTROL SYSTEM ELEMENTS

Datametrics Rate-of-Climb Sensor

$$G_{\dot{h}}(s) = \frac{s}{\left(\frac{s}{5} + 1\right)^2 \left(\frac{s}{10} + 1\right)}$$

Elevator Servo

$$\frac{\delta_e}{\delta_{e_c}}(s) = \frac{1}{\left[\left(\frac{s}{26.6}\right)^2 + \frac{2(0.7)}{26.6} s + 1\right]}$$

No Delay or hysteresis

$$\frac{\delta_{e_c}}{\delta_{e_f}} = 1.0$$

TABLE A-8. COMPARISON OF STABILITY AND CONTROL DERIVATIVES FROM
REF. A-1 MATRIX AND FROM REFS. A-3 THROUGH A-7 (110 kts)

DERIVATIVE	FROM REF. A-1[*] MATRIX	FROM REFS. A-3 THROUGH A-7 (Wind Tunnel Data, Theoretical Estimates)
C_{L_α} 1/rad	6.15	4.87
$C_{D_{trim}}$	0.056	0.047
C_{D_α} 1/rad	0.24	0.334
C_{M_α} 1/rad	-0.325	-0.974
$C_{M_{\dot\alpha}}$ 1/rad	0.	-14.6
C_{M_q} 1/rad	-14.4	-25.0
$C_{L_{\delta_e}}$ 1/rad	0.818	1.03
$C_{M_{\delta_e}}$ 1/rad	-2.30	-2.64

[*]Reference A-1 matrix reproduced in Table A-1, derivatives shown
here are the same as Table A-4.

NON-DIMENSIONAL		DIMENSIONAL		
STABILITY DERIVATIVES				
C_{D_u}	0	$X_u = \dfrac{\rho SU}{m}\left(-C_D - C_{D_u}\right)$		$-0.0381\ \text{sec}^{-1}$
C_{D_α}	$0.46\ \text{rad}^{-1}$	$X_w = \dfrac{\rho SU}{2m}\left(C_L - C_{D_\alpha}\right)$		$0.112\ \text{sec}^{-1}$
C_{L_u}	0	$Z_u = \dfrac{\rho SU}{m}\left(-C_L - C_{L_u}\right)$		$-0.443\ \text{sec}^{-1}$
C_{L_α}	$6.15\ \text{rad}^{-1}$	$Z_w = \dfrac{\rho SU}{2m}\left(-C_{L_\alpha} - C_D\right)$		$-1.48\ \text{sec}^{-1}$
C_{M_u}	0	$M_u = \dfrac{\rho SUc}{I_y}\left(C_M + C_{M_u}\right)$		$0.00168^*(\text{ft/sec})^{-1}$
C_{M_α}	$-0.325\ \text{rad}^{-1}$	$M_w = \dfrac{\rho SUc}{2I_y}\,C_{M_\alpha}$		$-0.0228\ (\text{ft/sec})^{-1}$
$C_{M_{\dot\alpha}}$	0	$M_{\dot w} = \dfrac{\rho Sc^2}{4I_y}\,C_{M_{\dot\alpha}}$		$0\ \text{ft}^{-1}$
C_{M_q}	$-14.4\ \text{rad}^{-1}$	$M_q = \dfrac{\rho SUc^2}{4I_y}\,C_{M_q}$		$-2.52\ \text{sec}^{-1}$
CONTROL (ELEVATOR) DERIVATIVES				
$C_{D_{\delta_e}}$	$0\ \text{rad}^{-1}$	$X_{\delta_e} = -\dfrac{\rho SU^2}{2m}\,C_{D_{\delta_e}}$		$0\ \text{ft/rad sec}^2$
$C_{L_{\delta_e}}$	$0.818\ \text{rad}^{-1}$	$Z_{\delta_e} = -\dfrac{\rho SU^2}{2m}\,C_{L_{\delta_e}}$		$-26.3\ \text{ft/rad sec}^2$
$C_{M_{\delta_e}}$	$-2.30\ \text{rad}^{-1}$	$M_{\delta_e} = \dfrac{\rho SU^2}{2I_y}\,C_{M_{\delta_e}}$		$-21.8\ \left(\text{rad/sec}^2\right)^{-1}$

---

*Due to thrust axis 0.75 ft above and parallel to X_{stab}.

TABLE A-10. AIRFRAME-ALONE ELEVATOR TRANSFER FUNCTIONS (80 kts)

$$\Delta = [0.0528, 0.243][0.767, 2.62]$$

$$N_{\delta_e}^u = -2.94(2.74)(-126.6) \ \frac{\text{fps}}{\text{rad}}$$

$$N_{\delta_e}^w = -26.3(114.3)[0.0577, 0.322] \ \frac{\text{fps}}{\text{rad}}$$

$$N_{\delta_e}^\theta = -21.8(0.0741)(1.420) \ \frac{\text{rad}}{\text{rad}}$$

$$N_{\delta_e}^{a_z} = -26.3(0)(-0.000583)(-11.54)(14.10) \ \frac{\text{ft/sec}^2}{\text{rad}}$$

$$N_{\delta_e}^{\dot{h}} = 26.3(-0.000583)(-11.5)(14.10) \ \frac{\text{fps}}{\text{rad}}$$

Notation: $K(a)[\zeta,\omega] = K[s + a][s^2 + 2\zeta\omega s + \omega^2]$

Figure A-1. PA-30/BCS Elevator Channel
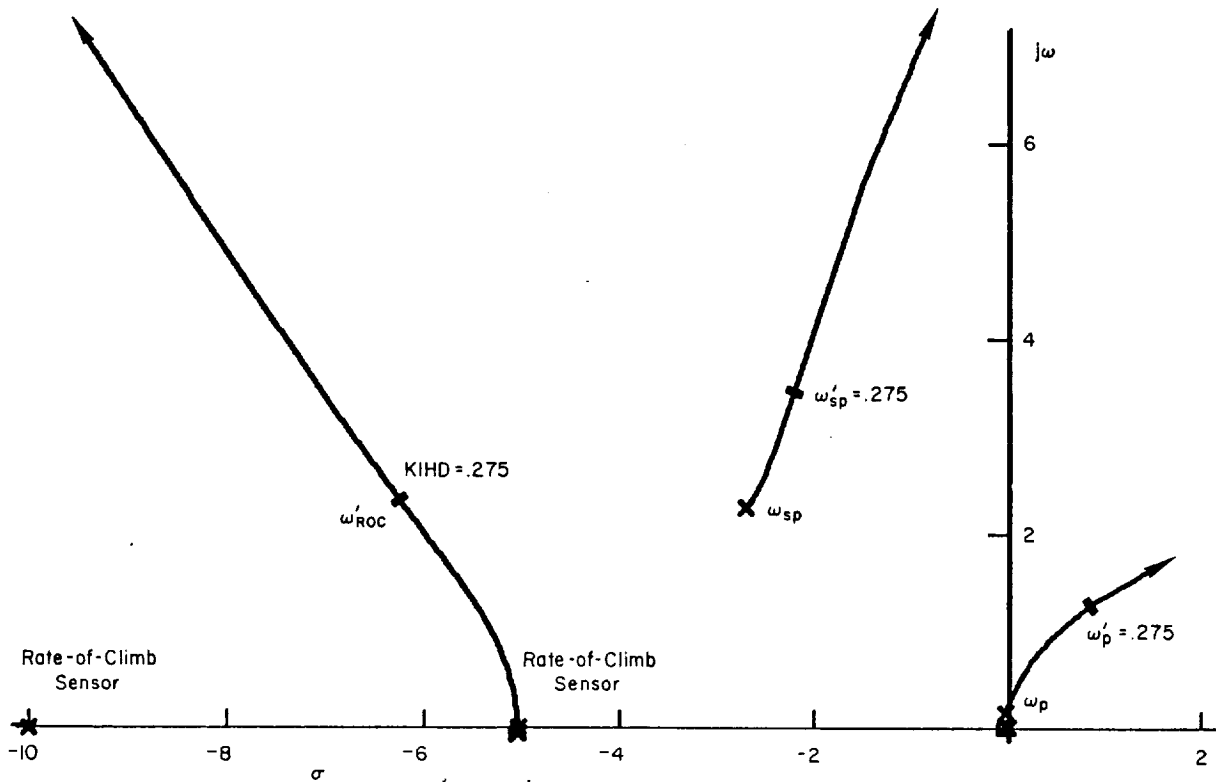
Figure A-2. Closure of the $\dot{h} \rightarrow \delta_e$ Loop With a_z, $q \rightarrow \delta_e$
and $u \rightarrow \delta_T$ Loops Open (110 kts)
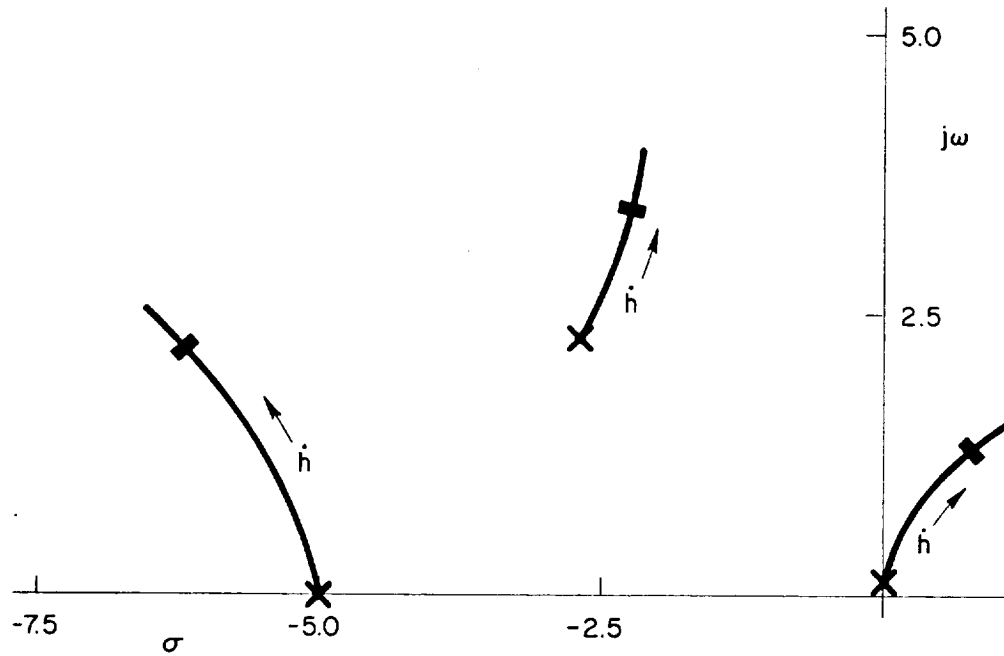
Figure A-3. ḣ Root Locus With Datametrics Pressure Sensor, 3,350 ft, 110 kts (Reproduction of Figure 18, Reference 1)
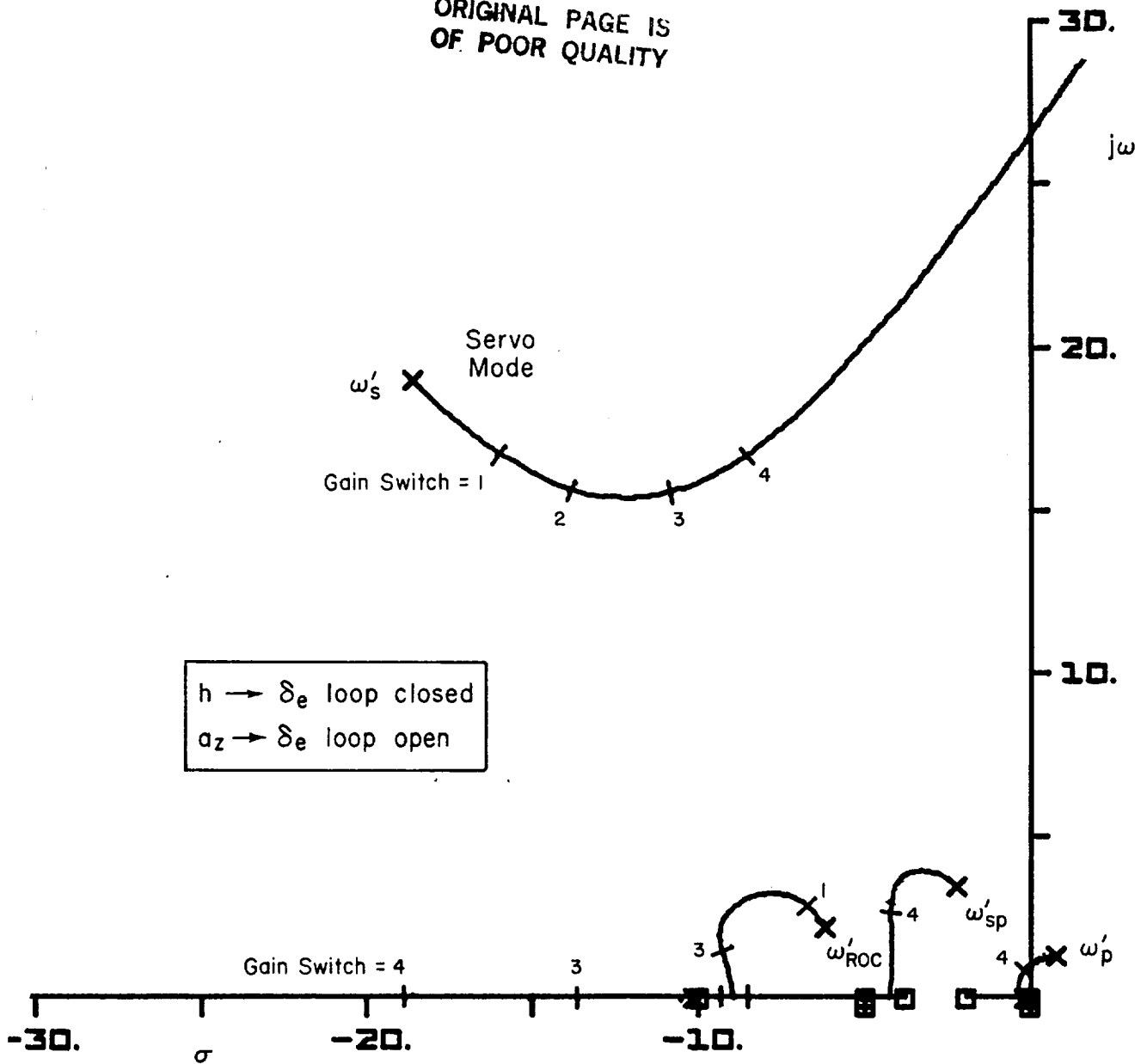
Figure A-4. Closure of $q \rightarrow \delta_e$ Loops (110 kts)
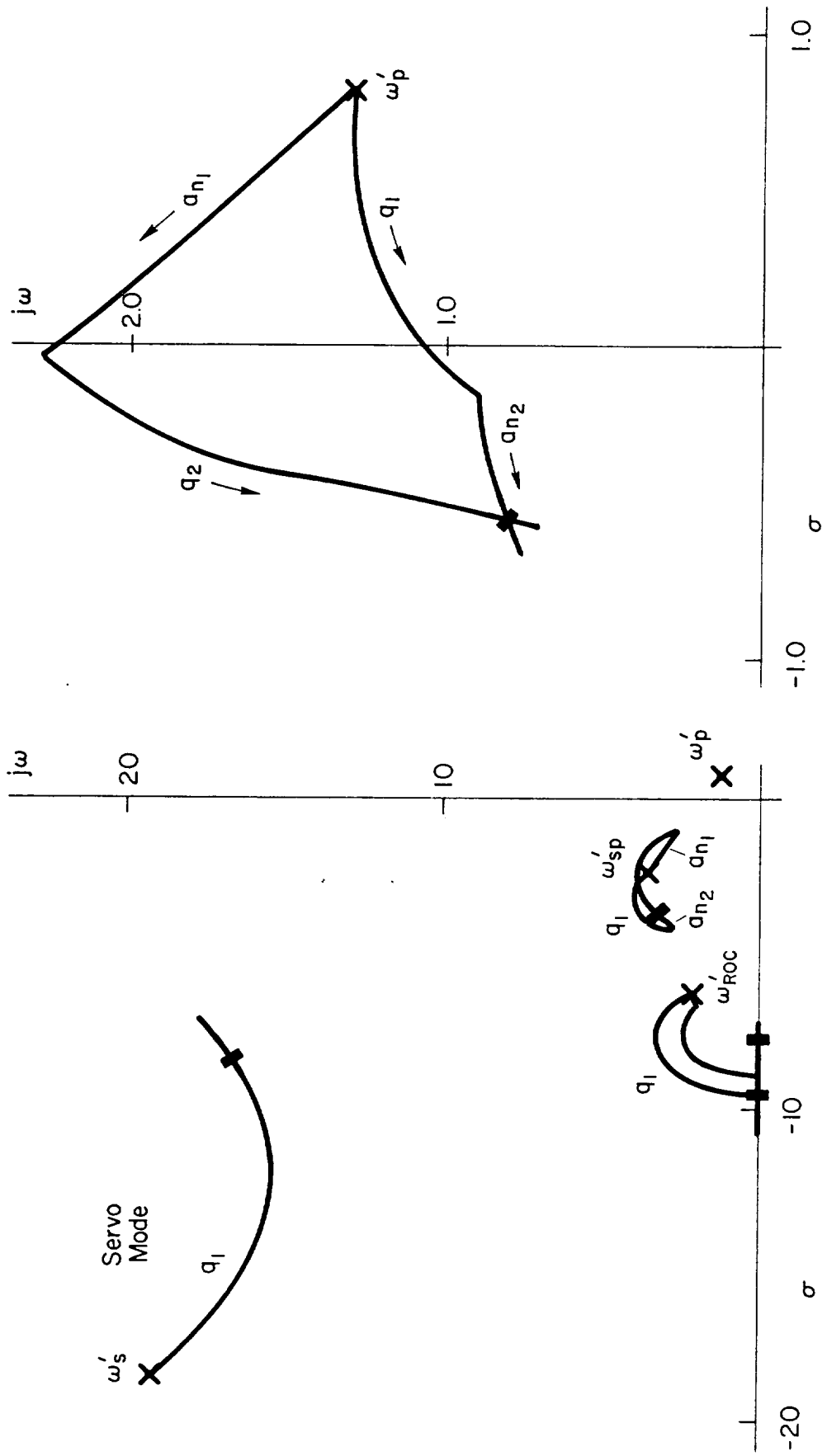
Figure A-5. q and a_n Root Locus With Datametrics Pressure Sensor, 3,350 ft, 110 kts, c Gains, Run 23 (Reproduction of Figure 21, Reference 1)
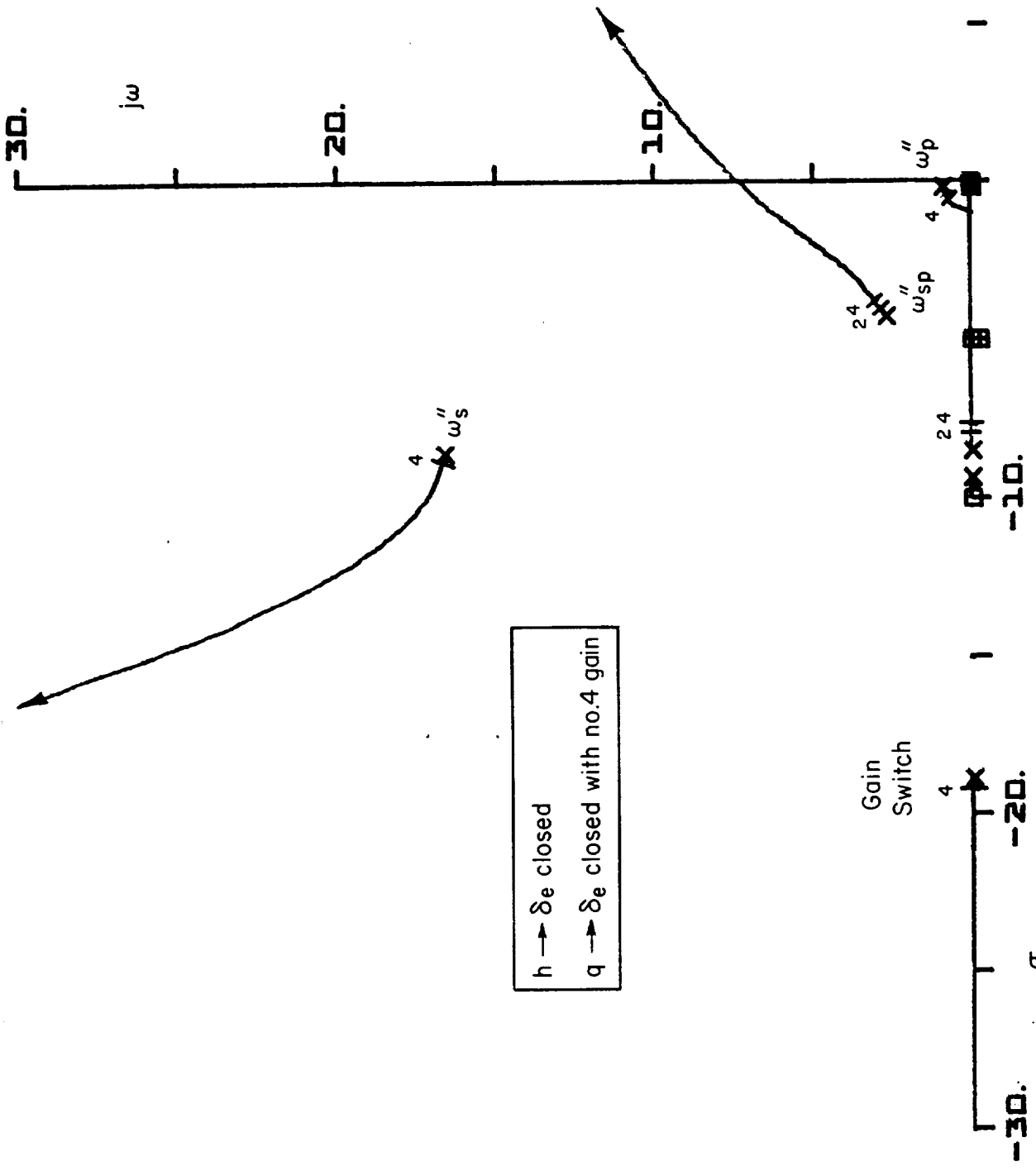
Figure A-6. Closure of $a_z \rightarrow \delta$ Loop (110 kts)
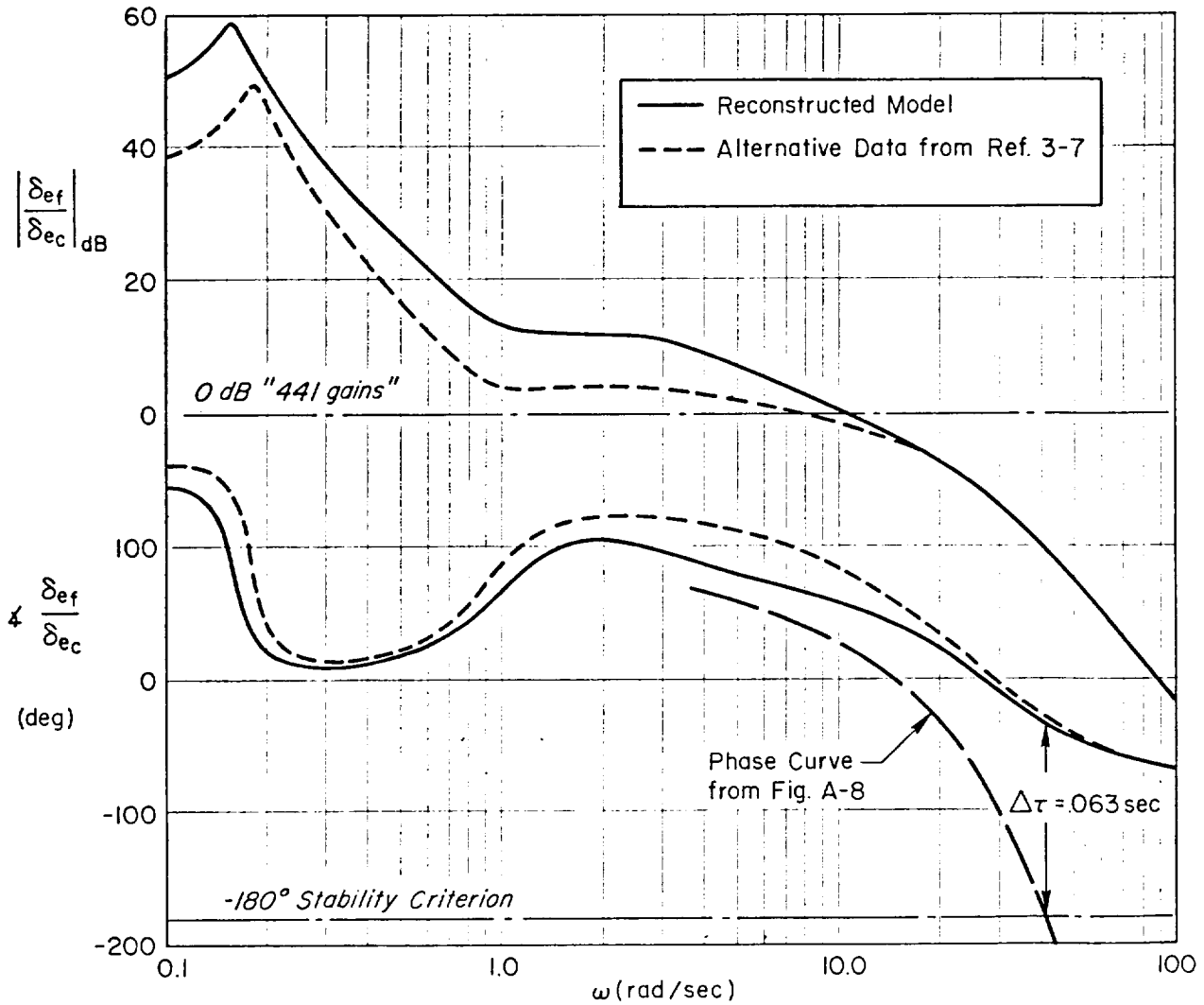
Figure A-7. Open Loop δ_{ef}/δ_{ec} Frequency Response Comparison
(Table A-6, '441' Gains, 110 kts)
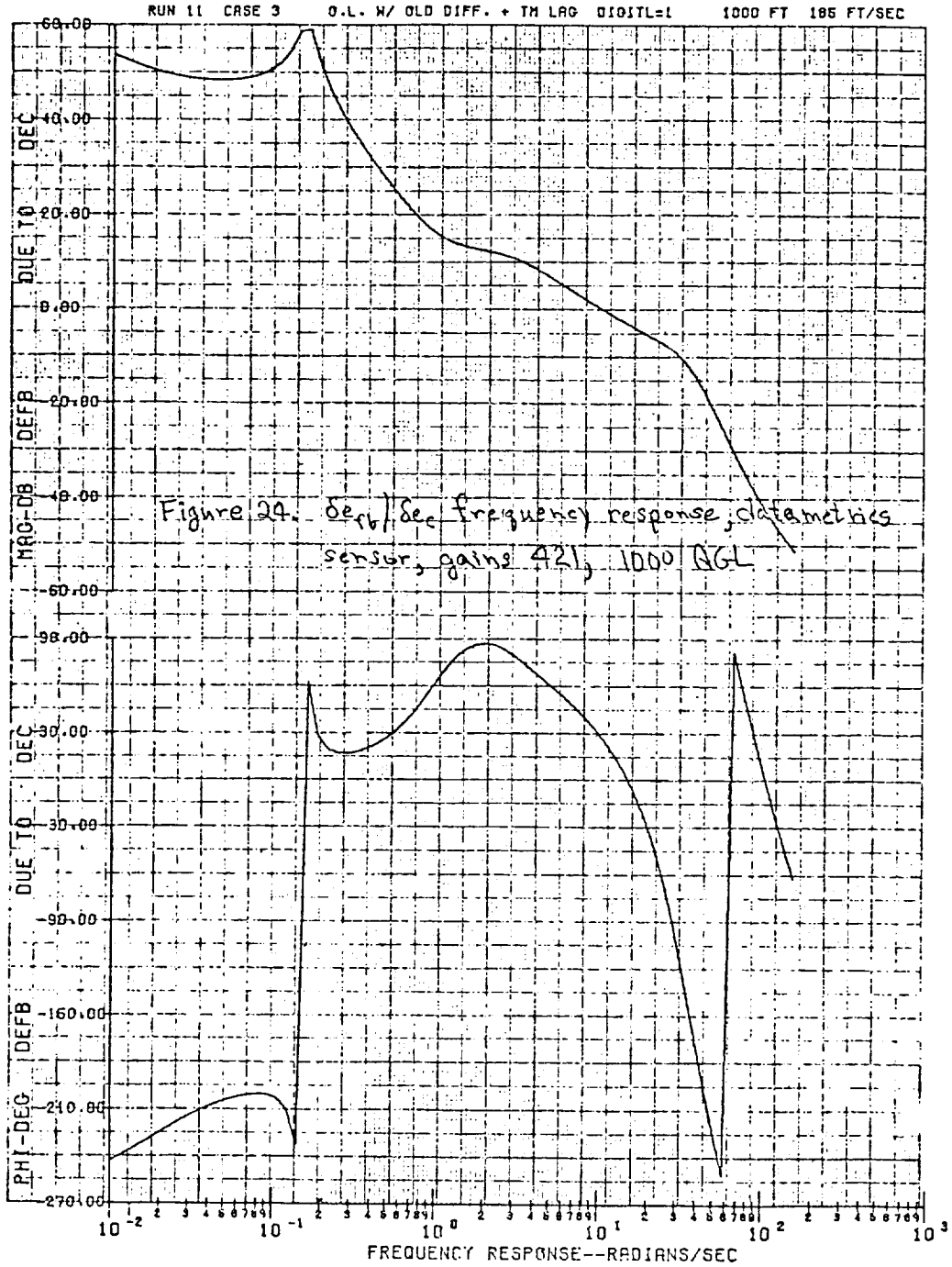
Figure A-8. Reproduction of Figure 24, Reference 1
(110 kts)

REFERENCES

A-1. Internal memo from John W. Edwards to HIMAT Project Office, Summary of Flight Tests and Analysis of the HIMAT BCS Approach and Landing System Using the PA-30 Airplane, Dryden Flight Research Center, NASA, 22 Nov. 1978.

A-2. "Autonomous RPRV Navigation, Guidance and Control Study," NASA Contract No. NAS4-2896 with Systems Technology, Inc., 1 Sept. 1981.

A-3. Lanman, Maurice H., III, An Investigation of Microwave Landing Guidance System Signal Requirements for Conventionally Equipped Civilian Aircraft, DOT-TSC-FAA-71-24, June 1971.

A-4. Albrecht, W., Operations Fact Sheet, OFS 808-77-1, PA-30 Airplane, Serial No. N-808NA, Dryden Flight Research Center, 20 Sept. 1977.

A-5. Barber, M. R., Data for the Six Degree of Freedom Simulation of the PA-30 Aircraft, 20 Dec. 1968.

A-6. Fink, Marvin P. and Delma C. Freeman, Jr., Full-Scale Wind-Tunnel Investigation of Static Longitudinal and Lateral Characteristics of a Light Twin-Engine Airplane, NASA TN D-4983, Jan. 1969.

A-7. Wolowicz, Chester H. and Roxanah B. Yancey, Longitudinal Aerodynamic Characteristics of Light, Twin-Engine, Propeller-Driven Airplanes, NASA TN D-6800, June 1972.

A-8. McRuer, Duane, Irving Ashkenas, and Dunstan Graham, Aircraft Dynamics and Automatic Control, Princeton University Press, 1973.

A-9. Gera, Joseph, "HIMAT-BCS Validation During Approach and Landing Using the PA-30 Airplane-Program Plan," NASA Dryden Flight Research Center HIMAT Internal Document H-78-009, Apr. 1978.
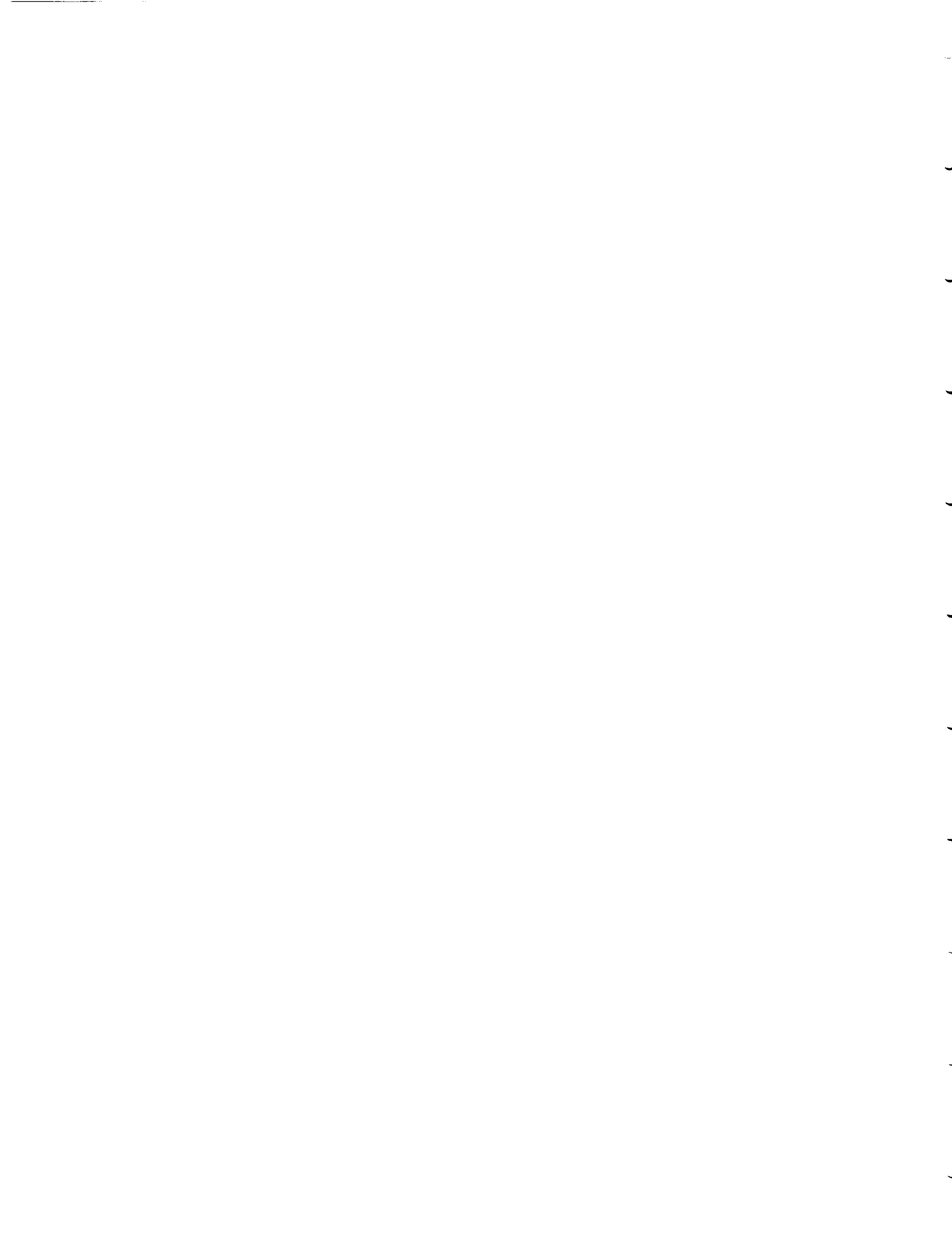
APPENDIX B

PA30/BCS AUTO THROTTLE ANALYSIS

1. Auto Throttle Mechanization for the PA-30 System

A complete analysis of the existing PA-30 auto throttle mechanization could not be made because of uncertainties regarding throttle deflection units and the throttle effectiveness derivative, $X_{\delta T}$. This situation produced an uncertainty in the overall loop gain for the auto throttle. Further, there was no linear auto throttle analysis in Ref. B-1, such as for the elevator loops, which could be used to resolve these questions. However, some approximate analysis has been done to understand the gross effects and to approximate auto throttle behavior sufficiently for use in analysis of the more important elevator loops. The auto throttle as shown in Fig. B-1 is basically an airspeed command system consisting of a $U \rightarrow \delta_T$ feedback and an airspeed command, U_c, scheduled with radar altitude. The airspeed schedule presently used is

$$U_c = \begin{cases} \begin{array}{l} 74.4 + 0.0375 \ h_R \ \text{kts} \\ (125.7 + 0.0634 \ h_R \ \text{fps}) \end{array} \Big\} \ \text{Decel region} \\ \begin{array}{l} 80.0 \ \text{kts} \quad \cdot \\ (135.2 \ \text{fps}) \end{array} \Big\} \ \text{Flare} \end{cases} \qquad (B-1)$$

It may be seen that the auto throttle is a pure airspeed to throttle loop in the flare mode, but in the decel region there is in addition an effective radar altitude-to-throttle feedback. This additional feedback will be considered briefly to demonstrate that its effect on the airspeed _dynamics_ is negligible and that it may be treated purely as a quasi-static airspeed command.

For small perturbations about any (quasi-static) reference speed, the auto throttle dynamics may be linearized. If we consider the
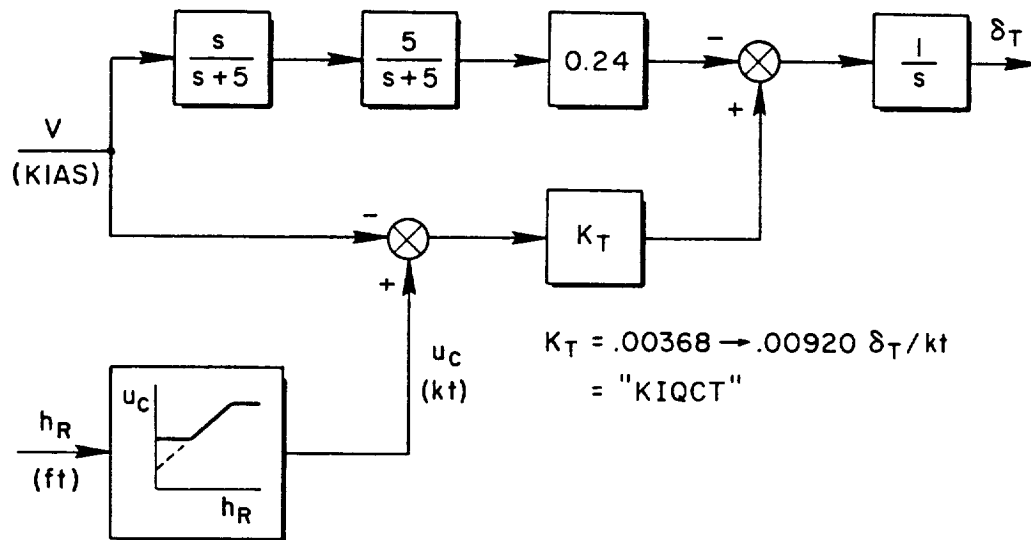
Figure B-1. PA-30/BCS Auto Throttle

closure of a throttle loop first before closure of the elevator loops,
it may be shown (Ref. B-2) that the throttle feedbacks modify the eleva-
tor and gust transfer function denominators and numerators.

2. Auto Throttle Effect on System Dynamics

As indicated in Eq. B-2

$$\frac{x}{\delta}\bigg|_{u,h_R \to \delta_T} = \frac{N_\delta^x + G_u^{\delta_T} N_\delta^x \frac{u}{\delta_T} + G_h^{\delta_T} N_\delta^x \frac{h}{\delta_T}}{\Delta + G_u^{\delta_T} N_{\delta_T}^u + G_h^{\delta_T} N_{\delta_T}^h} \qquad (B-2)$$

where

$$x = u, \theta, \alpha, \text{etc.}$$

$$\delta = \delta_e, u_g, w_g, \text{etc.}$$

From Eq. B-1 and Fig. B-1

$$G_h^{\delta T} = \begin{cases} \dfrac{-0.0375 \ K_T}{s} & \text{Decel region} \\[4mm] 0.0 & \text{Flare} \end{cases} \qquad \delta_T \ \text{unit/ft}$$

(B-3)

$$G_u^{\delta T} = \dfrac{-1}{s} \left\{ \dfrac{-0.24 \cdot 5s}{(s + 5)^2} - K_t \right\}$$

$$= \dfrac{1.2s + K_T(s + 5)^2}{s(s + 5)^2} \qquad \delta_T \ \text{unit/kt}$$

(B-4)

The above feedback transfer functions are written for negative feedback consistent with Eq. B-2. In addition to the uncertainty in the overall auto throttle loop gain, there is some uncertainty in the value of K_T in Fig. B-1 (denoted as "KIQCT" in the NASA DFRF documentation). In Ref. B-1

$$K_T = \text{"KIQCT"} = 0.00218 + 0.00545 \ \dfrac{\delta_T \text{unit}}{\text{kt}}$$

(A-5a)

In Ref. B-3

$$K_T = \text{"KIQCT"} = 0.00368 + 0.00920 \ \dfrac{\delta_T \ \text{unit}}{\text{kt}}$$

(A-5b)

However, for purposes of approximate analyses, we may assume that K_T is on the order of 10^{-3}.

3. Nature of the $G_u^{\delta_T}$ Numerator

The numerator of the $U \rightarrow \delta_T$ feedback transfer function in Eq. B-4 will be a quadratic with real roots. The nature of the roots, as a function of K_T may be seen in the system survey sketched in Fig. B-2. This indicates that for $K_T \doteq 10^{-3}$, there is one large root greater than 10^2 rad/sec and the small root which to an asymptotic approximation is 20.8 K_T rad/sec. Thus, from Fig. B-2 and Eq. B-4

$$G_u^{\delta_T} = \frac{K_T(1/T_1')(1/T_2')}{(0)(5)^2}$$

$$\doteq \frac{K_T(20.8K_T)(1.2/K_T)}{(0)(5)^2} \frac{\delta_T \text{ unit}}{kt} \tag{B-6}$$

a) Bode Root Locus   b) Conventional Root Locus
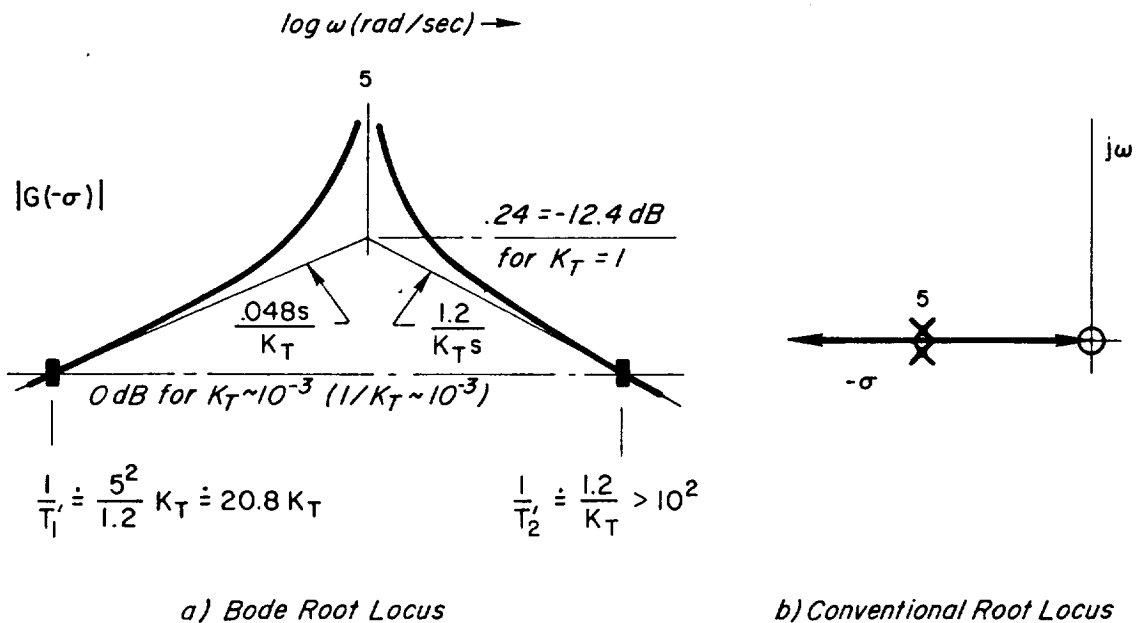
Figure B-2. System Survey Sketch for the $G_u^{\delta_T}$ Numerator

For the frequency region of interest which is well below the high frequency zero,

$$G_u^{\delta_T} \doteq \frac{1.2(20.8\ K_T)}{(0)(5)^2} \frac{\delta_T\ \text{unit}}{kt} \qquad (B-7)$$

which has an amplitude frequency response as sketched in Fig. B-3. It should be noted that the asymptote between the two zeros is independent of K_T.
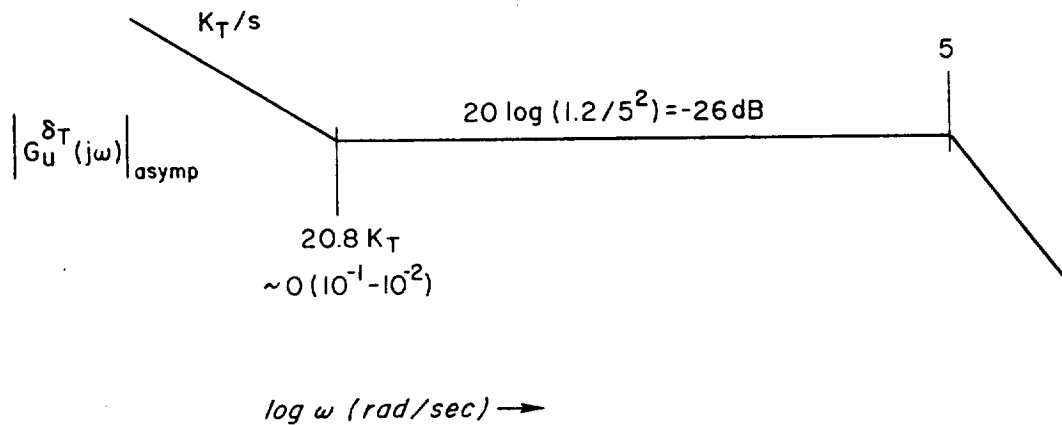

Figure B-3. Frequency Response Sketch of $G_u^{\delta_T}$ Amplitude

4. Relative Contribution of the Airspeed and Altitude Feedback Loops to Δ' in the Decel Region

From Eq. B-2 it may be seen that the relative contribution of the altitude and airspeed loops may be compared from the ratio

$$R_{uh} = \frac{G_h^{\delta_T}\ N_{\delta_T}^h}{G_u^{\delta_T}\ N_{\delta_T}^u} \qquad (B-8)$$

The contribution to the above ratio, which is dependent on the control system parameters is

$$\frac{G_h^{\delta T}}{G_u^{\delta T}} = \frac{-0.0375 K_T (5)^2}{K_T (20.8 K_T)(1.2/K_T)} \frac{kt}{ft} \qquad (B-9)$$

It may be seen from the asymptotic frequency response sketch in Fig. B-4 that this ratio will be much less than 1 at all frequencies, i.e., at least -28 db or less. The airframe numerator ratio in Eq. B-8 for the 110 kt case is

$$\frac{N_{\delta T}^h}{N_{\delta T}^u} = \frac{-0.000779(-0.0783)[0.0684,\ 13.62]/(0)}{0.00894/1.69(0.242)[0.742,\ 3.44]} \frac{ft}{kt} \qquad (B-10)$$
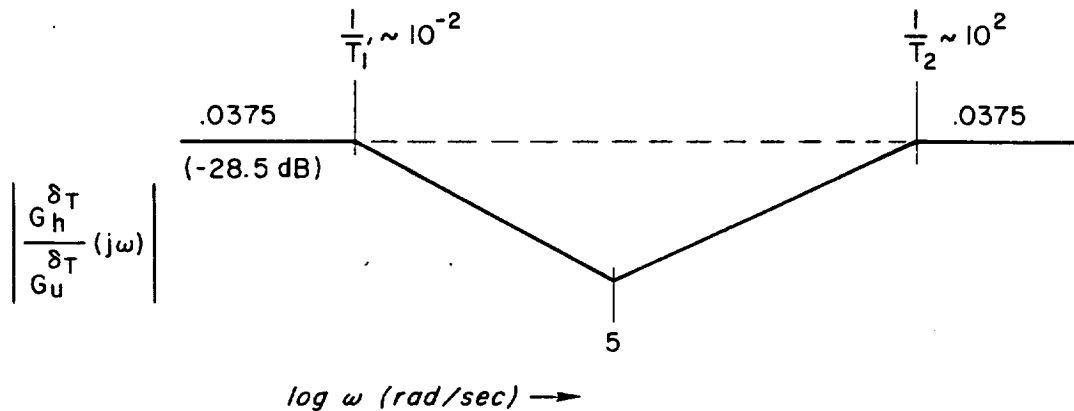
Figure B-4. Frequency Response Sketch of $\left| G_h^{\delta T}/G_u^{\delta T} \right|$

The sketch of the Eq. B-10 frequency response shown in Fig. B-5 indicates that the numerator ratio rolls off rapidly with increasing frequency and that the overall ratio given in Eq. B-8 will be on the order of 10^{-1} or less in the region of interest for vehicle dynamics, thus indicating that the $h \rightarrow \delta_T$ feedback is significant only at very low frequencies, i.e., the steady state. Thus, as indicated earlier, the $h \rightarrow \delta_T$

The figure shows a frequency response sketch with a slope labeled $\frac{.74}{s}$, frequency breakpoints at $\frac{1}{T_u}$, $\frac{1}{T_h}$, a level of 9.50 ($19.6\,dB$), and frequencies $\omega_u \doteq \omega_{sp}$ and $\omega_h \doteq \frac{-U_o Z_w}{\theta_o} \frac{M_{\delta_T}}{Z_{\delta_T}}$. The vertical axis is $\left|\frac{N^h_{\delta_T}}{N^u_{\delta_T}}(j\omega)\right|_{dB}$.
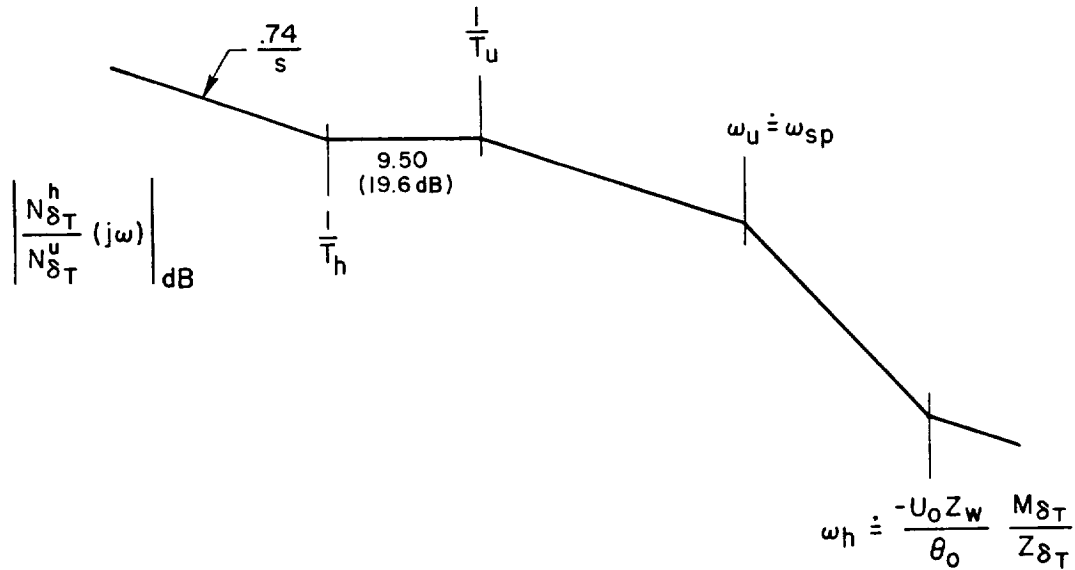
Figure B-5. Frequency Response Sketch of $\left|N^h_{\delta_T}/N^u_{\delta_T}\right|$

effect can be treated purely as a quasi-static variation in the airspeed command. Numerical surveys of the various coupling numerator ratios indicate that in an analogous manner the effect of the h feedback may generally be neglected on the numerators of Eq. B-2 — at least for the elevator transfer functions.

5. Approximate Augmented Denominator

From the preceding considerations, the effect of the auto throttle on the characteristic polynomial may be approximated as

$$\Delta' = \Delta|_{u,h \to \delta_T} \doteq \Delta|_{u \to \delta_T}$$

$$= \Delta + G^{\delta_T}_u N^u_{\delta_T}$$

$$= \Delta \left(1 + \frac{G^{\delta_T}_u N^u_{\delta_T}}{\Delta}\right) \tag{B-11}$$

There is some effect of the M_{δ_T} stability derivative (i.e., pitching moment due to throttle) which occurs as a consequence of thrust offset. This pitching moment contribution primarily effects the low frequency real root in the speed to throttle numerator. However, for an approximate analysis of the auto throttle closure, both the M_{δ_T} and the Z_{δ_T} effects may be neglected and thus

$$N^u_{\delta_T} \doteq X_{\delta_T}s\left[s^2 - \left(Z_w + M_q + M_{\dot\alpha}\right)s + (Z_wM_q - M_\alpha)\right]$$

$$\doteq X_{\delta_T}s\ \Delta_{sp} \tag{B-12}$$

Under these idealizations, the second order speed zero cancels the short period pole in the speed to throttle transfer function as seen in Eq. B-13

$$\frac{N^u_{\delta_T}}{\Delta} \doteq \frac{X_{\delta_T}s\Delta_{sp}}{\Delta_p \cdot \Delta_{sp}} = \frac{X_{\delta_T}s}{[\zeta_p,\omega_p]} \tag{B-13}$$

The phugoid mode is thus ideally the speed response mode.

Thus, the closure of the auto throttle loop may be seen from the system survey of Eq. B-14

$$\frac{G^{\delta_T}_u\ N^u_{\delta_T}}{\Delta} \doteq \frac{1.2(20.8K_T)}{(0)(5)^2} \cdot \frac{X_{\delta_T}(0)}{[\zeta_p,\omega_p]} \tag{B-14}$$

shown in Fig. B-6 as a Bode root locus. Figure B-6 shows that the low frequency zero of the airspeed-to-throttle equalization (Fig. B-2) is positioned near the phugoid to produce a "K/s region" above the phugoid out to $\dot\omega$ = 5 rad/sec. The auto throttle crossover frequency cannot be determined, of course, because of the uncertainty in loop gain noted previously. However, Fig. B-6 indicates that good auto throttle performance could be achieved with closures in the K/s region. Assuming
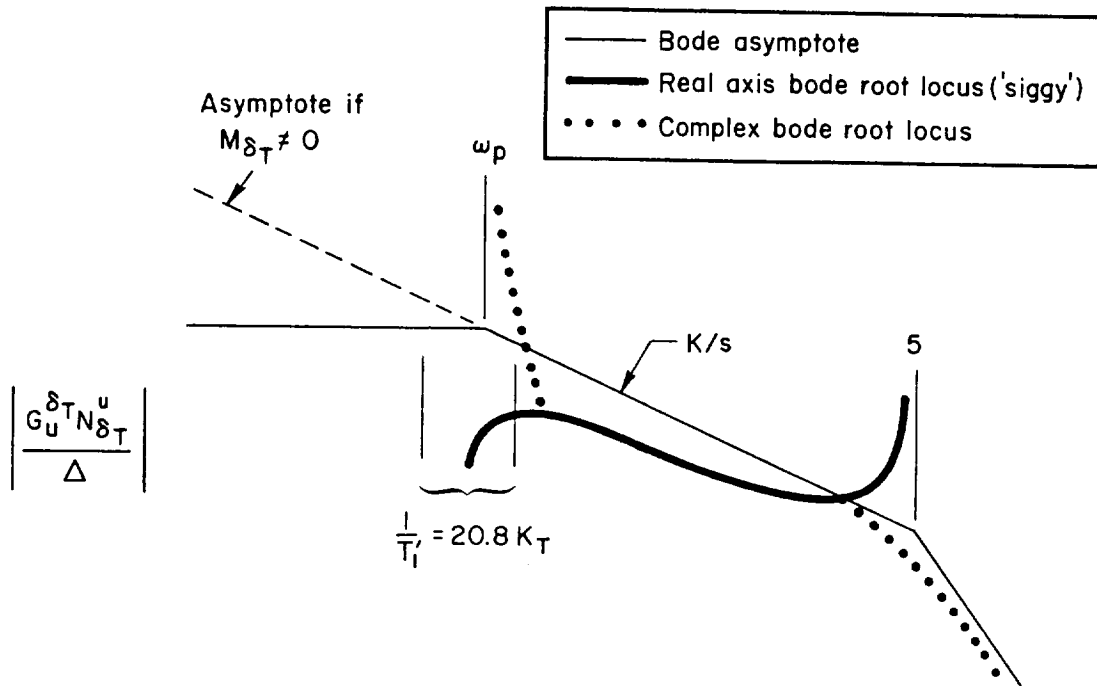
Figure B-6. Bode Root Locus Sketch of the Auto Throttle Closure

that the auto throttle does have a reasonable gain, then it is reasonable to consider its effect as an ideal airspeed constraint in the speed response (phugoid) region. Assumption of a pure speed constraint leads, of course, to the short period model, Ref. B-2 for the airframe dynamics. Thus, even if the auto throttle bandwidth is lower than the short period mode frequency, the short period equations of motion should provide an adequate auto throttle model for analyses of the elevator feedback loops.

REFERENCES

B-1. Internal memo from John W. Edwards to HIMAT Project Office, Summary of Flight Tests and Analysis of the HIMAT BCS Approach and Landing System Using the PA-30 Airplane, Dryden Flight Research Center, NASA, 22 Nov. 1978.

B-2. McRuer, Duane, Irving Ashkenas, and Dunstan Graham, _Aircraft Dynamics and Automatic Control_, Princeton University Press, 1973.

B-3. Gera, Joseph, "HIMAT-BCS Validation During Approach and Landing Using the PA-30 Airplane-Program Plan," NASA Dryden Flight Research Center HIMAT Internal Document H-78-009, Apr. 1978.

PA-30/BCS ELEVATOR FEEDBACK LOOP ANALYSIS

1. Short Period Model of the Airframe Dynamics

The auto throttle analysis, Appendix B indicates that even though the effective gain of the auto throttle (and hence the bandwidth) is unknown, it is reasonable to treat the auto throttle implicitly by use of the speed constrained, short period equations of motion for analysis of the elevator loop closures. The short period model, as given in Ref. C-1, pg. 637 is summarized below

Equations of Motion:

$$[s - Z_w]sd + Z_\alpha\theta = -Z_{\delta_e}\delta_e + Z_\eta\eta$$

$$(M_{\dot{w}}s + M_w)sd + [s^2 - (M_q + M_{\dot{\alpha}})s - M_\alpha]\theta = M_{\delta_e}\delta_e - M_\eta\eta \qquad \text{(C-1)}$$

Characteristic Function:

$$\Delta = s^2\{s^2 - (M_q + M_{\dot{\alpha}} + Z_w)s - (M_\alpha - Z_wM_q)\} = s^2\Delta_{sp} \qquad \text{(C-2)}$$

Numerator

$$N_\delta^d = -Z_\delta[s^2 - (M_q + M_{\dot{\alpha}})s - (M_\alpha - \frac{M_\delta}{Z_\delta}Z_\alpha)]$$

$$N_\eta^d = Z_\eta[s^2 - (M_q + M_\alpha)s - (M_\alpha - \frac{M_\eta}{Z_\eta}Z_\alpha)]$$

$$N_\delta^\theta = s\{(M_\delta + Z_\delta M_{\dot{w}})s - (M_\delta Z_w - Z_\delta M_w)\}$$

$$N_\eta^\theta = -s\{(M_\eta + Z_\eta M_{\dot{w}})s - (M_\eta Z_w - Z_\eta M_w)\} \qquad \text{(C-3)}$$

2. BCS Path Control System — PA-30

The BCS elevator feedback loop structure as presently implemented on the PA-30 is shown in Fig. A-1 and consists of feedbacks of pitch rate from a pitch gyro, acceleration from an accelerometer, altitude rate from a barometric rate of climb sensor and altitude from a radar altimeter. A linear analysis of this control system without speed constraint, i.e., neglecting the auto throttle was given in Ref. C-2 and that analysis is reviewed in Appendix A. The elevator loops will be briefly analyzed in this section with the auto throttle effect included implicitly through the short period model. This analysis will provide some perspective for the proposed system to be discussed in Appendix D.

3. Pitch Rate to Elevator Closure

The control law for the overall pitch rate to elevator feedback is

$$\delta_e = \left\{ \frac{K_{\bar{q}}s}{(s + 1/T_{wo})} \cdot \frac{q}{s} + K_q q \right\} G_s(s) \qquad (C-4)$$

where

$$K_q = KQAL$$

$$K_{\bar{q}} = KIQ$$

$$G_s(s) = \text{servoactuator transfer function}$$

Thus, as the effective feedback transfer function is

$$G_q^{\delta_e} = -\frac{K_q(s + 1/T_E)}{(s + 1/T_{wo})} G_s(s) \qquad (C-5)$$

where

$$\frac{1}{T_E} = \frac{1}{T_{wo}} + \frac{K_{\dot{q}}}{K_q}$$

The minus sign in Eq. C-5 is consistent with the assumption of negative feedback. For the BCS system as implemented on the PA-30

$$\frac{1}{T_{wo}} = 0.125 \text{ rad/sec}$$

$$\frac{K_{\dot{q}}}{K_q} = 3.70 \text{ rad/sec}$$

$$\frac{1}{T_E} = 3.83 \doteq \frac{K_{\dot{q}}}{K_q} \text{ rad/sec}$$

$$G_s(s) \doteq \frac{1}{18s + 1}$$

The closure of the pitch rate loop is shown in the system surveys of Fig. C-1 for 80 and 110 kts. The Bode root loci (4) shown as dots in Figs. C-1a and C-1b indicate the variation of the closed loop short period root with gain. Likewise the σ root loci labeled (1) through (3) in Figs. C-1a and C-1b show the variation of the closed loop real roots with gain. The roots for a given loop gain are indicated by the intersection of the appropriate 0 dB line with the Bode loci. The roots corresponding to the gain K_q = 0.25 rad/sec, are shown in Fig. C-1. The Bode loci in Figs. C-1a and C-1b may be correlated with the conventional root loci shown in the generic sketch of Fig. C-1.
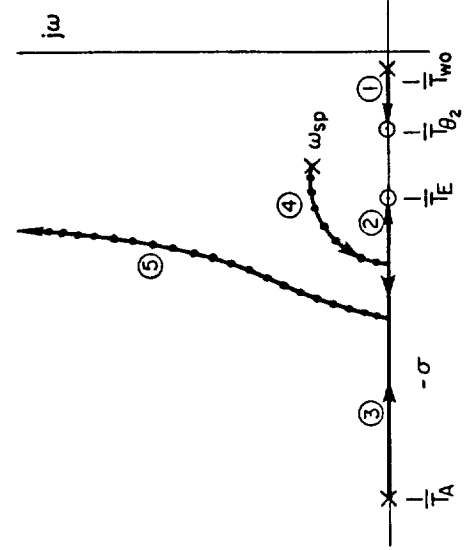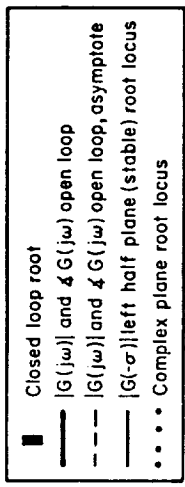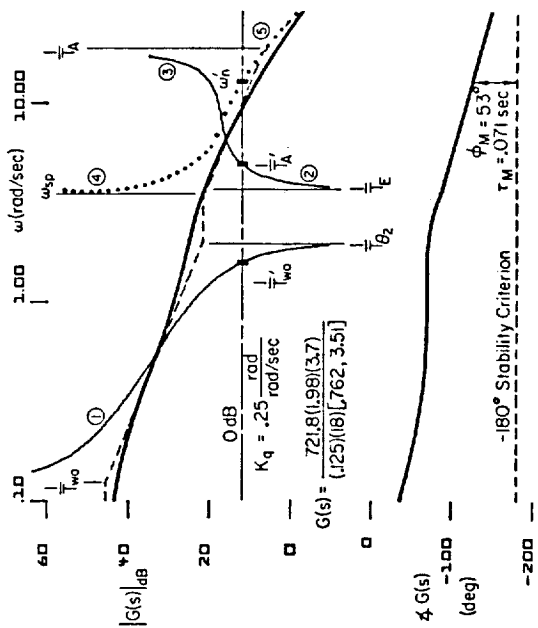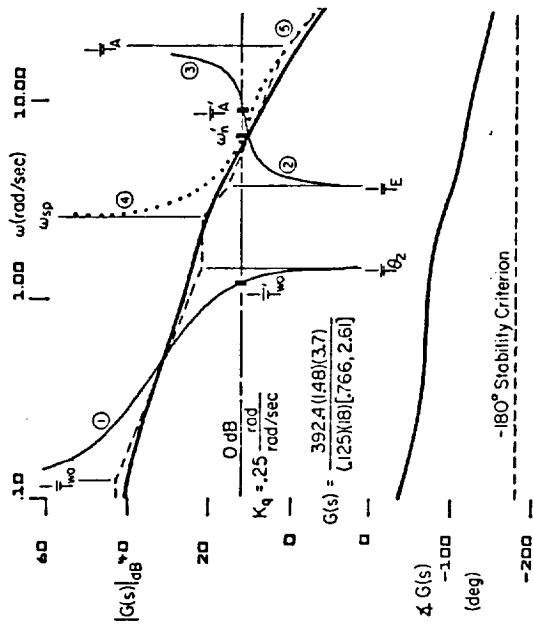
Figure C-1. System Survey of $q \rightarrow \delta_e$ Closure

The nature of the closed loop pitch rate dynamics is determined by the gain K_q or, equivalently, the crossover frequency ω_{ca} which is the frequency at which the 0 dB line for the chosen gain K_q intercepts the Bode asymptote. It may be seen that, for the given values of the parameters $1/T_{wo}$ and $1/T_E$, the closure can be made in a K/s region which implies adequate phase margin and adequate low frequency gain margins. Thus, even though the short period and servo modes are highly coupled (especially at 110 kts) the closed loop characteristics should be acceptable – unless there is additional significant loss in phase margin due to time delays resulting from use of the ground computer. The characteristic equation with the pitch rate loop closed (and with implicit closure of the auto throttle) is .

$$\Delta' = \Delta \Big|_{\substack{q \to \delta_e \\ u \to \delta_T}}$$

$$= s^2 \Delta_{sp} - \frac{K_q (1/T_E)}{(1/T_{wo})} \cdot \frac{1/T_A}{(1/T_A)} \cdot M_{\delta_e} s^2 (1/T_{\theta_2})$$

$$= s^2 \frac{(1/T'_{wo})(1/T'_A)[\zeta', \omega'_n]}{(1/T_{wo})(1/T_A)} \tag{C-6}$$

It is of interest to consider the nature of the pitch rate response to inputs at the last summer before the servo. Inputs at this point may be considered to be pitch rate commands as denoted by $'q'_c$ in Fig. A-1. Thus, the pitch rate feedbacks form a 'pitch rate command system' with respect to q_c with the closed loop transfer function

$$\frac{q}{q_c}\bigg|_{q \to \delta_e} = \frac{q'}{q_c} = \frac{-\left(\frac{1}{T_A s + 1}\right) N_{\delta_e}^q}{\Delta'}$$

$$= \frac{-M_{\delta_e}\left(1/T_{\theta_2}\right) \frac{1/T_A}{\left(1/T_A\right)}\left(1/T_{wo}\right)\left(1/T_A\right)}{\left(1/T_{wo}'\right)\left(1/T_A'\right)\left[\zeta', \omega_n\right]} \qquad \text{(C-7)}$$

It may be seen from Figs. C-1a and C-1b that the pole resulting from the washout time constant will essentially be driven into the attitude numerator $1/T_{\theta_2}$ at the nominal pitch rate closure. Thus

$$\frac{q'}{q_c} \doteq \frac{-M_{\delta_e}\left(1/T_{wo}\right)}{\left[\zeta', \omega_n'\right]} \cdot \frac{1/T_A}{\left(1/T_A'\right)} \qquad \text{(C-8)}$$

indicating that the pitch rate response to pitch rate command will be analogous to the open loop pitch rate response to elevator-command except that the attitude zero in Eq. C-8 is set by the washout time constant instead of the conventional value $1/T_{\theta_2}$.

4. $a_z \to \delta_e$ CLOSURE

From Fig. A-1, the a_z to elevator feedback transfer function is (negative feedback)

$$G_{a_{z_a}}^{\delta_{e_c}} = \frac{K_{a_z}}{s} \qquad \text{(C-9)}$$

where

$$K_{a_z} = KINZ(37.2/57.3)$$

The location of the accelerometer on the PA-30 was not specified in the available documentation, however, the analysis in Ref. C-2 is consistent with the fact that the accelerometer is near the instantaneous center of

rotation for elevator inputs (ICR). Under this assumption and the further assumption that the elevator effectiveness in lift, Z_{δ_e} may be neglected (so that the ICR is near the c.g.), then the accelerometer output response to elevator inputs for the speed constrained condition is given by Eq. C-10.

$$\frac{a_{z_a}}{\delta_e} \rightarrow \frac{N_{\delta_e}^{a_z}{}_{\delta_T}^{u}}{N_{\delta_T}^{u}} = \frac{s^2 N_{\delta_e}^{d}{}_{\delta_T}^{u}}{N_{\delta_T}^{u}}$$

$$= \frac{U_o Z_w X_{\delta_T} M_{\delta_e} s}{X_{\delta_T} s \Delta_{sp}} = \frac{U_o Z_w M_{\delta_e}}{\Delta sp} \qquad (C-10)$$

The effect of the accelerometer feedback on the characteristic equation with the pitch rate-to-elevator and auto throttle loops closed may be seen from a system survey of

$$G(s) = \frac{G_{a_z}^{\delta_e} N_{\delta_e}^{a_z}}{\Delta'}$$

$$= \frac{K_{a_z} U_o Z_w M_{\delta_e} (1/T_{wo})(1/T_A)}{(0)(1/T_{wo}')(1/T_A')[\zeta', \omega_n']} \qquad (C-11)$$

as sketched in Fig. C-2. The values of the accelerometer gain K_{a_z} derived from Ref. C-2 are

$$K_{a_z} = 0.0768 \rightarrow 0.1919 \text{ deg/g}$$

$$= 4.16 \cdot 10^{-5} \rightarrow 1.04 \cdot 10^{-4} \text{ rad/ft/sec}^2$$
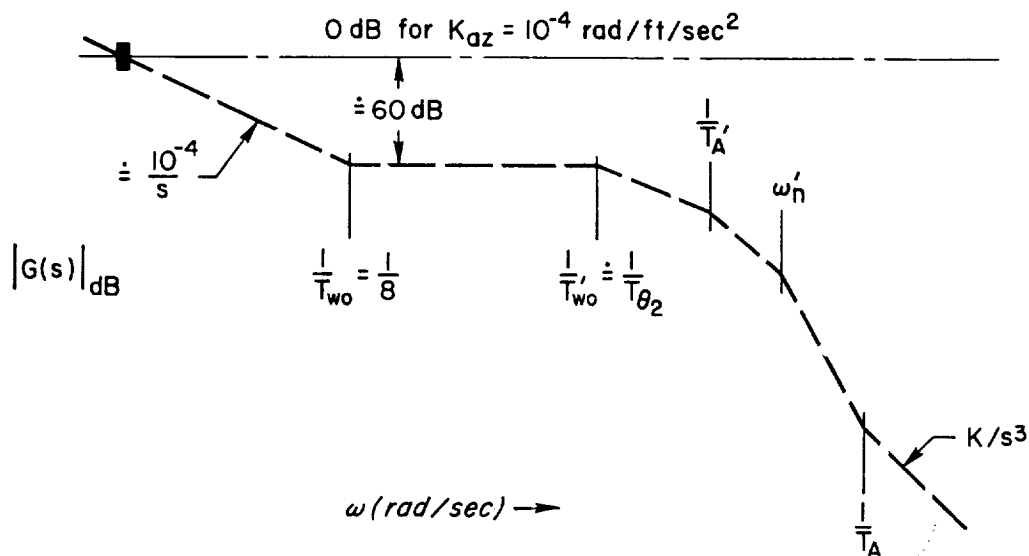
Figure C-2. Asymptote Sketch of the Bode Root Locus for the
Closure of the $a_z \rightarrow \delta_e$ Loop ($q \rightarrow \delta_e$ Closed) for
the Existing System

As shown in Fig. C-2, this is a very low value of accelerometer gain and thus this loop will have a negligible effect on the aircraft dynamics. This fact was also noted in the review of the linear analysis of Ref. C-2 given in App. A. Consequently, the effect of the accelerometer feedback will be neglected for in the following analysis.

5. SINK RATE TO ELEVATOR CLOSURE

With the pitch rate loop closed and the accelerometer feedback neglected, the open loop transfer function for the $\dot{h}$ loop is

$$\left.\frac{\dot{h}}{\dot{h}_3}\right|_{q \rightarrow \delta_e} = \frac{1}{s} \left.\frac{\dot{h}}{q} \frac{q}{q_c}\right|_{q \rightarrow \delta_e} \tag{C-12}$$

For the short period equations of motion, the $\dot{h}$ response to pitch rate is given by

$$\frac{\dot{h}}{q} \doteq \frac{U_O \gamma}{s\theta} \doteq \frac{U_O}{s(T_{\theta_2}s + 1)}$$

where

$$T_{\theta_2} \doteq \left(-Z_w + M_w \frac{Z_{\delta_e}}{M_{\delta_e}}\right)^{-1} \doteq (-Z_w)^{-1} \qquad \text{(C-13)}$$

Thus, Eq. C-12 becomes

$$\left.\frac{\dot{h}}{\dot{h}_3}\right|_{q \to \delta_e} \doteq \frac{U_O Z_w M_{\delta_e}(1/T_{wo})}{s^2(1/T_{\theta_2})[\zeta', \omega_n']} \cdot \frac{1/T_A}{(1/T_A')} \qquad \text{(C-14)}$$

and a system survey of this closure is sketched in Fig. C-3. For the crossover region defined by the nominal $\dot{h}$ gain at $U_O = 110$ kts

$$K_{\dot{h}} \left.\frac{\dot{h}}{\dot{h}_3}\right|_{q \to \delta_e} \doteq \frac{137 K_{\dot{h}}}{s} \qquad \text{(C-15)}$$

for

$$K_{\dot{h}} = 0.275 \text{ deg/fps} = 4.8(10^{-3}) \text{ rad/fps}$$

The sink rate loop closure is made in the K/s region between the washout inverse time constant, $1/T_{wo}$, and the airframe attitude zero, $1/T_{\theta_2}$. The asymptotic crossover frequency ω_{ca} is thus $137 K_{\dot{h}} = 0.66$ rad/sec which will be the approximate bandwidth of the sink rate loop closure.

Closed loop root

— — $|G(j\omega)|$ and $\sphericalangle G(j\omega)$ open loop, asymptote

$|G(-\sigma)|$ left half plane (stable) root locus

• • • • Complex plane root locus

a) Bode Root Locus

b) Conventional Root Locus
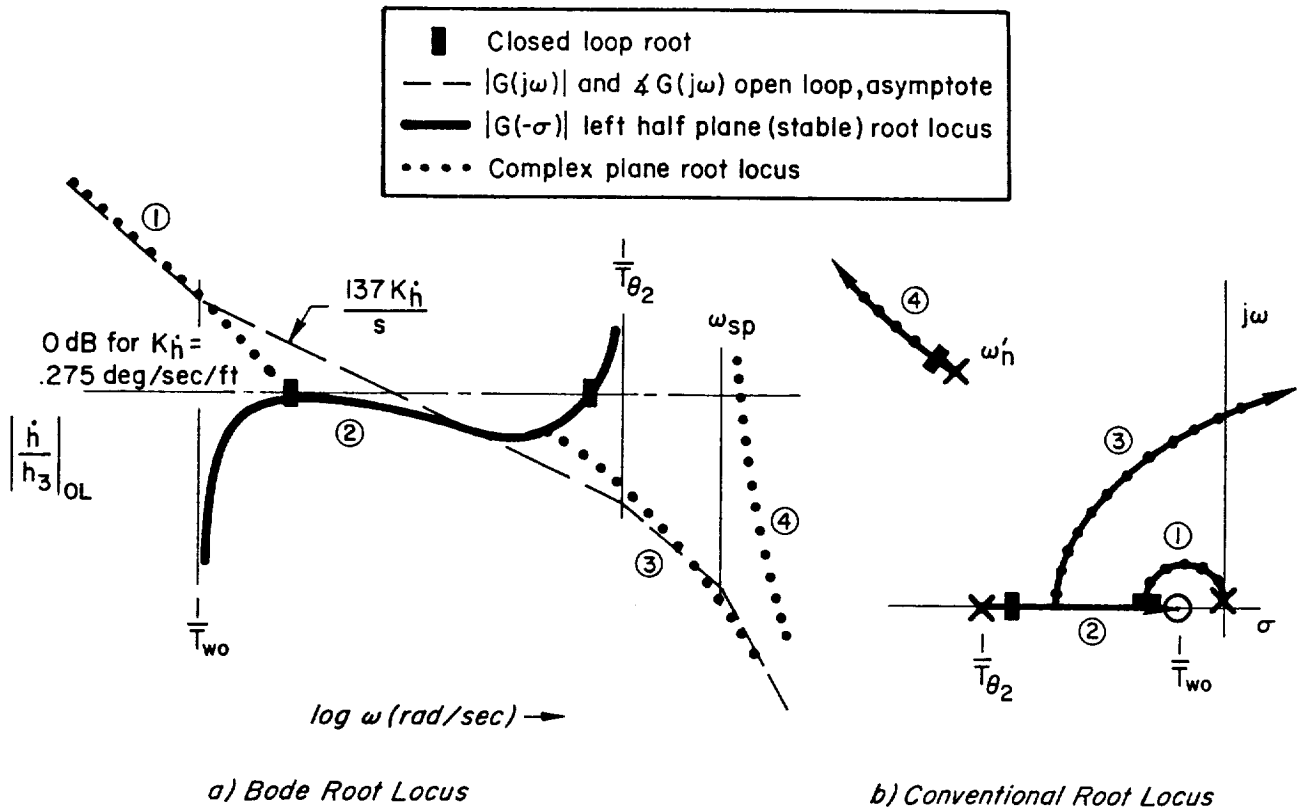
Figure C-3. System Survey of the $\dot{h} \rightarrow \delta_e$ Closure
($q \rightarrow \delta_e$ Closed) for the Existing System

It should be noted for comparison with the proposed system to be discussed later that achieving a good sink rate loop closure requires that $1/T_{wo} \ll 1/T_{\theta_2}$, a situation which will be different in the proposed system. When comparing this closure to that in App. A, it should be noted that the situation here is somewhat different because the significant attitude lags of the rate-of-climb sensor have been neglected and the speed constraint has effectively removed the phugoid mode.

6. SERVO MODE STABILITY

Reference C-2 indicated that problems with limit cycle oscillations in the elevator were encountered in the PA-30 flight test of the BCS system. The analysis in App. A also indicates the sensitivity of the relative stability of the servo mode to changes in system parameters. Thus, a brief analysis of the servo mode will be presented here to

identify the primary contributors to low damping ratio. For this analysis, a more complete servo model than the first order model used previously is required and the second order model given in Ref. C-2 as

$$G_S(s) = \frac{\delta_e}{\delta_{e_c}} = \frac{\omega_s^2}{[\zeta_s, \omega_s]} \qquad \text{(C-16)}$$

$$= \frac{26.6^2}{[0.70, \ 26.6]}$$

will be used. Since the pitch rate loop is the 'tightest' loop, it would be expected to be the primary cause of low servo mode damping ratio. This assumption may be tested by considering the expression for the characteristic polynomial with the pitch rate loop closed

$$\Delta' = s^2 \Delta_{sp} - \frac{K_q (1/T_E)}{(1/T_{wo})} \cdot \frac{\omega_s^2}{[\zeta_s, \omega_s]} \cdot M_{\delta_e} \ (1/T_{\theta_2}) s^2 \qquad \text{(C-17)}$$

Equation C-17 is equivalent to the expression in Eq. C-6 except for the use of second order servo model. At high frequencies near the servo mode, Eq. C-17 may be approximated as

$$\Delta' \doteq s^4 - \frac{K_q \omega_s^2 M_{\delta_e} s^3}{[\zeta_s, \omega_s]}$$

$$= s^4 \left\{ 1 - \frac{0.25 \cdot 26.6^2 \cdot - 40.1}{(0)[0.70, \ 26.6]} \right\}$$

$$\doteq \frac{s^3 (19.60) \ [0.464, 19.0]}{[0.7, \ 26.6]}$$

for

$$K_q = 0.25 \text{ rad}/(\text{rad/sec}) \tag{C-18}$$

The closed loop servo poles given in Eq. C-18 check almost exactly with those given in Fig. A-4 of App. A which also includes the effect of the sink rate feedback closure with the ROL sensor lags. Thus, it may be seen that the effect of the pitch rate closure is dominant on the servo mode and that it can be expected that other lower bandwidth outer loops will not affect servo mode stability. The primary concern regarding servo mode stability will thus be effective time delays due to transmission of the $q \rightarrow \delta_e$ signal the airplane to ground computer and back to the airplane.

REFERENCES

C-1. McRuer, Duane, Irving Ashkenas, and Dunstan Graham, Aircraft Dynamics and Automatic Control, Princeton University Press, 1973.

C-2. Internal memo from John W. Edwards to HIMAT Project Office, Summary of Flight Tests and Analysis of the HIMAT BCS Approach and Landing System Using the PA-30 Airplane, Dryden Flight Research Center, NASA, 22 Nov. 1978.

APPENDIX D

ANALYSIS OF PROPOSED SYSTEM

1. Design Concept For Beam Follower

The basic design concept for the beam follower portion of the proposed autoland system makes use of the synthetic ILS beam derived from tracking radar data and presently used only as a pilot flight director display for manual landing. The approach taken here is to design a beam following system using conventional ILS system practice as presented in Ref. D-1 and D-2. For purposes of system analysis in the following sections, it will be assumed the present PA-30/BCS schedules for sinkrate and airspeed will be used with the further assumption that beam tracking will occur in the decel region from an altitude of 950 ft to 150 ft with airspeed steadily decreasing from 110 kts to 80 kts. Landing flare using the variable τ flare concept will be assumed to take place at a constant airspeed of 80 kts beginning at 150 ft altitude. These assumptions are made to make the analysis concrete and to allow comparison with the existing BCS autoflare system. However, it will be shown that the basic system design and system gains can be used with variations in the altitude and airspeed schedules and furthermore, that the airspeed and altitude schedules can be considered independent. The primary concern in this connection is the effect of variations in airspeed during beam tracking. While the deceleration should always be slow enough with respect to the vehicle dynamic time constants that quasi-constant coefficient dynamic models may be used for analyses, there is at least a potential problem in the large variations in the effective gain through large changes in the dynamic pressure, e.g.,

$$\frac{M_{\delta_e}\big|_{80 \text{ kts}}}{M_{\delta_e}\big|_{110 \text{ kts}}} \doteq \left(\frac{80}{110}\right)^2 = 0.53$$

However, it will be shown in the following analysis that one set of system gains will work satisfactorily over the 80 to 110 kt speed range.

A basic beam follower system concept is shown in Fig. D-1 and is the same as the Ref. D-2 design except that the pseudo-integral of pitch rate (from the pitch rate gyro) is used as a surrogate for pitch attitude, consistent with the mechanization of the existing PA-30/BCS system.

It should be noted that the pitch rate feedback structure shown in Fig. D-1 is identical in form to that used in the existing PA-30/BCS autoflare system (Fig. A-1). No explicit accelerometer feedback loop is shown in Fig. A-1 and this is essentially consistent with the existing PA-30/BCS system given the negligible effect of the $a_z \rightarrow \delta_e$ loop (see Appendix A analysis). It would, however, probably be desirable to combine the accelerometer and barometric rate-of-climb signals in a complementary filter to produce a baro-inertial sinkrate signal for the $\dot{h}$ feedback loop in Fig. D-1. The primary difference in the sinkrate loops between the existing PA-30/BCS autoland system and the proposed beam follower is then the removal of the forward loop integrator from the existing system.

2. Basic Design Considerations for Beam Follower

The structure of the beam follower system shown in Fig. D-1 follows from consideration of the basic guidance, control and regulation requirements for the system. These are stated in Ref. D-1 and D-2 and will be repeated here for convenience:

1) To establish and maintain the aircraft on a specified spatial pathway or beam, e.g. the instrument low approach system ILS glidepath.

2) To reduce flight path errors to zero in a stable, well damped and rapidly responding manner.

3) To establish an equilibrium flight condition.

4) To limit the speed or angle of attack excursions of this established equilibrium flight condition.
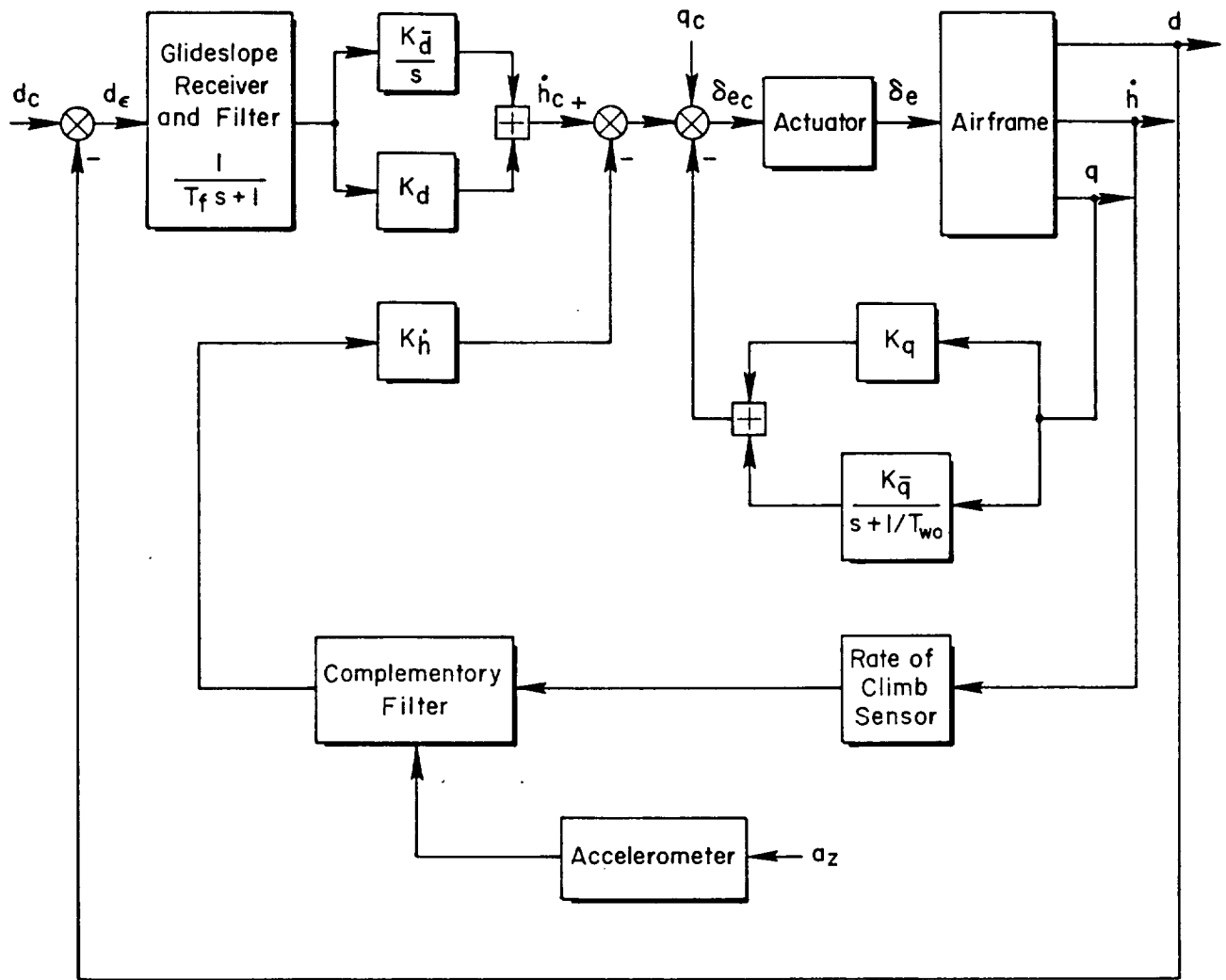
Figure D-1. Proposed Synthetic ILS Beam Follower

The regulation requirements are similar, i.e.,

1) To maintain the established flight path in the presence of disturbances such as gusts, winds, and wind shears

2) To provide a degree of short term attitude stability in the presence of disturbances.

The requirements stated above relate primarily to the low frequency response of the aircraft/autoland system, i.e., they pertain to the desired spatial trajectory during beam tracking. However, achieving these basic guidance requirements requires an acceptable design for the inner attitude loops. The synthesis of the Fig. D-1 structure from the above requirements is analyzed in detail in Ref. D-2 and will be reviewed briefly here for perspective in the selection of gains for the proposed system. The most fundamental guidance requirement is that the aircraft establish itself on the beam when the system is engaged. In other words, the deviation from the beam, d, must ultimately become zero when the system input is an initial condition $d_o \neq 0$. It is demonstrated in Ref. D-2 that this implies the need for a proportional, i.e., K_d term in the beam deviation feedback loop to establish static stability with respect to the beam.

It is also desirable that the system prevent beam deviation stand of errors, with minimal long term error. This consideration leads to a requirement for an integral term in the beam deviation feedback (or even higher order integration paths depending on the complexity of the deviation command). For example, a change in glideslope angle could be generated by input of a ramp beam deviation command, d_c. In the steady state, beam deviation error, d_ε, should go to zero: however, the measured sinkrate $\dot{H}$ will not be zero.* Thus, to achieve a zero pitch rate command in the steady state, a non-zero value of $\dot{h}_c$ is required which in turn requires the presence of a integrator in the beam

---

*Total sinkrate $\dot{H} = \dot{H}_o + \dot{h}$ is measured where $\dot{H}$ is the nominal (non-zero) sinkrate for ideal beam following and $\dot{h} = \dot{d}$ is a perturbation about the nominal.

deviation loop. However, since the beam following system will be phased out during flare in the proposed autoland system, the requirements for command following are less critical for this application.

As noted in Ref. D-2, regulation against steady U-gusts imply a need for a proportion beam deviation feedback and regulation against horizontal windshear implies a need for an integral term, i.e., $K_{\bar{d}}$. The requirements for regulation against W-gusts are more critical in that the integral term is required to regulate against steady gusts and that even with an integral term there will be a steady state error due to any shears component of a W-gust. W-gust regulation can be improved by selecting T_{wo} properly. Ideally this is done by setting $1/T_{wo}$ just below the short period frequency so that there is effective attitude (q/s) feedback at the short period mode, which is then washed out at lower frequencies. This allows the aircraft to weathercock at lower frequencies and thus unload W-gust induced angle of attack increments which would tend to cause the aircraft to deviate from the beam.

The above conclusions are derived from analyses in Ref. D-2 which is based on a 3 DOF analysis with unconstrained speed dynamics. While there will be some difference in the dynamical details for the speed constrained case, the same basic system elements will still be required. Furthermore, given the uncertainties regarding the auto throttle design, it is desirable to use a system which is independent of speed constraint as is the Fig. D-1 system. The inner sinkrate feedback loop approximates a $\dot{d}$ feedback and thus provides a damping term in the beam deviation (higher frequency) dynamics. The pitch feedback inner loops provide short period damping as well as short term attitude stability through the pseudo pitch attitude (pseudo integral of q) term. Finally, the inner pitch rate feedback provides a properly calibrated pitch rate command system for the outer path loops independent of uncertainties in the airframe pitch dynamics.

3. $q \rightarrow \delta_e$ Loop Design

The basic problem in design of the pitch rate feedback loop is the selection of the two time constants T_{wo} and T_E where

$$T_E = K_q/K_{\dot{q}} \qquad\qquad (D-1)$$

Furthermore, it is desired to select one set of gains which are adequate over the 80 to 110 kt speed range. Figure D-2 shows a comparison of the Bode asymptotes at 80 and 110 kts for the airframe $|q/\delta_e|$ under the speed constrained assumption and it may be seen that while there is almost a factor of two difference in dynamic pressure, the net effect on the response is not large.

The basic considerations in the selection of the time constant T_E (which indicates the relative mix of effective pitch attitude and pitch rate feedbacks) may be seen as sketched in Fig. D-3. An upper limit on the value of the inverse time constant

$$1/T_E \leqslant \omega_{ca} \qquad\qquad (D-2)$$

is set by a desire to have the open loop Bode magnitude asymptote be "K/s" in the region of crossover for good open loop phase margin and consequently good closed loop damping for the short period mode. A high value of $1/T_E$, approaching the crossover frequency, is desired, however, to maximize the low frequency gain margin, GM. This conflicts with a desire to place $1/T_E$ well below the crossover region to maximize the phase lead contribution at crossover. The desire for maximizing phase lead is generally not as critical as the need for good low frequency gain margin—unless the high frequency lags from the servo, etc. are very large. Thus, a near optimal selection for $1/T_E$ would be at or near the asymptotic crossover frequency, ω_{ca}. The value of $1/T_E = 3.7$ rad/sec that is used for the existing PA-30/BCS system is a reasonable choice for the 80 to 110 kt speed range. Examination of the Bode plots for the existing PA-30/BCS system shown in Figs. C-1a and C-1b of Appendix C indicate that while $1/T_E$ could be somewhat higher, this selection provides adequate low frequency gain margin and further allows some
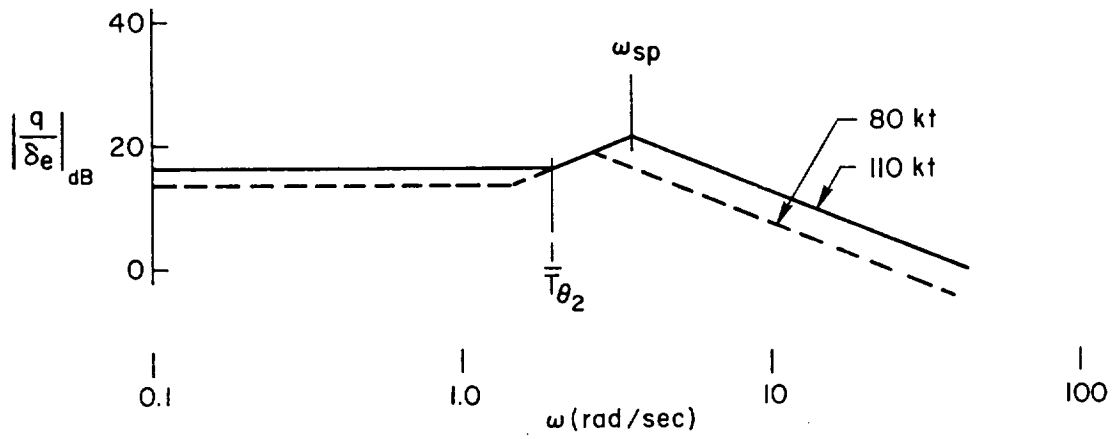
Figure D-2. Effect of Airspeed on Airframe $|q/\delta_e|$ Frequency Response
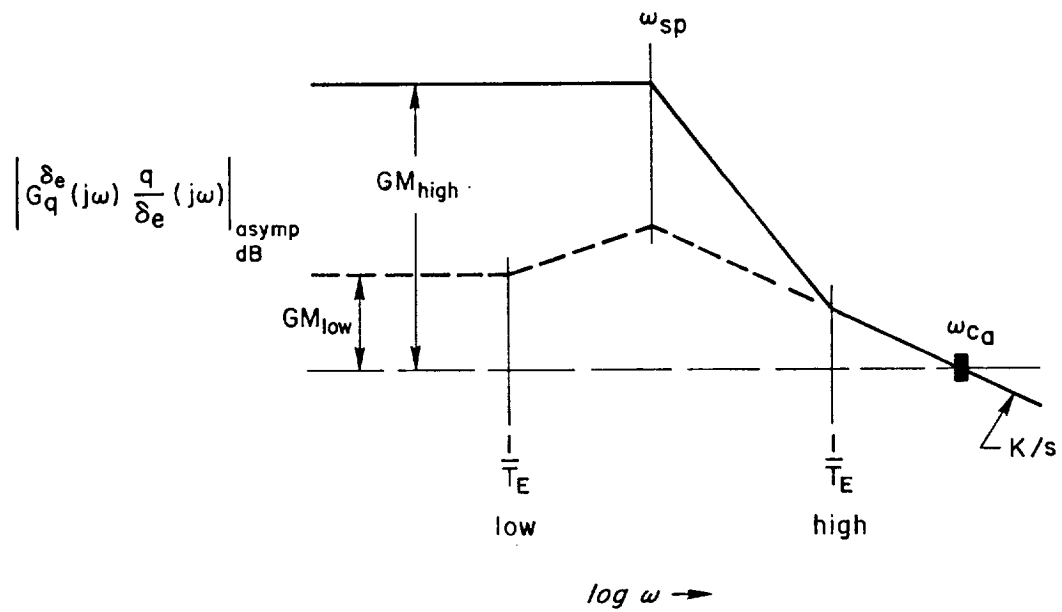
Figure D-3. Selection of $1/T_E$

reduction in the gain K_q if needed to account for increased phase lags from time delays, etc.

As noted previously in the discussion of guidance requirements for the beam following system, a primary consideration in the selection of the washout time constant is a desire to allow the aircraft to weathercock at frequencies below the short period to reduce beam deviation due to W-gusts (i.e., windproofing). This implies setting $1/T_{wo}$ near but below the short period frequency. A further consideration is the effect of the washout on low frequency gain margin. As indicated in Fig. D-4, if $1/T_{wo}$ washout lag is placed near the attitude numerator $1/T_{\theta_2}$, as shown in Fig. D-4b, there will be no additional loss of low frequency gain margin beyond that implied by the selection of $1/T_E$. However, as the washout is moved above $1/T_{\theta_2}$ towards the short period there is additional loss in low frequency gain margin (Fig. D-4c). By way of comparison the washout used for the existing BCS system is shown in Fig. D-4a. While this provides additional low frequency gain margin it would detract from the windproofing goal. Furthermore, the selection of the low value of the washout lag in the existing PA-30/BCS system is critical to the design of the sinkrate loop as shown previously in Fig. C-3. It will be shown shortly, this requirement is not necessary for the proposed system. Thus, consistent with the Ref. D-2 design philosophy, the washout inverse time constant is set as

$$\frac{1}{T_{wo}} = \frac{1}{T_{\theta_2}}\bigg|_{80 \text{ kts}} = 1.48 \text{ rad/sec} < \frac{1}{T_{\theta_2}}\bigg|_{110 \text{ kts}} \quad (D-3)$$

Having set the two time constants, it only remains to select the loop gain K_q. The primary consideration here is to use a high gain (i.e., high crossover frequency) to maximize the bandwidth of the inner loop as a pitch rate command system — since the inner loop bandwidth ultimately constrains the achievable outer loop bandwidth. The primary constraint on the pitch rate gain is destabilization of the servo mode
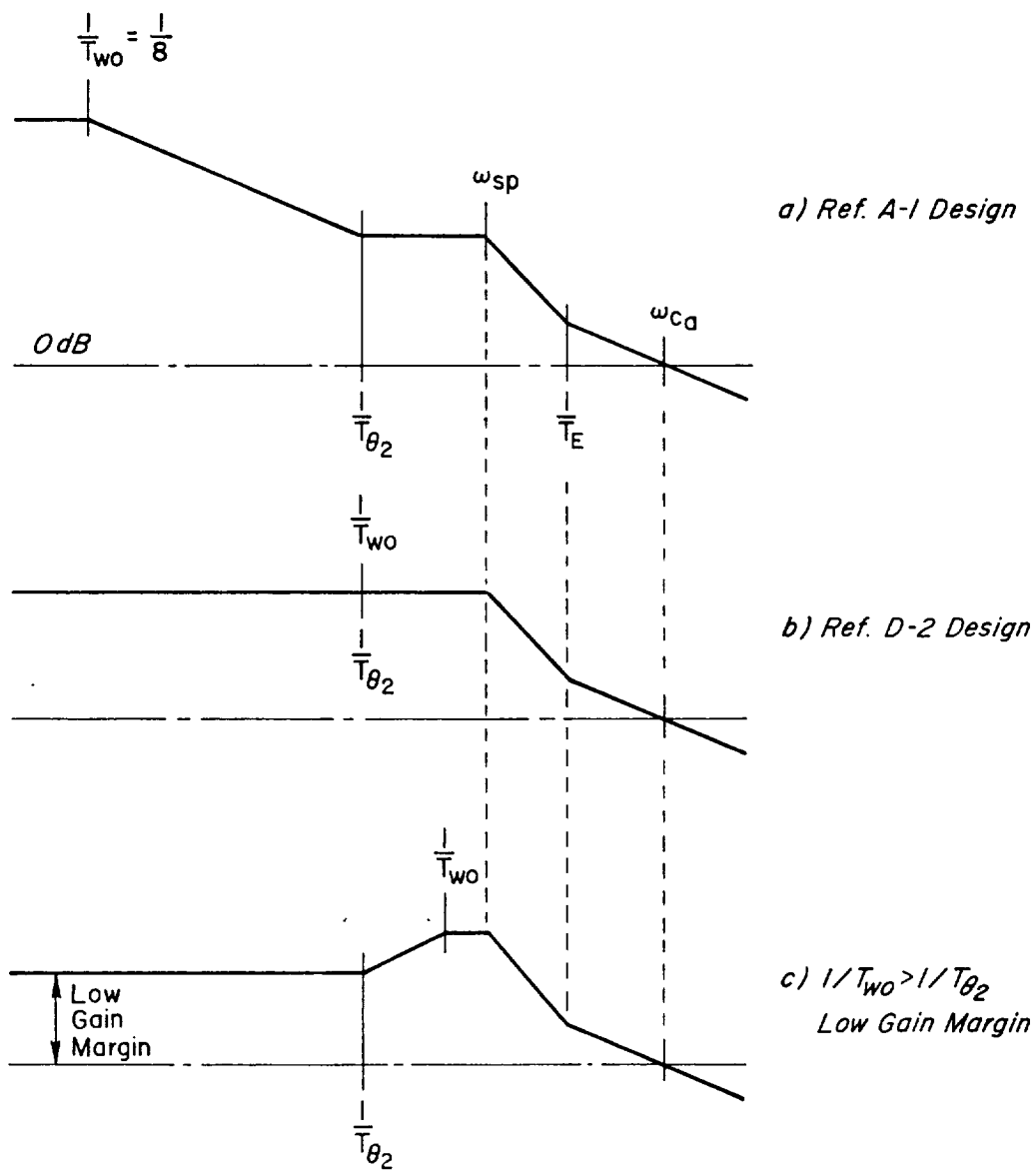
Figure D-4. Selection of Washout Time Constant

as noted previously in Appendix C. Since the phase margin in the cross-over region is relatively insensitive to the washout time constant, the situation is very similar to the existing pitch rate system. Thus, a K_q of 0.25 rad/sec corresponding to the best gain noted in Ref. D-3 will be used for the proposed system.

4. Closed Loop q/q_c Response

With the effective inner loop dynamics viewed as a pitch rate command system, the pitch rate response to pitch rate command is

$$\frac{q'}{q_c} = \frac{-\left(\dfrac{1}{T_A s + 1}\right) N^q_{\delta_e}}{\Delta - \dfrac{K_q(1/T_E)}{(1/T_{wo})}\left(\dfrac{1}{T_A s + 1}\right) N^q_{\delta_e}}$$

$$= \frac{-\dfrac{1/T_A}{(1/T_A)} N^q_{\delta_e}}{\dfrac{(1/T'_{wo})(1/T'_A)[\zeta', \omega'_n]}{(1/T_{wo})(1/T_A)}}$$

$$\doteq \frac{-M_{\delta_e}(1/T_{\theta_2})}{[\zeta', \omega'_n]} \cdot \frac{1/T_A}{(1/T'_A)}$$

$$= \begin{cases} \dfrac{40.1(1.98)}{[0.657, \ 14.1]} \cdot \dfrac{18}{(4.45)} & \text{110 kts} \\[30pt] \dfrac{21.8(1.48)}{[0.889, \ 8.99]} \cdot \dfrac{18}{(6.01)} & \text{80 kts} \qquad \text{(D-4)} \end{cases}$$

5. Relation of the Inner Attitude and Outer Path Loops

Using the speed constrained sinkrate-to-pitch rate response transfer function, Eq. C-13, Appendix C, the sinkrate-to-pitch rate command transfer function is

$$\frac{\dot{h}}{q} \doteq \frac{U_0 \gamma}{s \theta} \doteq \frac{U_0}{s(T_{\theta_2}s + 1)}$$

$$\frac{\dot{h}}{q_c} \doteq \frac{U_0}{s(T_{\theta_2}s + 1)} \cdot \frac{q}{q_c}(s)$$

$$= \frac{U_0/T_{\theta_2}}{s\left(s + 1/T_{\theta_2}\right)} \cdot \frac{-M_{\delta_e}\left(s + 1/T_{\theta_2}\right)}{[\zeta', \omega_n']} \cdot \frac{1/T_A}{\left(1/T_A'\right)}$$

Noting that $1/T_{\theta_2} \doteq -Z_w$

$$\frac{\dot{h}}{q_c} \doteq \frac{U_0 M_{\delta_e} Z_w / T_A}{s(1/T_A')[\zeta', \omega_n']} \tag{D-5}$$

From Eq. D-5 it may be seen that the sinkrate-to-pitch rate command response is 'K/s' out to the closed loop actuator break point

$$1/T_A' = \begin{cases} 4.45 \text{ rad/sec at } 110 \text{ kts} \\ \\ 6.01 \text{ rad/sec at } 80 \text{ kts} \end{cases} \tag{D-6}$$

which is above $1/T_{\theta_2} < 1.9$ rad/sec. Because of the strong actuator-short period coupling, the sinkrate loop bandwidth might even be improved by reducing K_q although this should not be necessary. When the succeeding beam deviation loops, d and $\int$d to elevator are closed, there will thus be a hierarchy of K/s closures.

6. Selection of Path Loop Gains

The control law implied by Fig. D-1 is

$$\delta_e = \left[\frac{K_{\bar{d}} + K_d s}{s(T_f s + 1)} d + K_{\dot{d}}\ddot{d} + G_q^{\delta_e} q \right] G_s(s)$$

$$= \left[\frac{K_{\dot{d}}(1/T_{d_1})(1/T_{d_2})(1/T_{d_3})}{s(1/T_f)} d + G_q^{\delta_e} q \right] G_s(s) \qquad (D-7)$$

As noted in Ref. D-2, the beam deviation inverse time constants are approximately related to the system gains as

$$\frac{1}{T_{d_1}} \doteq \frac{K_{\bar{d}}}{K_d} \quad , \quad \frac{1}{T_{d_2}} \doteq \frac{K_d}{K_{\dot{d}}} \quad , \quad \frac{1}{T_{d_3}} \doteq \frac{1}{T_f} \qquad (D-8)$$

Selection of the beam filter characteristics which define the time constant, T_f depend on the nature of the beam noise which is unknown for the synthetic ILS beam. However, it may be assumed that the time constant $1/T_{d_3}$ will cancel $1/T_F$. Thus, only the time constants $1/T_{d_1}$ and $1/T_{d_2}$ need be selected. As noted in Ref. D-2 these time constants are ordinarily related to the phugoid but under the assumption of speed constraint, we merely need to select the inverse time constants to be well below the beam deviation loop crossover frequency to achieve a wide K/s

region with near maximum phase lead from these terms. Therefore, following Ref. D-2 we select

$$\frac{1}{T_{d_2}} \doteq \frac{K_d}{\overset{\bullet}{K_d}} = 0.3 \text{ rad/sec}$$

$$(D-9)$$

$$\frac{1}{T_{d_1}} \doteq \frac{K_{\overline{d}}}{K_d} = 0.15 \text{ rad/sec}$$

The beam follower loop closures are summarized in the Bode root loci of Figs. D-5a and D-5b at 110 and 80 kts. For comparison, a generic sketch of the conventional root locus for the beam follower is shown in Fig. D-5a. It may be seen that for any speed in the 80 to 110 kt range, there is a broad K/s region between $1/T_{d_2}$ and the actuator time constant $1/T_A'$ with sufficient phase margin to close the beam follower loop at crossover frequencies approaching 2 rad/sec. On this basis, a loop gain, $\overset{\bullet}{K_d} = -42$ dB or 0.0080 rad/ft/sec, should provide good beam following performance. It should be noted that there is a conditional low frequency instability in this system which implies a lower limit on the gain $\overset{\bullet}{K_d}$ as well as an upper limit. These two limits correspond roughly with the extent of the K/s region and do <u>not</u> compromise the design. The low frequency conditional instability, which would occur only if the gain $\overset{\bullet}{K_d}$ were too low, is a consequence of the speed constraint and does not occur for the unconstrained 3 DOF analysis in Ref. D-3.

7. Variable τ Flare System Design

A generic mechanization of the variable τ flare law is shown in Fig. D-6. There are several possible ways to obtain a measure of ground speed V_G in wind which will affect details of the actual mechanization, but will not affect selection of the basic gains shown in Fig. D-6. Figure D-6 produces a variable τ flare law consistent with Eq. 24 which (in a rearranged form) is

a) Bode Root Locus, 110 kts

$$G(s) = \frac{+2.65 \cdot 10^5 K_d^1(.15)(.30)(1.48)}{s^3(1.87)(4.45)[.657, 14.1]}$$ $K_d = 1.0$
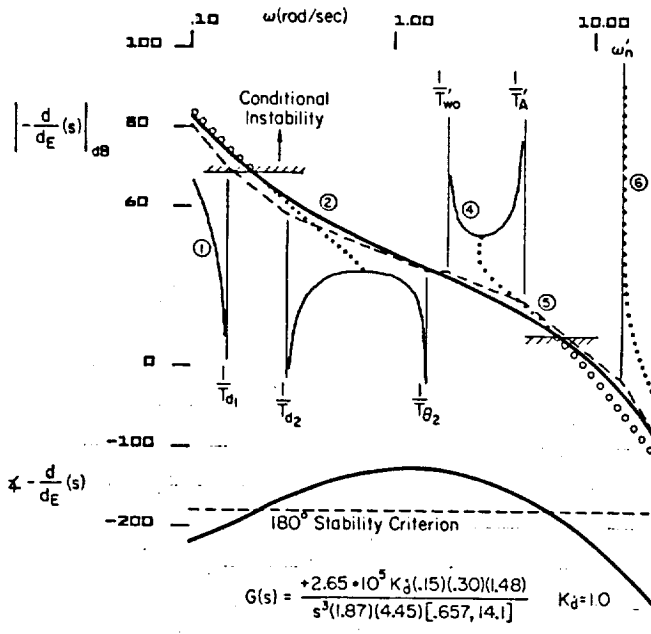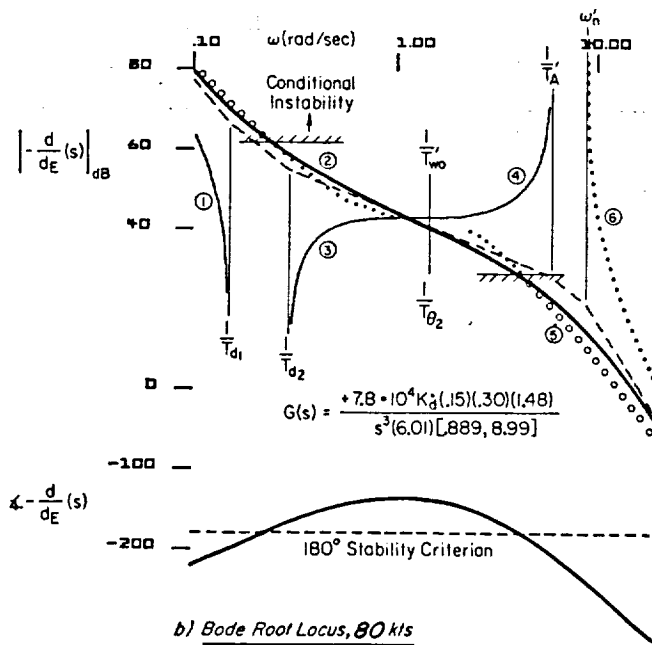
Legend:
∎ Closed loop root
— $|G(j\omega)|$ and $\measuredangle G(j\omega)$ open loop
- - - $|G(j\omega)|$ and $\measuredangle G(j\omega)$ open loop, asymptote
— $|G(-\sigma)|$ left half plane (stable) root locus
• • • • Complex plane root locus

b) Bode Root Locus, 80 kts

$$G(s) = \frac{+7.8 \cdot 10^4 K_d^1(.15)(.30)(1.48)}{s^3(6.01)[.889, 8.99]}$$
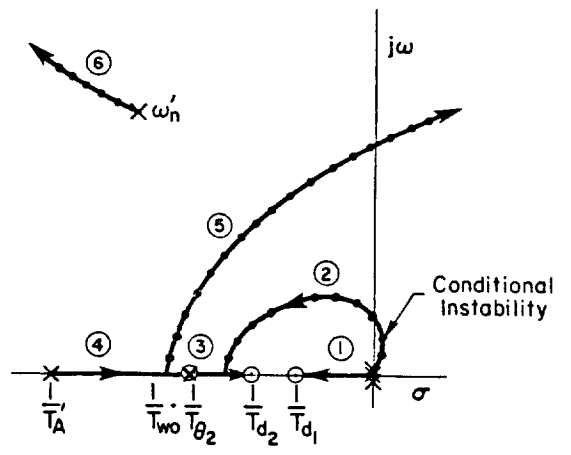
c) Generic Sketch Of Conventional Root Locus

Figure D-5. System Survey of the d→q_c Loop, Speed Constrained
(1/T_{wo} = 1.48 rad/sec, 1/T_E = 3.7 rad/sec)
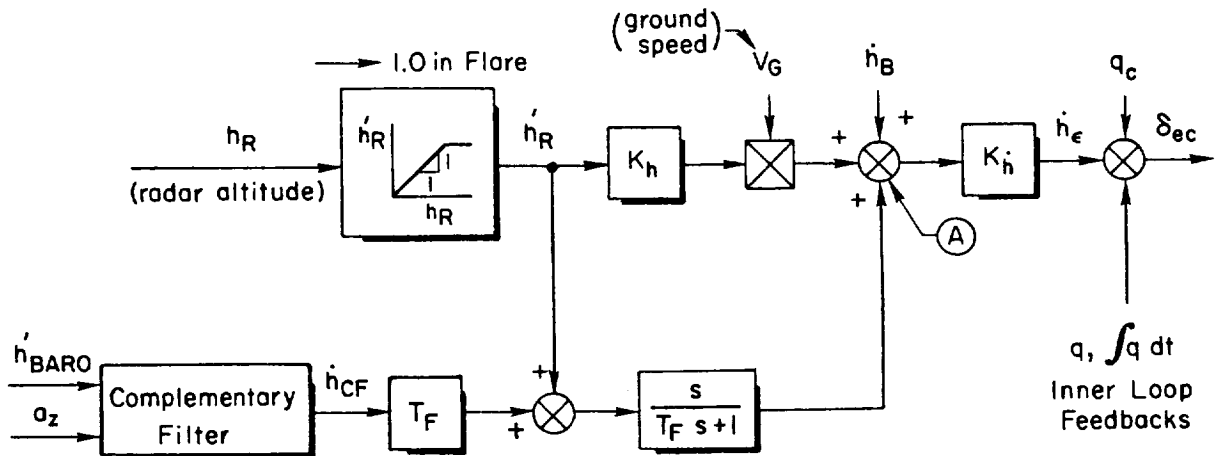
Figure D-6. Generic Variable τ System Mechanization

$$\frac{dh}{dt} + \frac{V_G}{\tau_0 V_{G_0}} (h + h_B) = 0 \qquad (D-10)$$

The above ordinary differential equation is the ideal ($\dot{h}_\epsilon = 0$) for summer A in Fig. D-6. That is, the signal through the upper forward path is proportional to altitude, h, where

$$K_h = \frac{1}{\tau_0 V_{G_0}}$$

$$\dot{h}_B = \frac{V_G}{\tau_0 V_{G_0}} h_B \qquad (D-11)$$

and the lower forward path is proportional to sinkrate dh/dt. The mechanization shown in Fig. D-6 causes the baro-inertial sinkrate, $\dot{h}_{CF}$ used in beam following to be washed out in flare with time constant T_F and replaced by the derivative of the radar altimeter signal, i.e., washed out h_R which is "runway referenced." This system can thus be considered to be runway referenced within 3 T_F seconds after flare initiation.

Thus, the primary consideration in the selection of the washout time constant, T_F is that it be much shorter than the flare law time constant τ.

The control law derived from Fig. D-6 is

$$\dot{h}_\varepsilon = K_{\dot{h}} \left[K_h V_G h_R + \left(\frac{s}{T_F s + 1} \right) h_R + \left(\frac{s T_F}{T_F s + 1} \right) \dot{h}_{CF} + \dot{h}_B \right] \qquad (D-12)$$

If it is assumed for basic analysis that the radar altimeter and baro-inertial rate of climb sensor characteristics are ideal (unity gains) then

$$\dot{h}_\varepsilon = K_{\dot{h}} \left[K_h V_G + \frac{s}{T_F s + 1} + \frac{s^2 T_F}{T_F s + 1} \right] h + K_{\dot{h}} \dot{h}_B$$

$$= K_{\dot{h}} \left[\frac{s^2 + (K_h V_G + 1/T_F)s + K_h V_G / T_F}{(s + 1/T_F)} \right] h + K_{\dot{h}} \dot{h}_B \qquad (D-13)$$

Since $K_h V_G = 1/\tau$

$$\dot{h}_\varepsilon = \left[\frac{K_{\dot{h}}(s + 1/\tau)(s + 1/T_F)}{(s + 1/T_F)} \right] h + K_{\dot{h}} \dot{h}_B$$

$$= K_{\dot{h}}(s + 1/\tau)h + K_{\dot{h}} \dot{h}_B \qquad (D-14)$$

Thus, from Eq. D-14 it may be seen that the Fig. D-6 mechanization produces the variable τ control law as required.

The same inner loop pitch rate command system used for the beam follower may be used for the flare law and thus, the open loop sinkrate-to-sinkrate error transfer function is (from Eq. D-5)

$$\frac{\dot{h}}{q_c} = \frac{K}{s(1/T_A')[\zeta',\omega_n']} \qquad \text{(D-15)}$$

where $K = U_o M_{\delta_e} Z_w / T_A$

Equation D-14 implies a feedback transfer function

$$G_{\dot{h}}^{\delta e} = -K_{\dot{h}}(s + 1/\tau) \qquad \text{(D-16)}$$

The open loop transfer function for the flare law is thus

$$\frac{\dot{h}_\epsilon}{q_c}\bigg|_{OL} = G_{\dot{h}}^{\delta e}\frac{1}{s}\frac{\dot{h}}{q_c} = \frac{K_{\dot{h}}K(s + 1/\tau)}{s^2(1/T_A')[\zeta',\omega_n']} \qquad \text{(D-17)}$$

which is shown in the bode root locus plot of Fig. D-7 for an 80 kt flare with the nominal (zero wind) $\tau = 19.8$ sec corresponding to the existing PA-30/BCS law. It may be seen from Fig. D-7 that there is a broad K/s region with potential for a 2 to 3 rad/sec crossover for the flare law. Unlike the beam follower no conditional instability occurs in this case because there is no integral feedback term. It may be seen that the flare inverse time constant is much lower than the desired crossover frequency and thus the crossover region is quite insensitive to $1/\tau$ over the ±30 kt steady wind range where

$$0.032 < \frac{1}{\tau} < 0.069 \qquad \text{(D-18)}$$
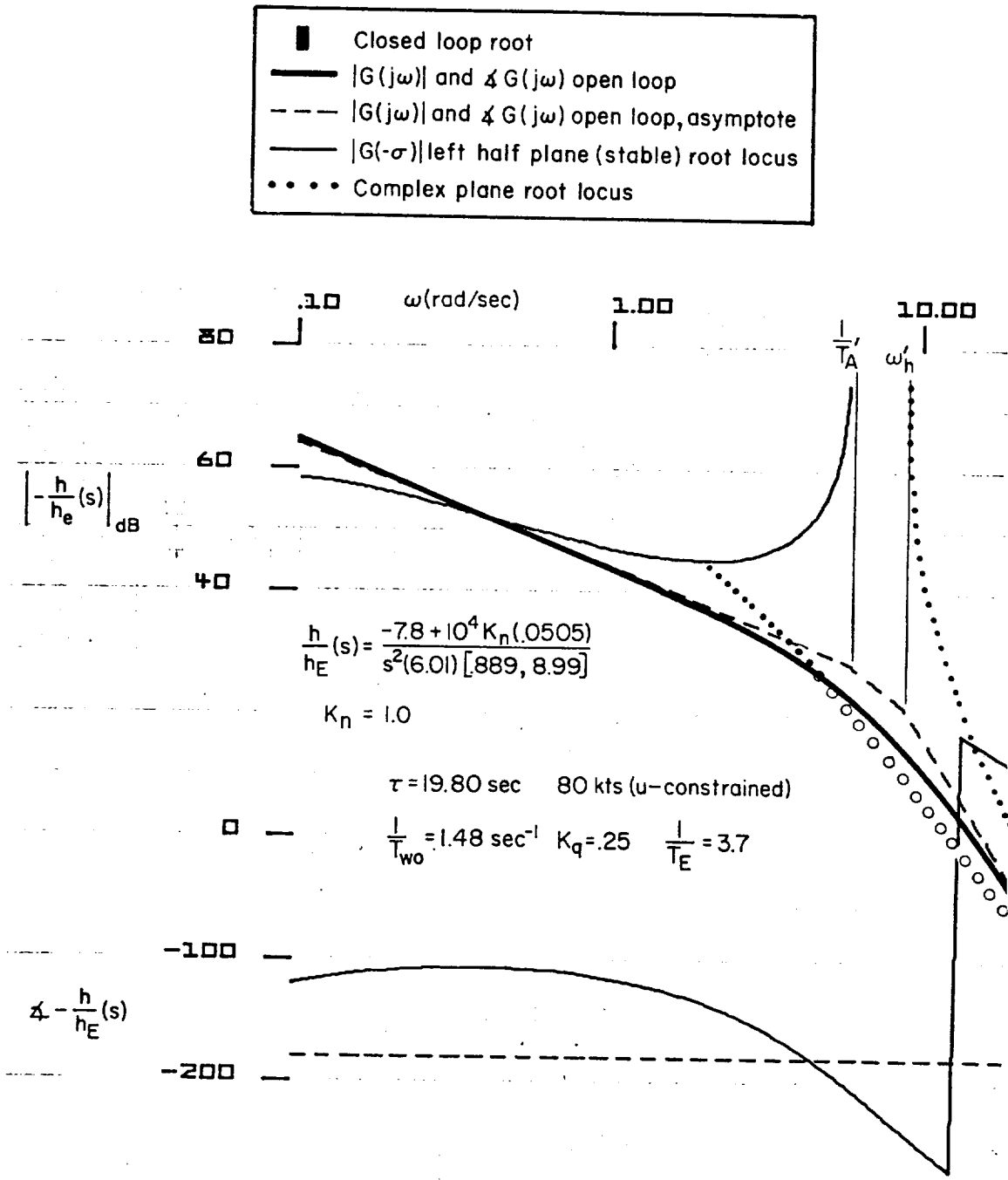
Figure D-7. Closure of Flare Low Loop in Figure D-6

Thus, the variation of τ over the nominal windspeed range should not effect the flare law loop closure. A selection of $K_{\dot{h}} = -38$ dB $= 0.0126$ rad/ft/sec will give an asymptotic crossover frequency of about 2 rad/sec.

REFERENCES

D-1. McRuer, Duane, Irving Ashkenas, and Dunstan Graham, <u>Aircraft Dynamics and Automatic Control</u>, Princeton University Press, 1973.

D-2. McRuer, Duane T., Walter A. Johnson, <u>Development of Approach Control System Requirements with Applications to a Jet Transport</u>, NASA CR-2023, May 1972.

D-3. Internal memo from John W. Edwards to HIMAT Project Office, Summary of Flight Tests and Analysis of the HIMAT BCS Approach and Landing System Using the PA-30 Airplane, Dryden Flight Research Center, NASA, 22 Nov. 1978.
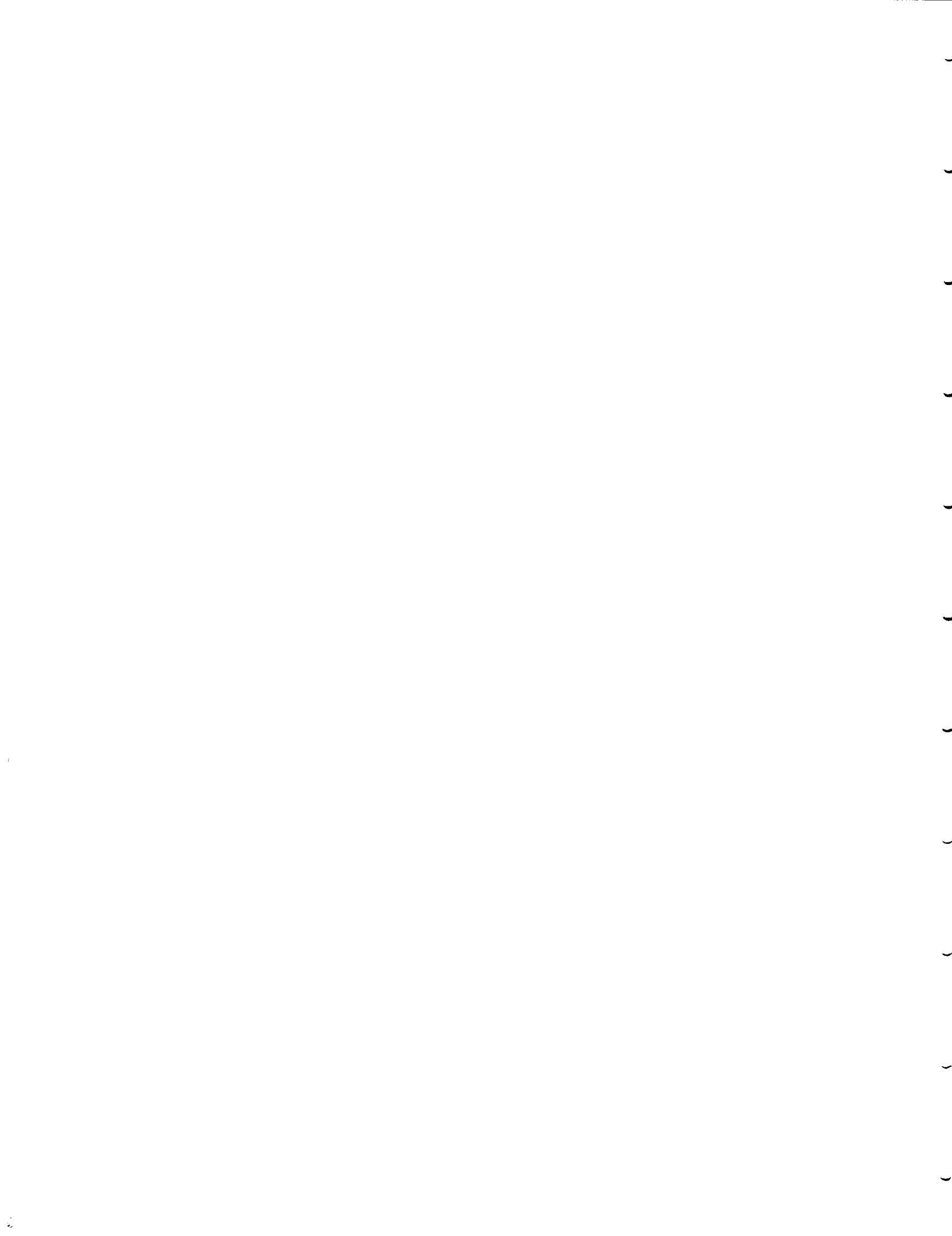
APPENDIX E

CIRCULAR ORBIT ALGORITHM

A. TIME HISTORIES

Figures E-1 to E-5 present time histories for several values of air-speed and wind speed (dimensions in ft, sec, rad). Variables are X1 = x, X2 = y, X3 = ψ.
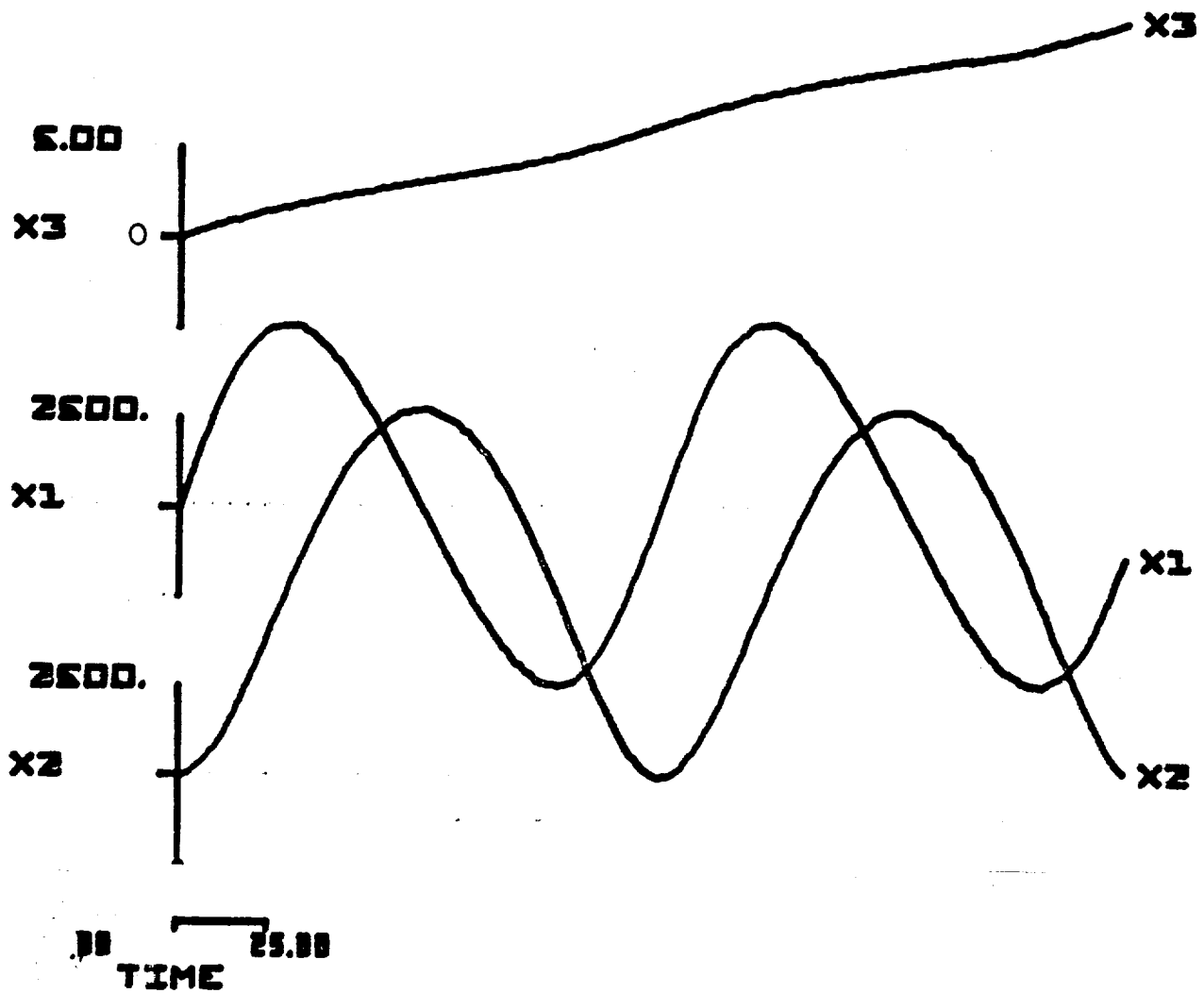
Figure E-1. Circular Algorithm, U = 500, V_w = 100
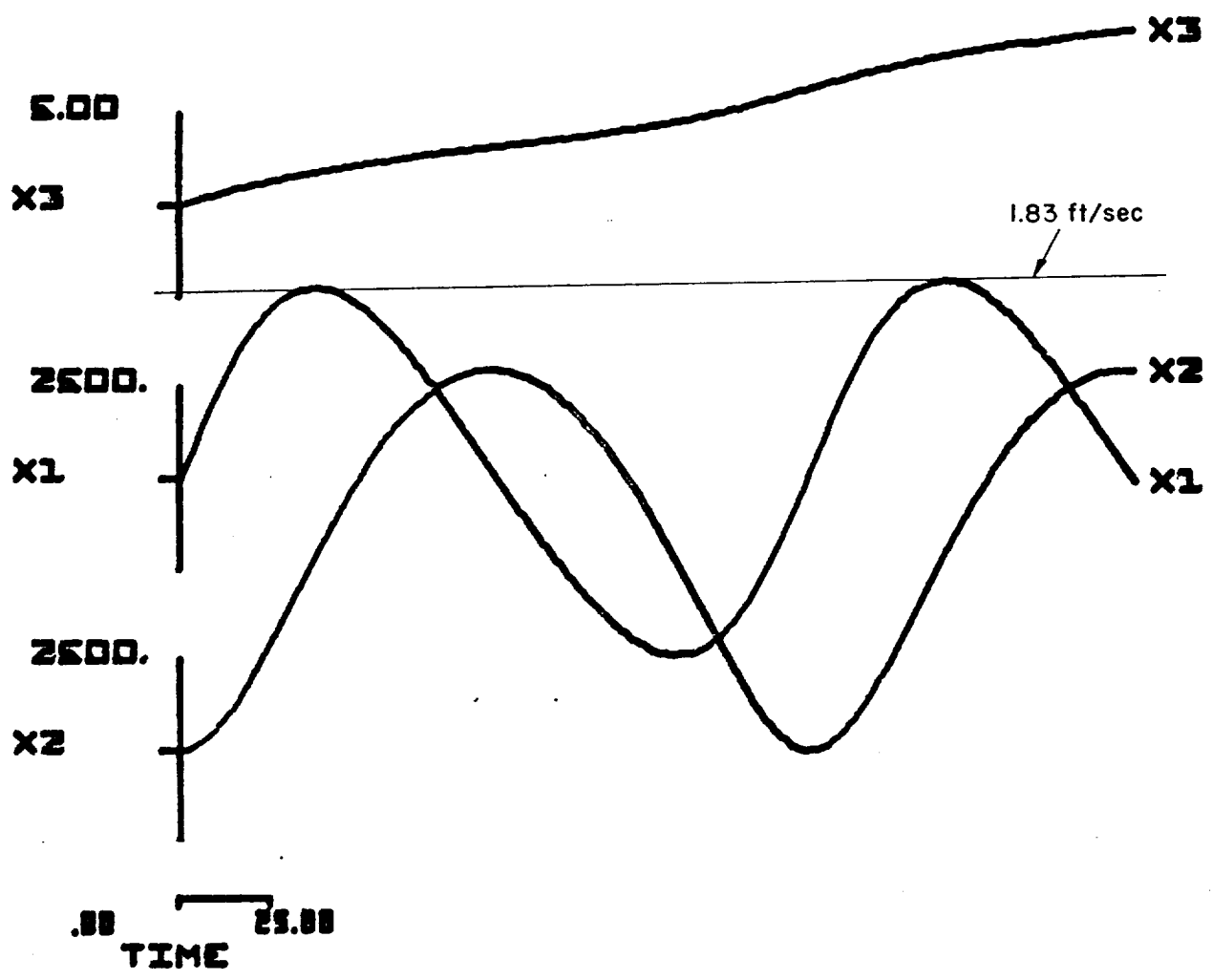
Figure E-2. Circular Algorithm, U = 400, V_w = 100
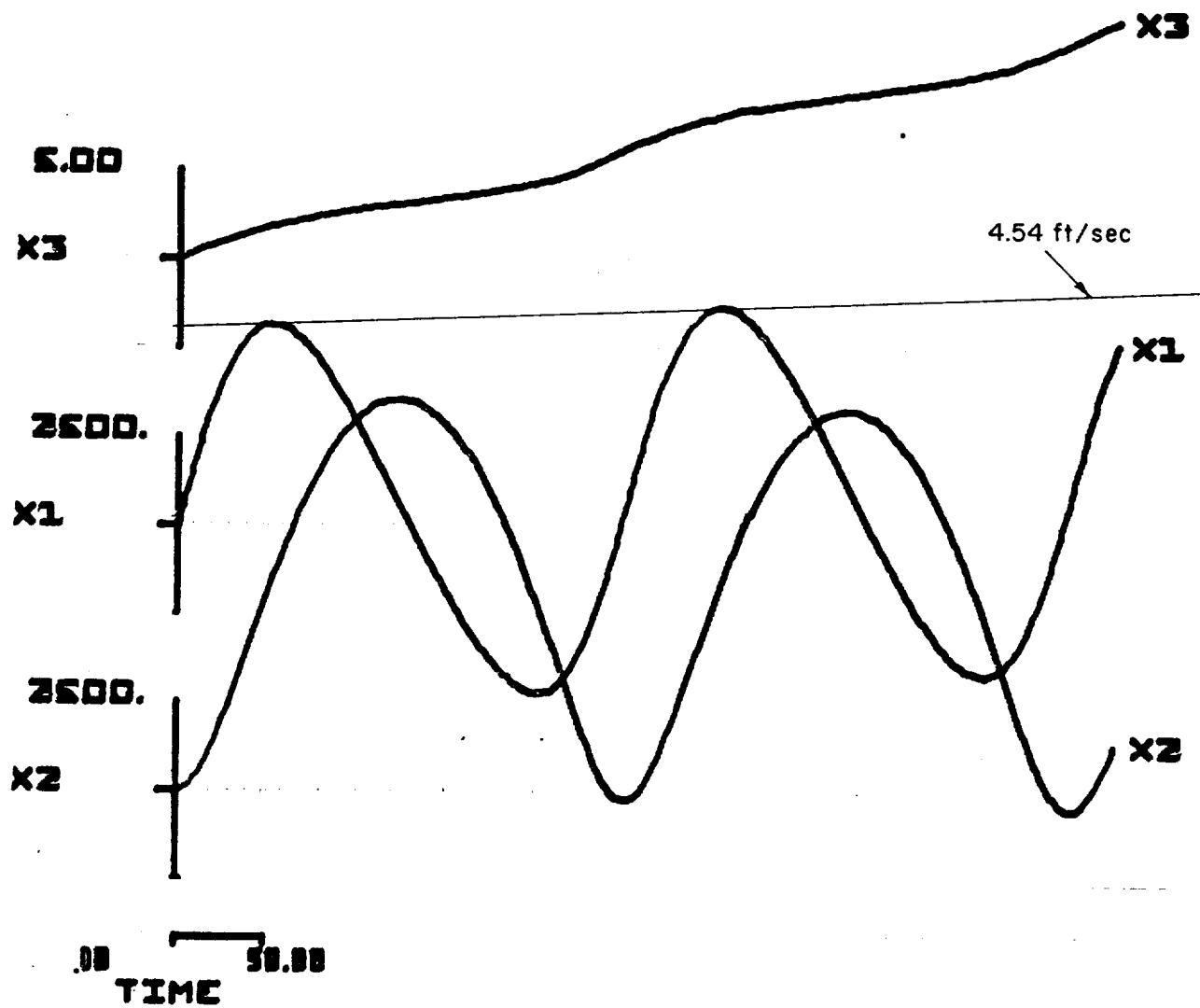
Figure E-3. Circular Algorithm, U = 300, V_w = 100
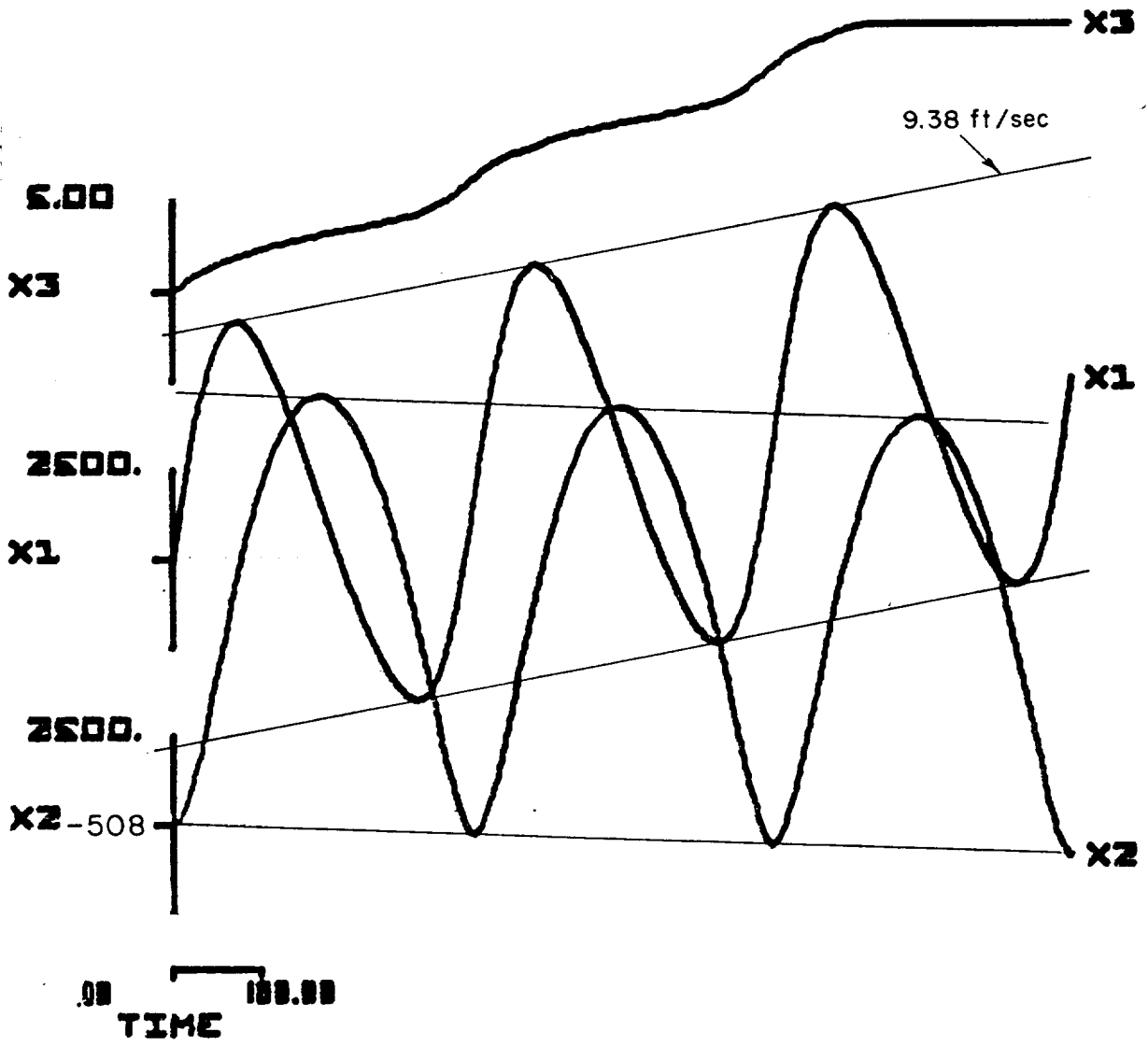
Figure E-4. Circular Algorithm, U = 250, V_w = 100
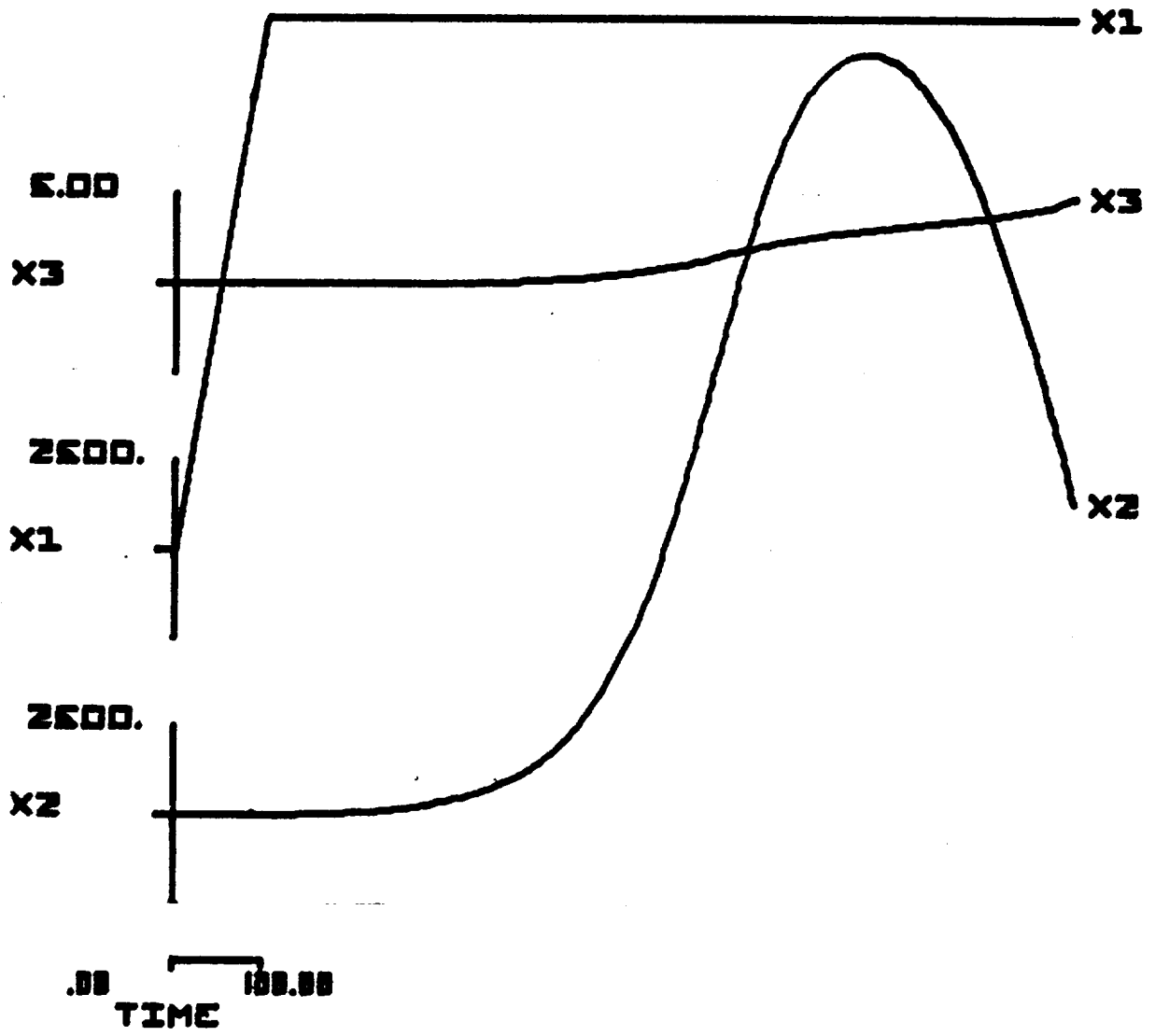
Figure E-5.   Circular Algorithm, U = 200, V_w = 100

APPENDIX F

DEAD RECKONED WING POINTING ALGORITHM

A. TIME HISTORIES

Figures F-1 to F-3 present time histories for several values of air-speed and wind speed (dimensions in ft, sec, rad). Variables are $X1 = x$, $X2 = y$, $X3 = \psi$.
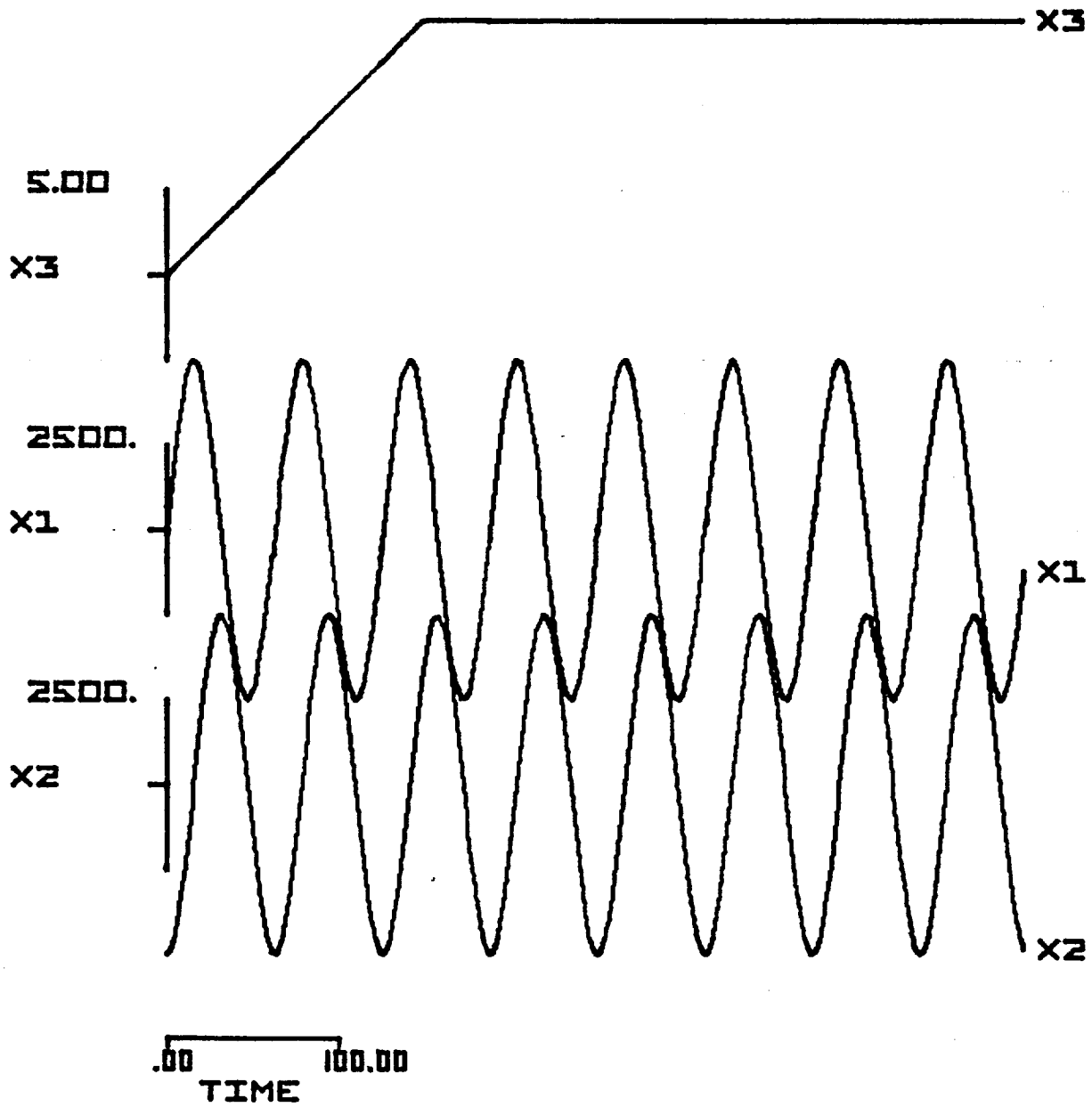
Figure F-1. Wing Pointing Algorithm, U = 500, V_w = 0
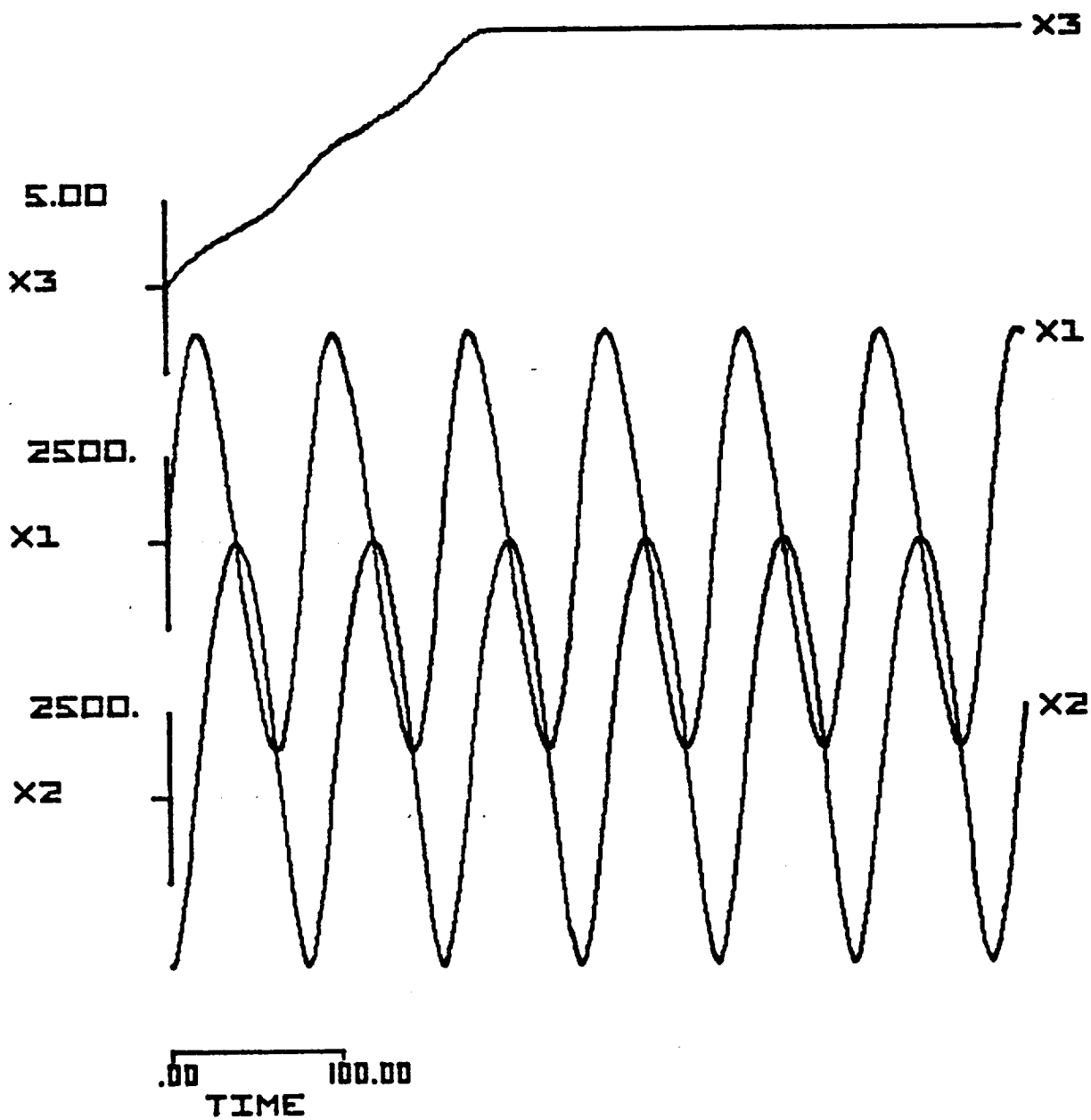
Figure F-2. Wing Pointing Algorithm, U = 500, V_w = 100
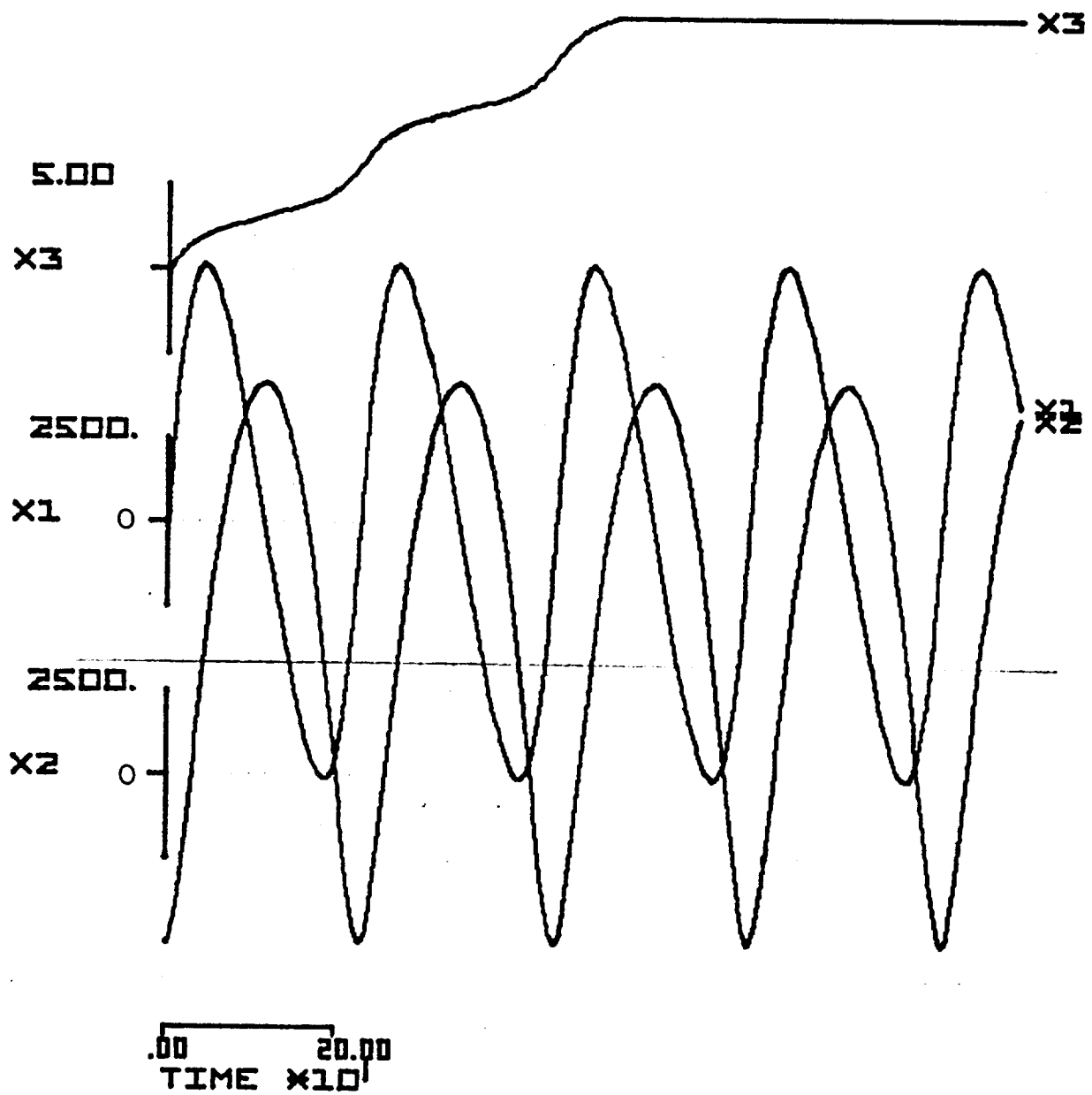
Figure F-3. Wing Pointing Algorithm, U = 250, V_w = 100